

# Investigation of Warm Convective Cloud Fields with Meteosat Observations and High Resolution Models

Von der Fakultät für Physik und Geowissenschaften  
der Universität Leipzig

genehmigte

## DISSERTATION

zur Erlangung des akademischen Grades  
Doktor der Naturwissenschaften  
(Dr. rer. nat.)

vorgelegt

von M. Sc. Sebastian Bley  
geboren am 25.06.1986 in Dresden

1. Gutachter: Prof. Andreas Macke  
2. Gutachter: Prof. Jerome Riedi

Tag der Verleihung: 23.10.2017

The present study was prepared between December 2012 and March 2017

at the Leibniz Institute for Tropospheric Research (TROPOS)

Remote Sensing Department

Permoserstraße 15

04318 Leipzig

Germany

The work was supervised by

Prof. Dr. Andreas Macke

# **Bibliografische Beschreibung**

Sebastian Bley

## **Untersuchung von warmen konvektiven Wolkenfeldern mittels Meteosat Beobachtungen und hochaufgelösten Modellen**

Universität Leipzig, Fakultät für Physik und Geowissenschaften

87 Seiten, 95 Literaturzitate, 8 Abbildungen (exklusive des kumulativen Teils)

### **Zusammenfassung:**

Die hohe raumzeitliche Variabilität von konvektiven Wolken hat erhebliche Auswirkungen auf die Quantifizierung des Wolkenstrahlungseffektes. Da konvektive Wolken in atmosphärischen Modellen üblicherweise parametrisiert werden müssen, sind Beobachtungsdaten notwendig, um deren Variabilität sowie Modellunsicherheiten zu quantifizieren. Das Ziel der vorliegenden Dissertation ist die Charakterisierung der raumzeitlichen Variabilität von warmen konvektiven Wolkenfeldern mithilfe von Meteosat Beobachtungen sowie deren Anwendbarkeit für die Modellevaluierung. Verschiedene Metriken wurden untersucht, um Unsicherheiten in Modell- und Satellitendaten sowie ihre Limitierungen zu quantifizieren. Mithilfe des hochaufgelösten sichtbaren (HRV) Kanals von Meteosat wurde eine Wolkenmaske entwickelt, welche mit  $1 \times 2 \text{ km}^2$  die Auflösung der operationellen Wolkenmaske von  $3 \times 6 \text{ km}^2$  deutlich übertrifft. Diese ermöglicht eine verbesserte Charakterisierung von kleinskaligen Wolken und bietet eine wichtige Grundlage für die Weiterentwicklung von satellitengestützten Wolkenalgorithmen. Für die Untersuchung der Lebenszyklen konvektiver Wolkenfelder wurde ein Tracking-Algorithmus entwickelt. Die raumzeitliche Entwicklung des Flüssigwasserpfads (LWP) wurde sowohl in einer Eulerschen Betrachtungsweise als auch entlang Lagrange'scher Trajektorien analysiert. Für die Wolkenfelder ergab sich eine charakteristische Längenskala von 7 km. Als Maß für die Wolkenlebenszeit ergab sich eine Lagrange'sche Dekorrelationszeit von 31 min. Unter Berücksichtigung des HRV Kanals verringern sich die Dekorrelationsskalen signifikant, was auf eine Sensitivität gegenüber der räumlichen Auflösung hindeutet. Für eine Quantifizierung dieser Sensitivität wurden Simulationen des ICON-LEM Modells mit einer Auflösung von bis zu 156 m berücksichtigt. Verbunden mit einem zwei- bis vierfach geringeren konvektiven Bedeckungsgrad besitzen die simulierten Wolken bei dieser hohen Auflösung deutlich größere LWP Werte. Diese Unterschiede verschwinden im Wesentlichen, wenn die simulierten Wolkenfelder auf die optische Auflösung von Meteosat gemittelt werden. Die Verteilungen der Wolkengrößen zeigen einen deutlichen Abfall für Größen unterhalb der 8- bis 10-fachen Modellauflösung, was der effektive Auflösung des Modells entspricht. Dies impliziert, dass eine noch höhere Auflösung wünschenswert wäre, damit mit ICON-LEM Wolkenprozesse unterhalb der 1 km-Skala realistisch simuliert werden können. Diese Skala wird zukünftig erfreulicherweise vom Meteosat der dritten Generation abgedeckt. Dies wird ein entscheidender Schritt für ein verbessertes Verständnis von kleinskaligen Wolkeneffekten sowie für die Parametrisierung von Konvektion in NWP und Klimamodellen sein.

# Bibliographic Description

Sebastian Bley

## Investigation of warm convective cloud fields with Meteosat observations and high resolution models

University of Leipzig, Faculty of Physics and Earth Sciences

87 Pages, 95 References, 8 Figures (excluding the cumulative part)

### Abstract:

Convective clouds have a high spatiotemporal variability that complicates the quantification of the cloud radiative effect. Since atmospheric models usually have to parameterize convective clouds, observations are needed to characterize their variability and to quantify model uncertainties. The aim of the present thesis is to characterize the spatiotemporal evolution of warm convective cloud fields using Meteosat observations and to evaluate simulated cloud fields in a high resolution atmospheric model. Several metrics are studied to quantify model and satellite retrieval uncertainties and sensor limitations. Meteosat's high resolution visible (HRV) channel was used to develop a cloud mask with  $1 \times 2 \text{ km}^2$  resolution that is much higher in comparison to the operational mask with  $3 \times 6 \text{ km}^2$  resolution. This HRV cloud mask improves the characterization of small-scale convective clouds and provides valuable information for the further development of cloud retrievals. For investigation of the spatiotemporal evolution, the cloud fields were tracked in sequential satellite images. The spatiotemporal change of the liquid water path (LWP) was analyzed adopting both, an Eulerian and a Lagrangian perspective. A characteristic length scale of 7 km was found for the cloud fields. Furthermore, a Lagrangian decorrelation time of 31 min is found corresponding to a measure of the average cloud life time. By taking into account the reflectance of the HRV channel, these decorrelation scales were essentially decreasing most likely due to small-scale cloud variability. This behavior indicates a high sensitivity of the decorrelation scales on the spatial resolution. To quantify this sensitivity, simulations from the ICON-LEM model with up to 156 m horizontal grid resolution were considered. At 156 m resolution, the simulations show a higher frequency of larger LWP values and an underestimation of the convective cloud fraction by a factor of two to four. These differences are essentially removed, if the simulated cloud fields are coarse-grained to the optical resolution of Meteosat. The distribution of the simulated horizontal cloud sizes shows a significant drop for sizes below 8–10 times the model grid resolution, which indicates the effective resolution of the model. This implies that simulations with an even higher spatial resolution than 156 m are desirable to resolve cloud scales below 1 km with ICON-LEM. Fortunately, this 1-km scale will be covered by Meteosat Third Generation. Such an observational capacity with a spatial resolution of at least 1 km will substantially improve the understanding of small-scale cloud effects as well as the parameterization development of cumulus convection for NWP and climate models.



# Contents

<b>1</b>	<b>Introduction</b>	<b>1</b>
1.1	The role of clouds in the climate system . . . . .	1
1.2	Climate change . . . . .	2
1.3	Satellite remote sensing of clouds . . . . .	4
1.4	Representation of convective clouds in atmospheric models . . . . .	5
1.5	Objectives . . . . .	6
<b>2</b>	<b>Instruments and related datasets</b>	<b>11</b>
2.1	The Meteosat SEVIRI instrument . . . . .	11
2.2	KNMI Cloud Physical Properties retrieval . . . . .	13
2.3	NWC SAF cloud products . . . . .	15
2.4	Uncertainties in cloud properties retrieved from geostationary satellites	16
<b>3</b>	<b>Model data</b>	<b>19</b>
3.1	ICON-LEM high resolution simulation . . . . .	19
3.2	COSMO-DE . . . . .	21
<b>4</b>	<b>Results and discussion</b>	<b>23</b>
4.1	First publication: A threshold-based cloud mask for the high-resolution visible channel of Meteosat Second Generation SEVIRI . . . . .	23
4.2	Second publication: Meteosat-based characterization of the spatiotemporal evolution of warm convective cloud fields over Central Europe . . . . .	35
4.3	Third publication: Metrics for the evaluation of warm convective cloud fields in a large eddy simulation with Meteosat images . . . . .	51
<b>5</b>	<b>Summary and Conclusions</b>	<b>63</b>
<b>6</b>	<b>Outlook</b>	<b>69</b>
	<b>Appendix</b>	<b>73</b>
A.1	Authors contribution to the three publications . . . . .	73

<b>Literature</b>	<b>74</b>
<b>List of Abbreviations</b>	<b>85</b>
<b>List of Symbols</b>	<b>87</b>
<b>List of Figures</b>	<b>87</b>
<b>List of Tables</b>	<b>88</b>
<b>Acknowledgements</b>	<b>89</b>
<b>Curriculum Vitae</b>	<b>91</b>

# 1 Introduction

## 1.1 The role of clouds in the climate system

Clouds play a fundamental role in the Earth's climate system. They cover around 70 % of Earth's surface (Stubenrauch et al., 2013), and influence the global climate and the hydrologic cycle through many complex interactions. The major energy source for the Earth is the sun. The incoming solar radiation, entering at the top of the atmosphere (TOA), is scattered and absorbed by cloud droplets and ice particles, aerosols, atmospheric gases and the Earth's surface. The annual global incoming solar energy on TOA is measured as  $340 \text{ W m}^{-2}$  on average (Fig. 1.1). From this amount of solar energy,  $100 \text{ W m}^{-2}$  are reflected back to space. The remaining portion of about  $240 \text{ W m}^{-2}$  is absorbed by the Earth's surface as well as gases and aerosol particles in the atmosphere, which is nearly balanced by the TOA thermal emission of  $239 \text{ W m}^{-2}$  (Wild et al., 2012). Considering the absorbed and emitted energy, an imbalance of approximately  $0.6 \text{ W m}^{-2}$  is estimated, which represents the increasing heat storage in the Earth-Ocean-Atmosphere system due to a warming climate system (Loeb et al., 2012). This net radiative imbalance has increased during the last decades (Allan et al., 2014).

Fig. 1.1 includes the uncertainty range for all fluxes, showing some fluxes with large uncertainties, as pointed out in many studies in the past (e.g., Hartmann et al., 1986; Kiehl and Trenberth, 1997; Gupta et al., 1999; Trenberth et al., 2009; Stephens et al., 2012; Wild et al., 2012). Estimation of the TOA fluxes has been improved in the last decades through advanced satellite missions like the Clouds and the Earth's Radiant Energy System (CERES, Wielicki et al., 1996). Despite these improved observations, substantial discrepancies remain between satellite observations and general circulation models (GCMs) for the global energy balance, mainly due to deficits in the process understanding which is important to develop appropriate parameterizations (Wild et al., 2012).

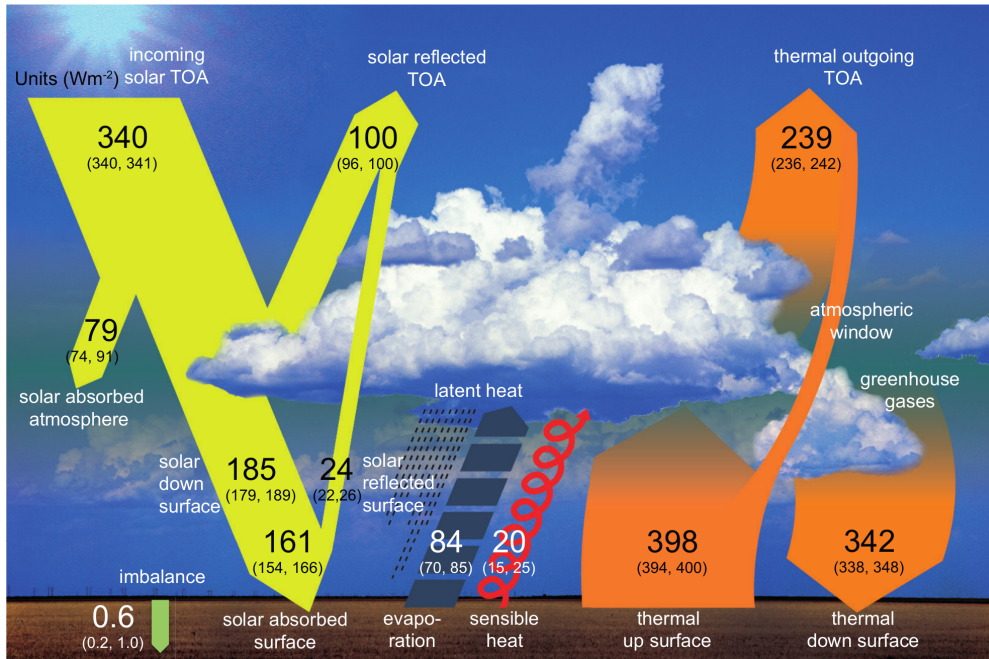


Figure 1.1: Annual global mean energy balance of the Earth, representing present day climate conditions at the the beginning on the twenty-first century (Wild et al., 2012).

## 1.2 Climate change

The major reason for the increase of the global average surface temperature of about 0.2 K per decade (Hansen et al., 2010) is the increase of greenhouse gases emitted by human activity. This warming is referred as the anthropogenic climate change. The primary greenhouse gases in Earth's atmosphere are water vapor (WV), carbon dioxide (CO<sub>2</sub>), nitrous oxide (N<sub>2</sub>O), methane (CH<sub>4</sub>) and tropospheric ozone (O<sub>3</sub>). The CO<sub>2</sub> concentration has substantially increased since 1750 due to human activity and exceeded the pre-industrial concentration by 40% (Hartmann et al., 2013). In 2013, CO<sub>2</sub> concentration surpassed 400 ppm for the first time in recorded history<sup>1</sup>. It is still not fully understood, how much the globe will warm exactly and how the climate system will respond to rising CO<sub>2</sub> concentration. Scientists are attempting to quantify the total amount of global warming by using measures like the transient climate response (TCR) and the equilibrium climate sensitivity (ECS).

While the TCR describes how much the Earth surface temperature will immediately warm, once the level of double CO<sub>2</sub> concentration is reached, the ECS refers to the change of the global mean surface temperature that would result after the Earth system has reached a new equilibrium for sustained doubling of the atmospheric CO<sub>2</sub>

<sup>1</sup>[http://climate.nasa.gov/climate\\_resources/24/](http://climate.nasa.gov/climate_resources/24/) (last accessed 29 August 2016)

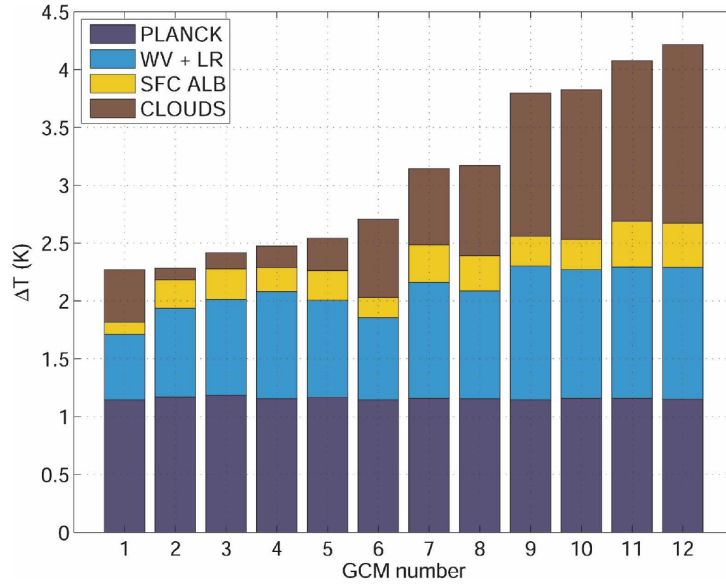


Figure 1.2: Equilibrium temperature change associated with the Planck response, water vapor, surface albedo and cloud feedback, computed for 12 CMIP3/AR4 calculations for a  $2\times\text{CO}_2$  forcing (Dufresne and Bony, 2008).

concentration. By deriving the ECS, it is possible to calculate the strength of the feedback processes in the system. The best estimate of the ECS based on the energy budget from the recent decade is 2.0 K, with a 5–95 % confidence interval from 1.2 to 3.9 K (Otto et al., 2013). Although this large uncertainty range has not narrowed in the last 40 years, our understanding about the factors controlling the ECS has been improved (Bony et al., 2015). In order to better understand the ECS uncertainty, different feedback parameters were defined. They describe the adjustment of the surface temperature in response to a particular forcing.

Fig. 1.2 shows the ECS for 12 different GCM runs decomposed into four different feedbacks. While the Planck and WV response dominate the absolute ECS, the intermodel differences are mainly due to variations in the cloud response to warming and the climate feedback (Dufresne and Bony, 2008). The net effect of clouds, including shortwave (SW) and longwave (LW) radiation, is to cool the planet by  $\sim 20 \text{ W m}^{-2}$  (Allan, 2011). In all recent GCM calculations, however, cloud feedbacks are positive since cooling of the planet is reduced (Zelinka et al., 2012). Clouds can adjust in different complex ways, depending on the cloud type and altitude, albeit the large spread in net cloud feedback is due to uncertainties in the estimation of low cloud changes (Zelinka et al., 2013). Thus, there is a great need to further investigate the physical processes of low-level clouds to better quantify the uncertainties in satellite observations as well as atmospheric and climate models.

### 1.3 Satellite remote sensing of clouds

Passive imaging radiometers on meteorological satellites measure radiances in multiple spectral bands at TOA. These radiances are reflected or emitted by the Earth's surface, clouds and different particles or molecules in the atmosphere. Satellites can be divided into geostationary and polar-orbiting. Geostationary satellites are positioned in the geostationary orbit about 36000 km above the equator and follow the direction of the Earth's rotation with the same speed. Thus, they continuously observe the same region of the globe. Polar-orbiting satellites, on the other hand, rotate at a fixed path, with high inclinations to the Earth's rotation, passing across high latitudes near the poles. With a distance of only 700 to 800 km to the Earth's surface they yield a higher spatial resolution. Polar-orbiting satellites measure polar regions several times a day, but lower latitudes generally only twice a day. In contrast, geostationary satellites with very high repeat cycles of a few minutes have the capability to observe and track clouds from their early developing stage onwards, and are thus the focus of this thesis.

The interpretation of satellite measurements relies on radiative transfer model calculations to relate cloud microphysical characteristics to radiances reaching the TOA from a particular cloud (Minnis et al., 1998). For collecting and analyzing satellite radiance data to investigate the global cloud property distributions, Schiffer and Rossow (1983) established the International Satellite Cloud Climatology Project (ISCCP) as part of the World Climate Research Programme (WCRP). The ISCCP cloud analysis involves the separation of image pixels into clear sky and cloudy, the radiative model analysis and the statistical analysis, merging cloud data from different satellites on a 30 km pixel resolution (Rossow and Garder, 1993). Nakajima and King (1990) introduced a method to determine the optical thickness and droplet effective radius of water clouds from reflection function measurements at two different wavelengths. This popular method is still used at the present day in numerous cloud property retrievals. The accuracy of retrieved cloud properties has improved during the last years due to advanced satellite instruments. If cloud properties retrieved from satellites are compared to model simulations, large uncertainties arise, particularly for low-level broken clouds with a high spatiotemporal variability (e.g., Marshak et al., 2006; Koren et al., 2008; Wolters et al., 2010; Horváth et al., 2014). These studies demonstrate that more research is needed to improve our knowledge of retrieval uncertainties and satellite sensor limitations. A more detailed view on these uncertainties is given in section 2.4.

## 1.4 Representation of convective clouds in atmospheric models

Due to the large range of relevant spatiotemporal scales, convective clouds cannot be explicitly resolved in atmospheric models. The impact of these unresolved processes on model variables like air motion, temperature, heat transfer, solar radiation and humidity has to be considered by parameterization schemes. Particularly cloud microphysical parameterizations play a key role in understanding latent heating and cooling, convection, precipitation, cloud-radiative and cloud-aerosol-precipitation interaction processes (Arakawa, 2004). All microphysical models can be basically categorized into two groups, bulk schemes and spectral (bin) microphysical schemes. Bulk schemes are commonly used in mesoscale models and are relatively cheap in computational costs, because all microphysical processes are described in terms of integral parameters. In contrast, bin microphysical models divide particles into different size bins and calculate the evolution of droplets in each size bin separately (Khain et al., 2000).

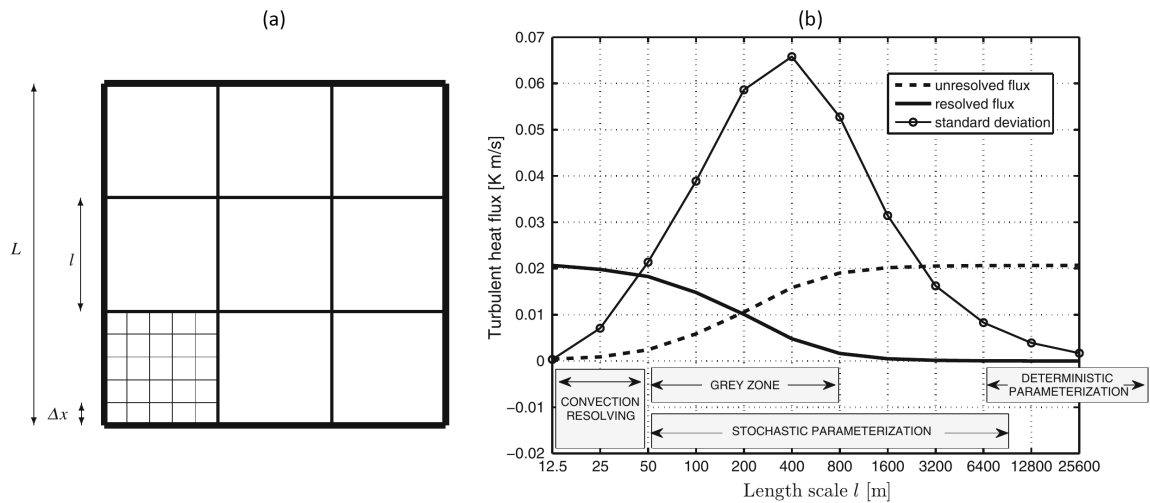


Figure 1.3: (a) Three length scales of an atmospheric model with different grid resolutions of  $L=25.6$  km (length scale of deterministic parameterizations in NWP models),  $l=1.6$  km (length scale where stochastic parameterizations are required) and  $\Delta x=50$  m (length scale of LES simulations) (Dorrestijn et al., 2012). (b) Decomposition of the resolved and unresolved turbulent fluxes in relation to the grid resolution  $l$  for the full  $25.6 \times 25.6$  km<sup>2</sup> domain shown in (a). The solid dotted line represents the standard deviation of the unresolved fluxes.

One very important characteristic of atmospheric models is their grid resolution. The higher the grid resolution in general, the more realistically can cloud microphysical and dynamical processes be simulated. To resolve convective clouds realistically, an atmospheric model with a grid resolution of at least 100 m is required (Dorrestijn et al., 2012). But a high grid resolution does not solve every problem. Barthlott and Hoose (2015) stated that more sophisticated parameterizations for boundary layer turbulence and cloud microphysics are also required to improve the representation of convective clouds in high resolution models.

Fig. 1.3 indicates the so-called grey zone between 50 m and 800 m grid resolution where resolved and unresolved turbulent heat fluxes are of the same order of magnitude. The standard deviation of the unresolved fluxes is very large in this gray zone, which demonstrates the difficulty to construct reliable parameterizations (Dorrestijn et al., 2012). This standard deviation remains large up to 10 km and indicates that stochastic parameterizations are most appropriate in this range. They also found that unresolved fluxes above 10 km grid resolution can be determined by using deterministic parameterizations. For grid resolutions lower than 50 m, unresolved fluxes are almost zero, because convection processes are largely resolved.

Current operational numerical weather prediction (NWP) models for limited regions reach 1 km resolution, but are still too coarse to resolve convection. Large eddy simulations (LES) are resolving a large part of the convection and turbulence due to their high grid resolution of usually 1 to 100 m. However, due to their high computational costs, such simulations are basically run using idealized setups (e.g., with periodic boundary conditions and without realistic land surface models) and are performed for small regions (e.g., Heus et al., 2010), which complicates their comparison with observational data. Due to the increasing capacity of supercomputers, large domain simulations at a cloud resolving scale are becoming feasible, and show for example a better timing of the diurnal cycle of convection (e.g., Hohenegger et al., 2008; Schlemmer and Hohenegger, 2014).

## 1.5 Objectives

The overall aim of the present thesis is an in-depth characterization of the spatiotemporal evolution of convective cloud fields with the Spinning Enhanced Visible and Infrared Imager (SEVIRI) on-board the geostationary Meteosat Second Generation (MSG) satellite and its applicability towards model evaluation. A further goal is to establish appropriate metrics to evaluate the representation of convective cloud fields in the high resolution model ICON-LEM and to characterize convective



cloud fields across different spatial scales. While polar-orbiting satellites like MODIS can resolve finer spatial cloud structures due to their higher spatial resolution, only geostationary satellites like Meteosat have the capability to observe and track clouds from their early developing stage onwards (see section 1.3). From the modeling perspective, simulations with at least 100 m grid resolution are required to resolve convective clouds realistically (Dorrestijn et al., 2012), which are however very expensive in computational costs if a large domain is considered (see section 1.4). Both perspectives, Meteosat observations and high resolution simulations of convective clouds will be considered and compared in the present thesis.

A fundamental problem for the characterization of convective clouds with satellite observations is the separation between cloudy and cloud-free areas. To approach this issue and improve the detection of convective clouds from MSG, the first goal is to develop and evaluate a threshold-based cloud mask for the high resolution visible (HRV) channel of Meteosat SEVIRI with  $1 \times 1 \text{ km}^2$  spatial resolution. The aim of using the HRV channel is to study small-scale cloud features, like their horizontal dimensions, which cannot be resolved by Meteosat's low resolution channels ( $3 \times 3 \text{ km}^2$ ). Past studies suggested that the HRV channel contains important information for investigating the small-scale variability of convective clouds (e.g., Klüser et al., 2008; Deneke and Roebeling, 2010). Sophisticated algorithms are required in order to determine reliable thresholds for gray-level images (Kapur et al., 1985). The large variability in the surface reflectance will be considered by using a differencing approach to improve the contrast between clouds and the underlying surface (Minnis and Harrison, 1984; Ipe et al., 2003). We finally want to evaluate the ability of the HRV cloud mask to identify convective clouds by comparison with the operational cloud mask from EUMETSAT.

The second objective is to investigate suitable techniques and quantities for characterizing the spatiotemporal evolution of convective cloud fields from space. This characterization provides complementary information about the spatial structure as well as temporal changes of cloud reflectances and microphysical properties. The latter will serve as a fingerprint to the underlying dynamical and microphysical processes. Especially warm convective clouds induce unresolved reflectance variations, which cause high cloud property uncertainties (Han et al., 1994). Some of these uncertainties have been quantified already with ground based measurements (Roebeling et al., 2008), but such evaluations are challenging for warm convective clouds due to their rapid changes in space and time (Feijt and Jonker, 2000; Deneke et al., 2009). Observations with Meteosat offer the opportunity to investigate convective cloud life cycles adopting a Lagrangian perspective. Nowcasting convective initiation and tracking of deep convective cloud systems often rely on object-based approaches (e.g.,

Mecikalski and Bedka, 2006; Zinner et al., 2008; Senf et al., 2015). We are focusing, however, on warm convective clouds, which are changing too fast within a 5 min time span in order to apply object-based approaches. Consequently, we are aiming to find a sophisticated tracking algorithm, that is capable of considering the temporal change of spatial coherence of the horizontal cloud field structure in sequential satellite images. While the Eulerian perspective includes advective and convective affected processes, the Lagrangian approach will provide the great opportunity to separate both.

The final aim is to apply these techniques when evaluating high resolution simulations and to investigate the spatiotemporal characteristics of warm convective cloud fields across different spatial scales to advance our understanding of the effects of small-scale cloud processes, which are underrepresented by geostationary satellite observations. Towards this goal, suitable metrics for comparing these high resolution model results with relatively coarsely resolved satellite observations are required. A better understanding of the scaling behavior of convective cloud scales at different spatial resolutions will further help to evaluate and improve stochastic parameterizations of cumulus convection in atmospheric models. Weisman et al. (1997) demonstrated a significant resolution sensitivity of the representation of convective cloud processes in a nonhydrostatic model with grid resolutions between 1 km and 10 km. We will consider simulations at a horizontal resolution up to 156 m to investigate the resolution sensitivity of the analyzed metrics. These simulations are based on the ICON-LEM model, which was developed within the High Definition Clouds and Precipitation for Climate Prediction (HD(CP)<sup>2</sup>) project (Dipankar et al., 2015; Heinze et al., 2017). Realistic ICON-LEM runs are performed on different grid spacings between 156 m and 625 m for the whole of Germany. The comparison of these high resolution model results with current satellite observations will further help to quantify satellite retrieval uncertainties and sensor limitations.

The main research questions for this thesis are formulated as follows:

1. How can we improve the representation of small-scale convective clouds using Meteosat observations?
2. What are suitable metrics for evaluating high resolution model simulations with relatively coarsely resolved satellite observations?
3. How sensitive are the spatiotemporal characteristics of convective cloud fields to the spatial resolution of a sensor or a model?

4. How can uncertainties of retrieved cloud properties and the instrumental limitations of MSG SEVIRI be quantified and which improvements are expected with respect to upcoming satellite missions?

The present thesis is structured as follows. The instrumental and model datasets are described in chapter 2 and 3. The results are presented in chapter 4 which is the cumulative part of the thesis including Bley and Deneke (2013); Bley et al. (2016) and Bley et al. (2017). The summary and conclusions including the answers of the research questions, which are formulated above, are given in chapter 5. In the following outlook, the implications for future satellite missions and model studies are discussed.



## 2 Instruments and related datasets

### 2.1 The Meteosat SEVIRI instrument

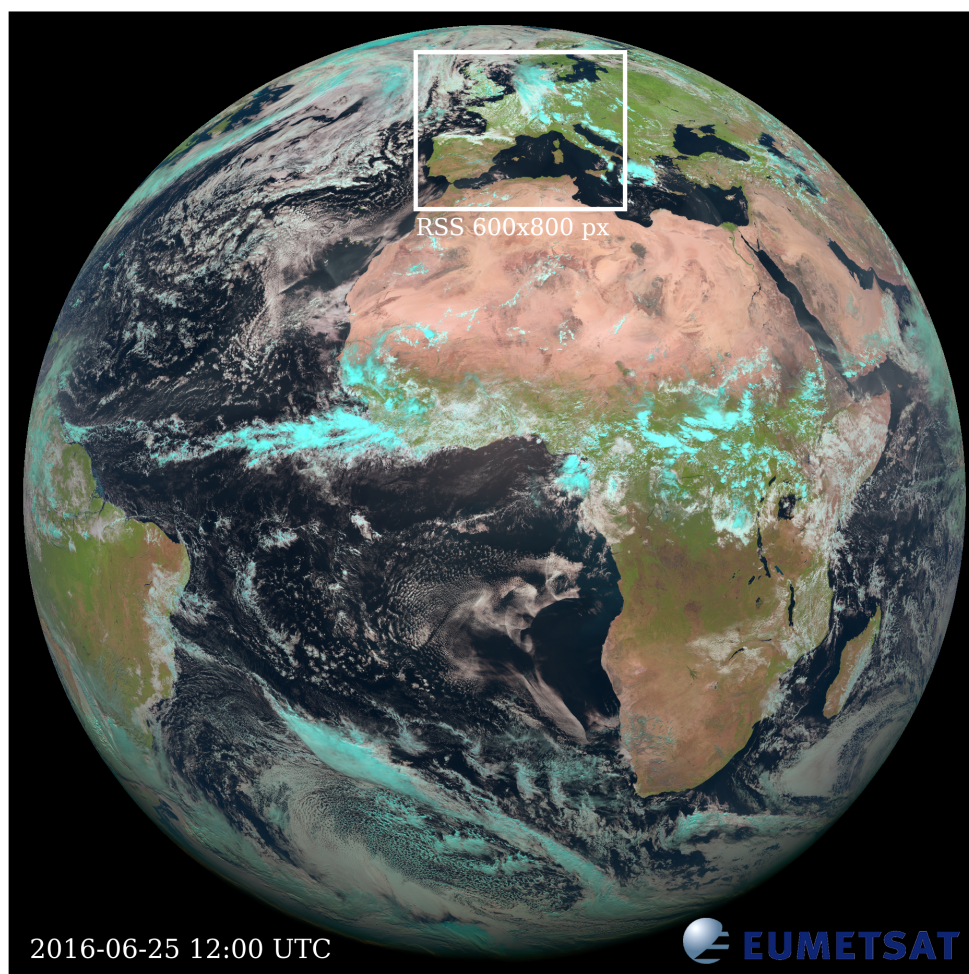


Figure 2.1: SEVIRI Full disk red-green-blue (RGB) natural color image following the Lensky and Rosenfeld (2008) method. Data for this thesis is taken from the rapid scan service (RSS), which covers a sub region of the full disk from approximately  $15^{\circ}$  to  $70^{\circ}$  N. This smaller area leads to a higher repeat cycle of 5 min instead of 15 min. The white rectangle marks a region over Central Europe, which is chosen for this thesis.

Nr.	Channel	Spectral band ( $\mu\text{m}$ )			Main gaseous absorber or window
		$\lambda_{min}$	$\lambda_{cen}$	$\lambda_{max}$	
01	VIS0.6	0.56	0.635	0.71	window
02	VIS0.8	0.74	0.81	0.88	window
03	NIR1.6	1.50	1.64	1.78	window
04	IR3.9	3.48	3.90	4.36	window
05	WV6.2	5.35	6.25	7.15	water vapour
06	WV7.3	6.85	7.35	7.85	water vapour
07	IR8.7	8.30	8.70	9.10	window
08	IR9.7	9.38	9.66	9.94	ozone
09	IR10.8	9.80	10.80	11.80	window
10	IR12.0	11.00	12.00	13.00	window
11	IR13.4	12.40	13.40	14.40	CO <sub>2</sub>
12	HRV	broadband ( $\sim 0.4\text{--}1.1$ )			window / water vapour

Table 2.1: Spectral channel characteristics of SEVIRI providing central, minimum and maximum wavelength of the channels and whether the channel is an absorbing or a window channel (Schmetz et al., 2002).

The Spinning Enhanced Visible and Infrared Imager (SEVIRI) is a passive instrument that operates onboard the Meteosat Second Generation (MSG) satellites on the geostationary orbit (Schmetz et al., 2002). EUMETSAT is currently operating four MSG satellites – Meteosat-7, -8, -9 and -10, which are located 36000 km above the Equator. Meteosat-10 is currently the primary operational satellite, positioned at 0° E, and provides full disk images covering Africa and Europe every 15 min. Meteosat-9 is running the Rapid Scan Service (RSS) at 9.5° E and delivers images over a sub-region of the full disk with a repeat cycle of 5 min. This sub-region covers Europe with 5 min temporal resolution and thus serves as the main data basis for this thesis. Meteosat-8 is the back-up satellite for Meteosat-9 and -10. Meteosat-7 was shifted to 57° E for observations over the Indian Ocean.

SEVIRI as the main payload onboard the MSG satellites provides 12 spectral channels: three solar (0.6, 0.8 and 1.6  $\mu\text{m}$ ), eight thermal infrared (IR) (3.9, 6.2, 7.3, 8.7, 9.7, 10.8, 12.0 and 13.4  $\mu\text{m}$ ) and one broadband high-resolution visible (HRV) (0.4–1.1  $\mu\text{m}$ ) (Tab. 2.1).

Fig. 2.1 shows one example RGB image taken by Meteosat-10 on 25 June 2016. The nadir spatial resolution is 1×1 km<sup>2</sup> for its HRV channel and 3×3 km<sup>2</sup> for the other 11 channels. The true optical resolution, however, is lower by a factor of 1.6 for both the high resolution and the low resolution channels (Schmetz et al., 2002). The spatial resolution is further decreased with an increasing distance to the nadir satellite point. This effect has, particularly for Meteosat-9 and over Central Europe,

almost no influence on the East-West pixel length, but is significant for the North-South pixel length. This leads to an anisotropic pixel resolution of  $1.2 \times 2 \text{ km}^2$  for the HRV channel and  $3.6 \times 6 \text{ km}^2$  for the narrow-band channels. The HRV channel is of particular interest for this thesis. The level 1.5 image data of MSG is received and processed by the satellite remote sensing group at the Leibniz Institute for Tropospheric Research (TROPOS) in Leipzig.

## 2.2 KNMI Cloud Physical Properties retrieval

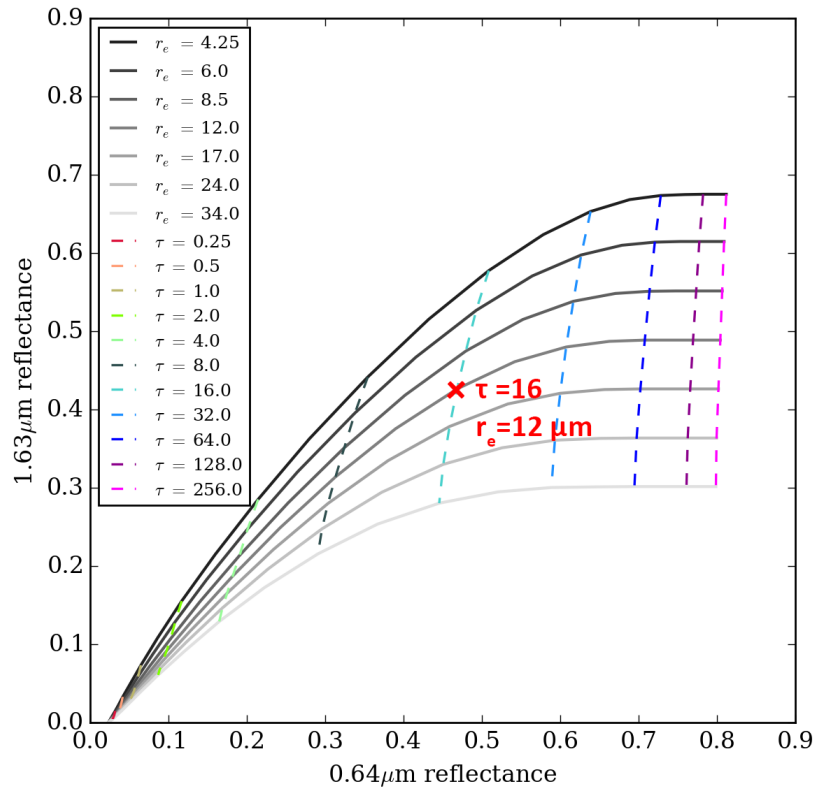


Figure 2.2: Look-up table for calculation of  $\tau$  and  $r_e$  from the KNMI DAK radiative transfer simulations. Solid lines are related to  $r_e$ , vertical dashed lines correspond to  $\tau$ . The red cross demonstrates an example cloudy pixel with  $r_e = 12 \mu\text{m}$  and  $\tau = 16$ .

The fundamental concept behind retrieving cloud properties from satellite is that the optical thickness is closely related to the cloud reflectance at a nonabsorbing channel in the visible wavelength ( $0.6 \mu\text{m}$  for SEVIRI), while the cloud droplet effective radius is strongly related to the reflectance at an absorbing channel in the near infrared region ( $1.6 \mu\text{m}$  for SEVIRI) (Roebeling et al., 2006). The relation between the cloud optical thickness  $\tau$ , the cloud droplet effective radius  $r_e$  and the reflectance in the two channels



is simulated by radiative transfer calculations and stored in look-up tables (Fig. 2.2). For this study, the Cloud Physical Properties (CPP) retrieval is used, which was developed at the KNMI (Roebeling et al., 2006) in the framework of the Satellite Application Facility on Climate Monitoring (CM SAF) (Schulz et al., 2009). The Doubling Adding KNMI (DAK) radiative transfer model is considered to generate the look-up tables in the CPP-retrieval (Roebeling et al., 2006).

The primary cloud property for this thesis is the liquid water path (LWP), which represents the vertical integrated cloud water content between cloud base and cloud top. Passive satellite instruments, however, retrieve cloud parameters such as the LWP in a rather indirect way. The estimation of LWP from  $r_e$  and  $\tau$  requires assumptions about the vertical cloud structure. Usually, the liquid water content (LWC) and  $r_e$  are assumed to be constant with height, resulting in the relation

$$LWP = \frac{2}{3} \cdot \rho_w \cdot \tau \cdot r_e. \quad (2.1)$$

where  $\rho_w$  is the density of liquid water (Stephens, 1978; Roebeling et al., 2008). However, Wood and Hartmann (2006) demonstrated that observations of boundary layer clouds often show a linear increasing LWC with cloud height. This model results in the relationship

$$LWP = \frac{5}{9} \cdot \rho_w \cdot \tau \cdot r_e. \quad (2.2)$$

to estimate the LWP, assuming adiabatic clouds (see Wood and Hartmann, 2006, for further discussion). Since a linear increase of LWC is typically found for warm convective clouds (Merk et al., 2016), we use the equation 2.2 for the calculation of LWP.

$\tau$  and  $r_e$  are estimated from the simulated look-up tables. Fig. 2.2 illustrates an example look-up table calculated with the KNMI DAK radiative transfer simulations with the  $0.6 \mu\text{m}$  as nonabsorbing and the  $1.6 \mu\text{m}$  as the absorbing channel. The red cross illustrates one example cloud pixel with  $\tau=16$  and  $r_e=12 \mu\text{m}$ . The retrieval of  $r_e$  is related to the upper part of the cloud (Platnick, 2001). Fig. 2.2 also shows that the curves of  $r_e$  are lying very close to each other for optically thin clouds, which indicates large uncertainties in that region. For these small  $\tau$ , the relation between  $r_e$  and the  $1.6 \mu\text{m}$  reflectance is highly nonlinear which further influences the retrieval accuracy (Cahalan et al., 1994b). An in-depth description of the retrieval uncertainties follows in section 2.4.



## 2.3 NWC SAF cloud products

The Satellite Application Facility on Support to Nowcasting and Very Short Range Forecasting (NWC SAF) provides algorithms to improve the use of data from the Meteosat satellites which is relevant for Nowcasting applications. Nowcasting and very short range forecasts are essential for the safety of our daily life. The MSG SEVIRI images are supporting many nowcasting applications, like monitoring of convection which can lead to severe convective thunderstorms, or detection and tracking of dust storms, volcanic ash and fog. From a large variety of cloud products, the cloud mask (CM) and cloud type (CT) (Derrien and Le Gléau, 2005) as well as the cloud top height (CTH) (Derrien, 2012) and high resolution wind vectors (HRW) (García-Pereda, 2013) are used in this thesis.

The NWC SAF provides the software packages with full default configuration data for free. Please note that the default configuration was partially adjusted to focus the calculation of the HRW product on the textural patterns of the HRV channel. The CM algorithm identifies cloudy and cloud-free regions in Meteosat images and uses different tests applied to various channel combinations for each pixel of a current image. Complementary to these pixel-based tests, some spectral combinations of channels are applied to the temporal and spatial coherence of the image, to improve the detection of low cumulus clouds (Derrien and Le Gléau, 2005). Some IR tests further require NWP parameters from the European Center for Medium range Weather Forecasting (ECMWF) model like surface temperature, humidity and water vapor content. Vertical NWP profiles are also used as input for the very fast radiative transfer model (RTTOV) to simulate the clear sky radiance at TOA. All these tests, assumptions and input parameters from different models demonstrate the complexity of the CM algorithm.

The HRW product represents the basis for the Lagrangian analysis of the Meteosat observations (Bley et al., 2016). It is based on a cross-correlation technique and contains atmospheric motion vectors (AMVs) for cloudy pixels characterized by particular tracers that can be matched in subsequent satellite images. Please note that the default configuration for the HRW product was adjusted to improve the determination of low-level cloud motions, which are usually rejected by the stringent quality tests in the default configuration (Bedka and Mecikalski, 2005). This was realized by considering more tracers that are used for the calculation and by slightly reducing the quality threshold (Bley et al., 2016).

## 2.4 Uncertainties in cloud properties retrieved from geostationary satellites

The derived optical and microphysical cloud properties from geostationary satellite retrievals are accompanied by high uncertainties, especially for warm convective clouds. These uncertainties complicate the evaluation of modeled cloud properties with observations (Jonkheid et al., 2012). They showed that the CPP retrieval of the cloud water path (CWP) is very sensitive to the assumptions made in the code. Retrieval errors of the CWP are found to be generally small for homogeneous single layer clouds, but are substantially increasing up to 40–80 % in multi-layer cloud conditions with ice and water within one pixel (Jonkheid et al., 2012). This is due to the fact that clouds are assumed to be plane-parallel, in a multi-layered Rayleigh scattering atmosphere and that the cloud water is horizontally uniformly distributed within the cloud (Roebeling et al., 2006). In the real atmosphere, this is evidently not the case. Especially convective clouds have a very heterogeneous structure, which can only be coarsely resolved from geostationary satellite observations. The CPP retrieval of  $\tau$  and  $r_e$  is conducted on a pixel basis, and only for those that are classified as cloudy by the NWC SAF cloud mask. Ignoring the sub-pixel variability of the cloud reflectances leads to large uncertainties in the retrieval of  $\tau$  and  $r_e$  (e.g., Cahalan et al., 1994a; Davis et al., 1996; Platnick, 2001; Roebeling et al., 2006; Marshak et al., 2006; Zinner and Mayer, 2006; Várnai and Marshak, 2007; Wolters et al., 2010; Zhang and Platnick, 2011; Horváth et al., 2014; Cho et al., 2015; Zhang et al., 2016). This large number of studies demonstrates the importance of considering and quantifying these effects for reliable physical interpretations.

Cahalan et al. (1994b) described the influence of averaging the unresolved cloud reflectance variations on the derived  $\tau$  and  $r_e$  due to the nonlinear relation between the measured reflectance and the related  $\tau$ . Fig. 2.3 illustrates this effect for look-up tables based on a channel combination of the 0.8  $\mu\text{m}$  and 2.13  $\mu\text{m}$  bands (Zhang et al., 2016). In this example, two clouds with different  $\tau=2.8$  and  $\tau=30.8$  but the same  $r_e=8 \mu\text{m}$  are assumed to fill the footprint of one pixel. The retrieved  $\tau=10.8$  based on the average reflectance is substantially smaller than the arithmetic average of the real unresolved  $\tau$ , leading to  $\tau=16.8$ . This plane-parallel albedo bias generally causes much smaller  $\tau$  for satellite observations with relatively coarse spatial resolution compared to retrieved values from higher resolution observations such as the MODIS instrument or the Advanced Very High Resolution Radiometer (AVHRR) (Roebeling et al., 2006). They also reported that differences in the derived LWP are usually smaller due to a compensation of slightly larger  $r_e$  resulting from the plane-parallel albedo bias that is

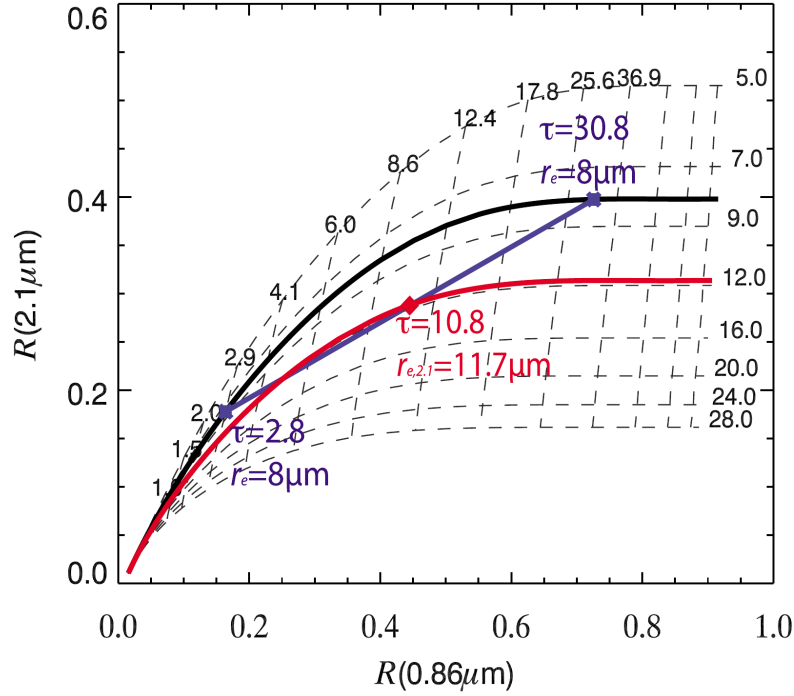


Figure 2.3: Theoretical case to illustrate the nonlinearity effect in  $r_e$  retrievals resulting from sub-pixel cloud inhomogeneity (Zhang et al., 2012). Numbers on top of the Nakajima King look-up table correspond to  $\tau$ , numbers on the right represent  $r_e$ .

also shown in Fig. 2.3. The influence on  $r_e$  can be explained by the retrievals of  $r_e$  and  $\tau$ , which are not independent (Marshak et al., 2006).

Such sub-pixel cloud reflectance variations can be also caused by shadowing effects due to surrounding pixels. These 3-D radiative effects, however, cannot be explained by the 1-D radiative transfer theory (Marshak et al., 2006). The retrieval accuracy is further reduced in multi-layer cloud conditions. Watts et al. (2011) used an optimal estimation method to develop a two-layer cloud retrieval scheme with multispectral channels from MSG SEVIRI. A recent study by Sourdeval et al. (2016) describes an algorithm to retrieve cloud ice and water properties simultaneously with the capability to determine multi-layer cloud properties.

Since the focus of the present thesis is on single-layer convective clouds that are purely liquid, such effects are neglected. In contrast, large retrieval uncertainties are expected for this type of clouds due to the coarse spatial resolution of Meteosat, which was already described as the plane-parallel albedo bias. Consequently, the influence of the spatial resolution on the statistical representation of warm convective clouds needs to be quantified. Geostationary satellite retrievals generally underestimate the LWP

especially for broken convective clouds due to their coarse resolution (e.g., Wolters et al., 2010; Marshak et al., 2006). This effect is also influenced by the viewing angle of the satellite instrument (Horváth et al., 2014). Due to the relatively high viewing angle of  $60^\circ$  for observations over Central Europe, this influences not only the retrieval accuracy but also the cloud fraction (CF). These effects are quantified and discussed in Bley et al. (2017).

## 3 Model data

### 3.1 ICON-LEM high resolution simulation

The ICON-LEM model is based on the unified modeling system for climate and numerical weather forecast ICON (ICOsahedral Nonhydrostatic) developed by the German Weather Service, which is extended to a large eddy simulation that partially resolves turbulence and convection. For the unresolved part, a new three-dimensional turbulence scheme based on the classical Smagorinsky scheme has been implemented and is applied to the prognostic winds, potential temperature, specific humidity and specific cloud liquid water content (Dipankar et al., 2015). The cloud microphysics are parameterized by the two-moment mixed phase bulk microphysical scheme after Seifert and Beheng (2005). The cloud fraction scheme does not account for fractional cloudiness at the subgrid scale (Heinze et al., 2017). To keep the integration of the physical parameterizations stable, horizontal diffusion is added. ICON-LEM is used in a real-case configuration with prescribed lateral boundary conditions and a nesting approach (Heinze et al., 2017). ICON-LEM is not running in a semi-idealized setup like the PARallelized Large Eddy simulation Model (PALM) but uses the realistic land surface model Terra which is also used in COSMO-DE (Heinze et al., 2017). Each simulation day is initialized at 00 UTC from the operational COSMO-DE analysis and runs for 24 h.

Within the HD(CP)<sup>2</sup> project, ICON-LEM performed four simulations for the 24–26 April and the 2 May 2013 with a very high spatial resolution of 156 m for a large domain covering Germany (Fig. 3.1). Grid refinement steps are taken from 624 m to 312 m and to 156 m in the innermost domain (Heinze et al., 2017). As the grid spacings of the ICON-LEM runs are somewhat higher than those used typically in LES models for cloud studies, these runs could also be classified as “near-LES” experiments (Mechem et al., 2012). The simulations were originally performed on a 100 m icosahedral grid, but regridded afterwards on a regular grid to facilitate the model evaluation with observations. The resulting spatial resolution is related to the square root of the mean cell area in the icosahedral grid, which is equivalent to about 1.5 times the corresponding resolution in a regular grid (Heinze et al., 2017). ICON-LEM uses 150 vertical model

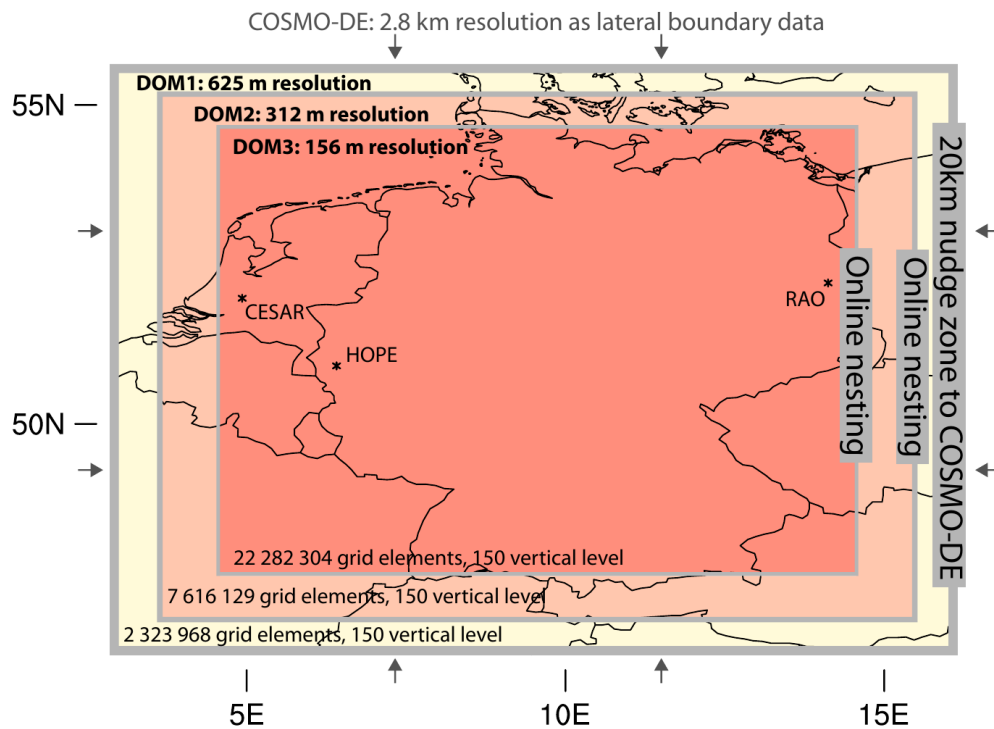


Figure 3.1: ICON-LEM domain and its two nests with grid refinement. The open lateral boundaries are relaxed towards COMSO-DE analysis (Heinze et al., 2017).

layers with a decrease of the spatial resolution towards the domain top and with 20 layers representing the lowest 1000 m.

Apart from the great challenge to carry out such high performance simulations at the German Supercomputing Centre (DKRZ), it also took massive storage capacities to write the model results to files (Heinze et al., 2017). A large number of approximately 3.3 billion grid cells have been processed with a model run time step of 0.75 sec (Heinze et al., 2017). Keeping this in mind, it was a great challenge to analyze the data output. 50 terabyte of data output were generated for one day of simulation. The three-dimensional model variables were mapped to a regular grid with 1 km grid spacing and written out every hour. Variables on the unstructured high resolution model grid were written to files only once or twice a day during MODIS overpasses. The two-dimensional data output for the cloud properties is archived at 156 m, 312 m and 625 m grid spacing and a 1 sec time frequency, albeit sub-sampled to 1 min time steps for the present study to reduce the computing time for the analysis.

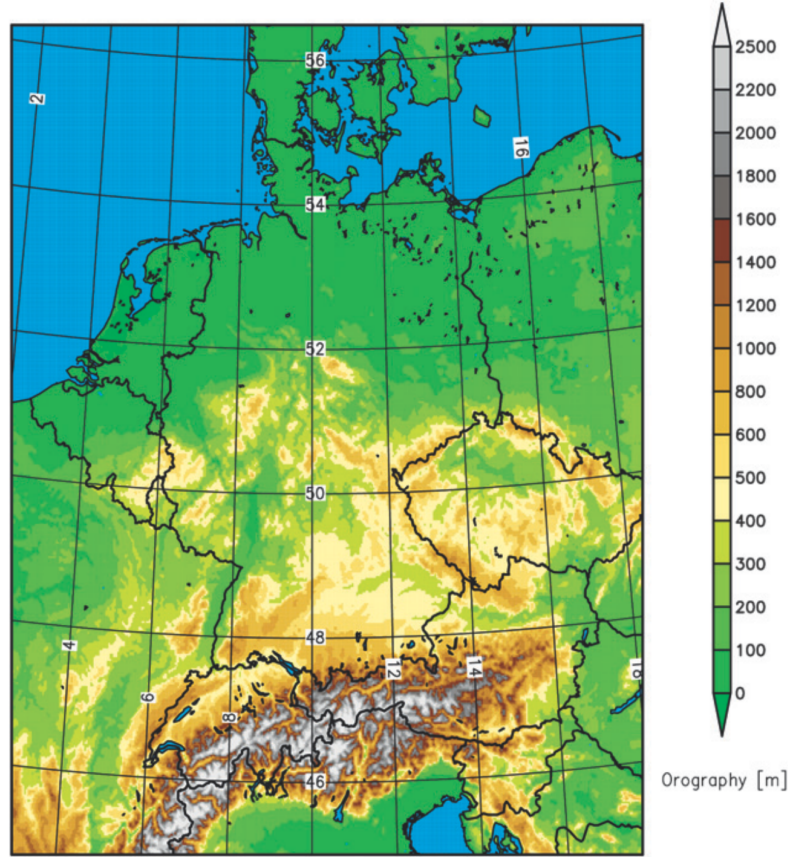


Figure 3.2: Domain covered by the COSMO-DE model with  $421 \times 461$  grid points (Baldauf et al., 2011).

## 3.2 COSMO-DE

The Consortium for Small Scale Modelling (COSMO-DE) is a numerical weather prediction model which is operating at the German Weather Service (DWD). It runs on a convection-permitting scale with 2.8 km grid resolution and is thus able to predict deep convection explicitly (Baldauf et al., 2011). In contrast to NWP models in the past, COSMO-DE partially resolves convective cloud structures by using a Runge-Kutta method. Small-scale shallow convection is parameterized with the Tiedtke (1989) scheme, that is also used in the ICON-LEM model. In comparison to ICON-LEM, which uses the two-moment cloud microphysical scheme after Seifert and Beheng (2005), however, COSMO-DE parameterizes the cloud microphysics with a one-moment Lin et al. (1983) type scheme that is extended by a graupel class. COSMO-DE uses 50 vertical model layers with a stretched level spacing at the domain top. While the improved microphysical scheme leads to a successful prediction of deep convection, Baldauf et al. (2011) describe the Planetary Boundary Layer (PBL)

scheme as the most problematic model deficit in order to better resolve small-scale convection in the boundary layer. They further state that an improved vertical resolution is required to improve the representation of the PBL. The domain covered by the COSMO-DE model Fig. 3.2 completely overlaps the domain of the ICON-LEM model, which facilitates inter-model comparisons.

For evaluation of the ICON-LEM model, COSMO-DE simulations were carried out with the operational configuration, but with the same Seifert and Beheng (2005) scheme which was used in ICON-LEM. The cloud liquid and ice water content contain the grid scale and subgrid scale cloud water and ice, as used in the radiation scheme.



## 4 Results and discussion

### 4.1 First publication: A threshold-based cloud mask for the high-resolution visible channel of Meteosat Second Generation SEVIRI

The content of this chapter has already been published in the manuscript “A threshold-based cloud mask for the high-resolution visible channel of Meteosat Second Generation SEVIRI” by Sebastian Bley and Hartwig Deneke in the journal “Atmospheric Measurement Techniques” in 2013 with the doi: 10.5194/amt-6-2713-2013.

Reprinted with permission by the authors from Atmospheric Measurement Techniques. 2013, 6, 2713–2723.



# A threshold-based cloud mask for the high-resolution visible channel of Meteosat Second Generation SEVIRI

S. Bley and H. Deneke

Leibniz Institute for Tropospheric Research (TROPOS), Permoserstraße 15, 04318 Leipzig, Germany

Correspondence to: S. Bley (bley@tropos.de)

Received: 18 January 2013 – Published in Atmos. Meas. Tech. Discuss.: 20 March 2013

Revised: 19 August 2013 – Accepted: 2 September 2013 – Published: 18 October 2013

**Abstract.** A threshold-based cloud mask for the high-resolution visible (HRV) channel ( $1 \times 1 \text{ km}^2$ ) of the Meteosat SEVIRI (Spinning Enhanced Visible and Infrared Imager) instrument is introduced and evaluated. It is based on operational EUMETSAT cloud mask for the low-resolution channels of SEVIRI ( $3 \times 3 \text{ km}^2$ ), which is used for the selection of suitable thresholds to ensure consistency with its results. The aim of using the HRV channel is to resolve small-scale cloud structures that cannot be detected by the low-resolution channels. We find that it is of advantage to apply thresholds relative to clear-sky reflectance composites, and to adapt the threshold regionally. Furthermore, the accuracy of the different spectral channels for thresholding and the suitability of the HRV channel are investigated for cloud detection. The case studies show different situations to demonstrate the behavior for various surface and cloud conditions.

Overall, between 4 and 24 % of cloudy low-resolution SEVIRI pixels are found to contain broken clouds in our test data set depending on considered region. Most of these broken pixels are classified as cloudy by EUMETSAT's cloud mask, which will likely result in an overestimate if the mask is used as an estimate of cloud fraction. The HRV cloud mask aims for small-scale convective sub-pixel clouds that are missed by the EUMETSAT cloud mask. The major limit of the HRV cloud mask is the minimum cloud optical thickness (COT) that can be detected. This threshold COT was found to be about 0.8 over ocean and 2 over land and is highly related to the albedo of the underlying surface.

## 1 Introduction

The effect of clouds on radiative fluxes depends on cloud type and can vary strongly both in space and time. Accurate information about the physical and radiative properties of clouds is necessary to determine the role of clouds in the climate system including their response to anthropogenic forcings (e.g., Forster et al., 2007).

Geostationary satellite imagers such as Meteosat SEVIRI (Spinning Enhanced Visible and Infrared Imager) are well-suited to monitor the temporal development of clouds, and to resolve their diurnal cycle fully over land and ocean (Roebeling and van Meijgaard, 2009). The spatial resolution of SEVIRI's narrowband channels ( $3 \times 3 \text{ km}^2$ ) lags behind that of polar orbiting imagers such as MODIS ( $1 \times 1$  down to  $0.25 \times 0.25 \text{ km}^2$ ) and AVHRR ( $1.1 \times 1.1 \text{ km}^2$ ), which limits its ability to resolve small-scale structures. SEVIRI does however have a high-resolution visible (HRV) channel with a nadir resolution of  $1 \times 1 \text{ km}^2$ .

The HRV channel contains important information for studying the small scale variability of clouds and the underlying surface (e.g., Klüser et al., 2008; Deneke and Roebeling, 2010). The study of Derrien et al. (2010a) improves the detection of small-scale low clouds by use of the HRV channel. The HRV channel reflectance was also used by Carbajal Henken et al. (2011) for the detection of deep convective clouds. Nevertheless, few operational products based on the HRV channel are available, which is a significant hurdle for use of its finer spatial resolution for scientific studies and applications.

The estimation of cloud and/or surface properties from multispectral satellite images requires the classification of pixels into cloud-free and cloudy classes as an initial step.

Most cloud detection algorithms described in the literature rely on a combination of threshold tests applied to different spectral channels for this purpose. Rossow et al. (1989) present an overview of early methods chosen for cloud masking. These methods often exploit the fact that clouds generally appear brighter in solar channels due to reflection, and colder in infrared channels relative to cloud-free surfaces. In addition, spatial coherence tests are commonly used, as clouds are often more variable than the underlying surface (e.g., see Saunders and Kriebel, 1988). It should be noted that spatial coherence tests also rely on thresholds for identifying regions with high variability.

Cloud masking is one particular case of object identification by thresholding, and can be described mathematically by considering the grey-level histograms based on specific channel radiances. Thresholds are selected to separate the histograms for the cloud-free and cloudy pixels of a satellite image best. Suitable thresholds for satellite channels are often selected by experts (e.g., Saunders and Kriebel, 1988). As an alternative, automatic statistical methods can be applied to select optimal thresholds. Here, methods that make use of a training data set for threshold selection (supervised methods) need to be differentiated from those that select thresholds based on intrinsic properties of the data set (unsupervised methods). Yang et al. (2007) have investigated several algorithms for unsupervised threshold selection, and have determined the most accurate ones for application to cloud masking for the multi-angle imaging spectroradiometer (MISR) over land. Regardless of the method, independent reference data are needed to establish the accuracy of threshold-based classification methods.

The goal of the present paper is to develop a cloud mask based on the HRV channel, which exploits its high spatial resolution, and is suitable to study small-scale features of clouds, including, for example, their horizontal dimensions. This does preclude the use of spatial coherence tests due to their non-local nature. Instead, a differencing approach using clear-sky composite reflectances as a background is adopted to improve the contrast between clear-sky and cloudy situations (e.g., Minnis and Harrison, 1984; Ipe et al., 2003). Nevertheless, a threshold test applied to a single visible channel cannot achieve the accuracy of other SEVIRI cloud masks that are based on multiple spectral channels. Instead of replicating other cloud mask algorithms, this HRV mask is designed as a complement to an existing cloud mask used as a reference for threshold selection and to estimate the mask's accuracy. The operational cloud mask product (CLM) by EUMETSAT's Meteorological Product Extraction Facility, which is based on the narrowband channels of SEVIRI (EUMETSAT, 2007), is a convenient choice for this purpose as it is distributed through the EUMETCast system together with the level 1.5 SEVIRI images, and it is used in our study.

This paper is structured as follows: in Sect. 2, a brief overview of the data sets used in our study, including the characteristics of the SEVIRI instrument, is given. This is

followed by Sect. 3, which describes our proposed cloud masking method. Section 4 presents results and discussions, followed by conclusions and an outlook in Sect. 5.

## 2 Data

### 2.1 Instrumental data

The current series of European geostationary satellites, Meteosat Second Generation (MSG), is operated by EUMETSAT. Its main payload is the the Spinning Enhanced Visible and Infrared Imager (SEVIRI), an optical imaging radiometer. Three MSG satellites, Meteosat-8 to Meteosat-10, were launched and are positioned in geostationary orbit at an altitude of 36 000 km above the Equator. Meteosat-9 observes the full disk of the earth as a primary geostationary service with a repeat cycle of 15 min. Meteosat-8 is currently used as a standby and operates the rapid-scan service covering Europe with a 5 min repeat cycle. Meteosat-10 was launched on 5 July 2012, and is currently in commissioning. A detailed description of MSG is given by Schmetz et al. (2002).

The SEVIRI instrument has 3 solar channels (0.6, 0.8 and 1.6  $\mu\text{m}$ ), 8 thermal infrared channels (3.9, 6.2, 7.3, 8.7, 9.7, 10.8, 12.0 and 13.4  $\mu\text{m}$ ) and one high-resolution visible channel (HRV) (0.4–1.1  $\mu\text{m}$ ). The nadir spatial resolution for SEVIRI's HRV channel is  $1 \times 1 \text{ km}^2$  and  $3 \times 3 \text{ km}^2$  for the other 11 channels. However, the true optical resolution is lower by a factor of about 1.6 for both high resolution and low-resolution (LRES) channels (Schmetz et al., 2002).

Only the 0.6, 0.8, 1.6, 8.7  $\mu\text{m}$  and HRV channels are considered in this study. The normalized spectral response functions of the narrowband solar and the broadband HRV channels are shown in Fig. 1.

The narrowband channels cover the full disk of the earth with  $3712 \times 3712$  pixels. At a 3-fold higher resolution, this results in a nominal image size of  $11\,136 \times 11\,136$  pixels for the HRV channel. However, the actual HRV channel coverage is only 5568 pixels in east–west direction. An upper region of 3072 scanlines with a fixed position is centered on Europe. The lower region consisting of 8064 scan lines follows the daily illumination. Only the upper region is considered in this study.

### 2.2 EUMETSAT cloud mask

The EUMETSAT cloud mask (CLM) is derived by the Meteorological Product Extraction Facility (MPEF) and utilizes a combination of several multi-spectral threshold tests grouped into different categories to distinguish between cloudy and cloud-free pixels (see EUMETSAT, 2007, for a detailed description of the algorithm). The CLM is an operational SEVIRI product and is derived every 15 min for the full disk. In the final product, each pixel is labeled either as 0 (clear-sky ocean), 1 (clear-sky land), 2 (cloudy) or 3 (no data). The EUMETSAT threshold tests involve almost every

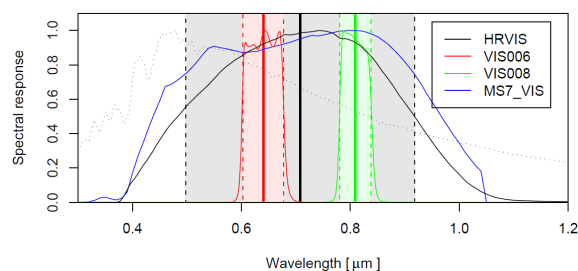


**Fig. 1.** Normalized spectral response functions of the Meteosat-9 SEVIRI radiometer for the 0.6  $\mu\text{m}$  (red), 0.8  $\mu\text{m}$  (green) and HRV (black) channels. The central wavelength of each channel is marked by a thick colored line, and the spectral region covered by the channel width has been shaded. The solar spectrum is added as a dotted line.

SEVIRI channel with the exception of channel 8 (9.7  $\mu\text{m}$ ), as it is mainly sensitive to tropospheric and stratospheric ozone and thus adds little additional information for cloud masking, and channel 12 (HRV), as it is not available for the full disk.

### 2.3 Study regions

To evaluate the threshold-based cloud mask algorithm and study its performance for different surface types and synoptic conditions, we have selected the following four regions in and around Europe: (1) Atlantic, (2) the Alps, (3) Upper Rhine Valley and (4) Spain (see Fig. 2). The four regions comprise  $192 \times 192$  HRV pixels (or  $64 \times 64$  LRES pixels) to provide enough data points to calculate representative histogram functions. This size has been chosen as a reasonable trade-off versus the advantage offered by a smaller size and thus a smaller surface variability. To illustrate the improvements gained by applying thresholds relative to a clear-sky composite, we have focused on regions with a relatively high spatial surface variability such as the Alps and the Upper Rhine Valley. Due to our future plans to investigate the diurnal cycle of shallow cumulus convection we use the Rapid Scan Service (RSS) of Meteosat over the European region. The presented algorithm is limited in terms of the surface albedo, which is discussed in Sect. 3 (Fig. 4).

## 3 Methods and algorithms

For applying a binary classification to separate cloudy and clear-sky pixels, we rely on the following simplified assumption. In general clouds have a higher HRV reflectance compared to the clear-sky surface and thus appear brighter. Counterexamples include snow-covered surfaces, enhanced clear-sky reflectances due to aerosols, and cloud shadows, but they are neglected here. A perfect classification would allow an exact separation between clear-sky and cloudy reflectances based on a single reflectance threshold.

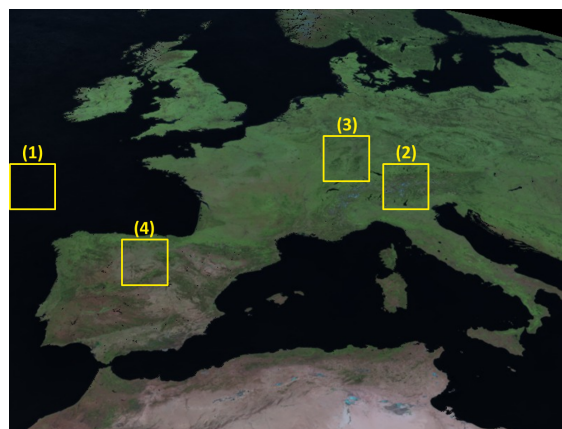


**Fig. 2.** Day natural color (RGB) clear-sky composite of Lensky and Rosenfeld (2008) based on clear-sky reflectances of the 0.6, 0.8 and 1.6  $\mu\text{m}$  channel. Median values of clear-sky reflectance over a period of 16 days (1–16 June 2011) and cloud-cleared with the EUMETSAT cloud mask are shown (at standard SEVIRI resolution). The following four regions used in our study are marked by boxes: (1) Atlantic, (2) the Alps, (3) Upper Rhine Valley and (4) Spain.

The first step in this study is the separation of clear-sky and cloudy HRV pixels based on the EUMETSAT cloud mask. The latter includes multiple solar and thermal threshold tests. As it is not based on a fixed reflectance threshold, clear-sky pixels can have a higher HRV reflectance than cloudy pixels. Consequently, there is an overlap between the histograms of the clear-sky and the cloudy reflectances (Fig. 3). The normalized frequency distribution of clear-sky and cloudy HRV reflectances are shown for the regions Spain (yellow), Upper Rhine Valley (green), the Alps (red) and Atlantic (blue). The clear-sky histograms have been calculated as a median value over a 16-day period (1–16 June 2011). Figure 3 shows the lowest clear-sky reflectance and lowest variability over the Atlantic region. The clear-sky reflectance histogram over Spain reveals a high value and simultaneously a high spatial variability. Readers should note the overlap between the clear and cloudy histograms.

Several reasons can cause the broadness of the clear-sky histogram and thus the overlap in the HRV reflectance histograms (Fig. 3). This includes spatial and temporal variability of the surface reflectance (e.g., due to changes in vegetation, atmospheric aerosols). Additionally undetected thin cirrus clouds with low visible reflectance can contaminate the HRV clear-sky histogram. This overlap is the major source of uncertainty for our cloud mask. The challenge is thus to reduce this overlap, and to find an optimal threshold to obtain the best classification.

One of the major problems that causes the overlap is the broadness of the cloudy histogram due to different cloud types with different COTs. This broadness is strongly related

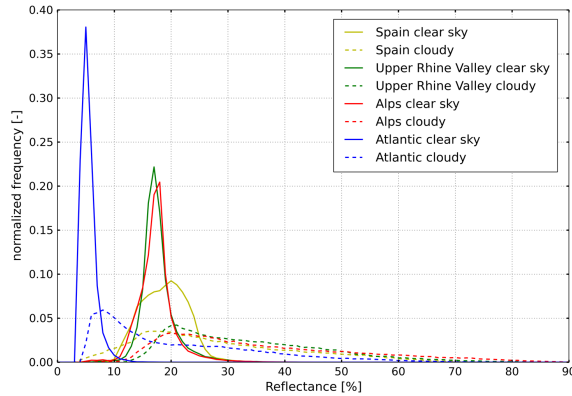


**Fig. 3.** Normalized frequency distribution of cloudy and clear-sky HRV reflectances over Spain (yellow), Upper Rhine Valley (green), the Alps (red) and Atlantic (blue) observed by MSG SEVIRI. Separation between cloudy (dotted line) and clear-sky (solid line) reflectances is based on EUMETSAT cloud mask. EUMETSAT cloud mask is upsampled to HRV resolution.

to the definition of the cloud the user wants to capture with his/her cloud mask. In our study it is related to the minimum COT that can be detected reliably by the HRV cloud mask depending on the underlying surface albedo. In order to quantify the accuracy of the cloud detection algorithm and the implication of the underlying surface, we calculate the minimum COT using a simple, qualitative model (Eq. 1 by Lacis and Hansen, 1974). The change in the planetary albedo due to the occurrence of clouds is based on an expression by Liou (1980) to take into account multiple scattering between the cloud and the underlying surface. Furthermore, no absorption within the cloud is considered in this formula:

$$A_P = A_C + R_S \cdot \frac{(1 - A_C)^2}{1 - R_S \cdot A_C}. \quad (1)$$

Thereby  $A_P$  is the change in the planetary albedo,  $A_C$  the cloud albedo and  $R_S$  the albedo of the underlying surface. The cloud albedo can be approximated by

$$A_C = \frac{\tau_c}{\tau_c + 7.7}, \quad (2)$$

where  $\tau_c$  is the cloud optical thickness (Lacis and Hansen, 1974). The statement of Eq. (1) is illustrated by Fig. 4 for four different COTs. The curves show the change in planetary albedo due to the occurrence of clouds with a particular COT from 0.2 to 2 over a surface with different clear-sky reflectances between 0 and 0.55.  $\delta$  (planetary albedo – surface albedo) indicates the accuracy of the threshold that is necessary to detect a cloud over a specific ground. The thin blue area (COT=0.2–0.5) illustrates that a high accuracy of the threshold is necessary to detect those optical thin clouds. A smaller  $\delta$  (planetary albedo – surface albedo) is related to a

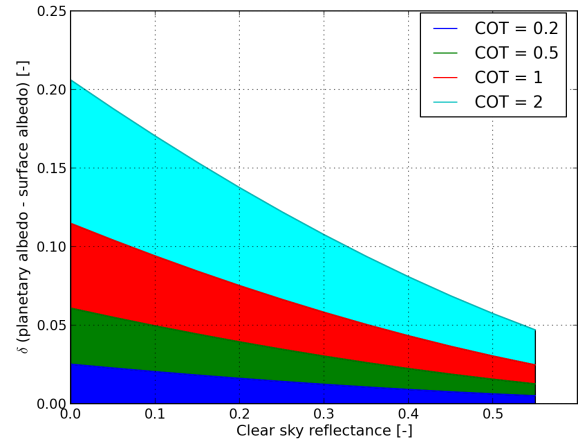


**Fig. 4.** Change in planetary albedo due to the occurrence of clouds with a COT of 0.2 (blue), 0.5 (green), 1 (red) and 2 (cyan) as a function of the clear-sky reflectance of the underlying surface. The  $\delta$  (y axis) demonstrates the accuracy that is necessary to detect a cloud over a surface with a specific clear-sky reflectance. This simple model is based on Eq. (1) by Lacis and Hansen (1974).

higher accuracy. This accuracy has to be even higher with an increasing clear-sky reflectance of the underlying surface (Fig. 4). For a higher COT the  $\delta$  (planetary albedo – surface albedo) is obviously higher, although substantially decreasing with a decreasing clear-sky reflectance.

Applying Eq. (2) to the average clear-sky reflectances (Table 2) for our four regions results in a minimum ascertainable COT of 0.88, 2.62, 2.62 and 2.95 over the Atlantic, the Alps, the Upper Rhine Valley and Spain during the summer period. This result demonstrates a negligence of thin cirrus clouds over land solely with the solar channel information. In summary, it can be stated that for a clear-sky reflectance higher than 0.25 it is very difficult to detect clouds above such bright surfaces. Over surfaces with about 0.35 clear-sky reflectances or even higher, no accurate cloud mask can be derived (Fig. 4). Equation (2), Fig. 4 and Table 2 indicate that no cloud with a COT above 1 can be detected reliably by the HRV cloud mask over the regions that are investigated in this study.

### 3.1 Cloud-free composites

To reduce the uncertainties caused by spatially varying surface reflectance, we apply the thresholds for cloud detection relative to a composite map of clear-sky HRV reflectance. These maps are derived initially based on the EUMETSAT cloud mask. Due to the lower SEVIRI standard resolution, it is necessary to upsample the EUMETSAT cloud mask to the 3 times higher resolution of the HRV channel. This is done using nearest-neighbor interpolation. The clear-sky composite is based on the median value  $\bar{\tau}_{cs}$  of all clear-sky

**Table 1.** Contingency table with binary classification cloudy and clear.

	EUMETSAT CLM cloudy	EUMETSAT CLM clear
Predicted HRV cloudy	true positive	false positive
Predicted HRV clear	false negative	true negative

reflectances observed during a 16-day period. The median is chosen as an alternative to the average value to neglect sub-pixel small-scale clouds, which are labeled as clear by the MPEF cloud mask. The average value would include biases such as small-scale undetected clouds or cloud shading. The length of this period seems appropriate to ensure relatively constant surface conditions and a high likelihood of finding at least one cloud-free observation for each pixel. Nevertheless, pixels can occur with no clear-sky observation due to persistent clouds. Such HRV pixels are always reported as cloudy.

Instead of subtracting the clear-sky composite from the observed reflectance, an anomaly map is created for each  $192 \times 192$  pixel region using Eq. (3):

$$r_{\text{norm}}(x, t) = r_{\text{obs}}(x, t) - (\langle \tilde{r}_{\text{cs}}(x) \rangle_t - \langle \tilde{r}_{\text{cs}} \rangle_{t,x}). \quad (3)$$

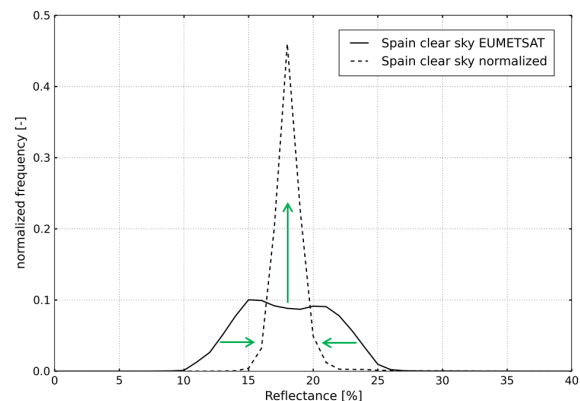
Here,  $r_{\text{obs}}(x, t)$  is the observed HRV reflectance field at time  $t$  during a specific period. The subtrahend  $\langle \tilde{r}_{\text{cs}}(x) \rangle_t - \langle \tilde{r}_{\text{cs}} \rangle_{t,x}$  consists of two parts. The first term  $\langle \tilde{r}_{\text{cs}}(x) \rangle_t$  is the spatially resolved temporal median of the clear-sky reflectance, while the second term  $\langle \tilde{r}_{\text{cs}} \rangle_{t,x}$  is the spatial and temporal median of the clear-sky reflectance.

Figure 5 demonstrates the effects of reducing the spatial variability by applying the clear-sky composite anomaly map. The solid line shows the histogram of the clear-sky HRV reflectance over Spain observed by MSG SEVIRI on 15 July 2011 and derived by applying the EUMETSAT cloud mask. The dotted line represents the normalized clear-sky histogram.

The effect of this treatment is illustrated by the green arrows in Fig. 5. The distribution indeed becomes more narrow, which indicates that our method is capable of compensating for the spatial variability of the underlying surface reflectance. This method therefore minimizes the overlap between the cloudy and clear histograms and reduces the associated uncertainty of the HRV cloud mask.

### 3.2 Optimal threshold

The threshold for detecting cloudy pixels should maximize the quality of our classification. It is thus necessary to compare it to reference data, and to define suitable quality criteria for assessing its accuracy. The four possible outcomes for comparing two binary classifications are listed in the contingency Table 1. In this study the EUMETSAT cloud mask is used as a reference, and the predicted class of the HRV

**Fig. 5.** Normalized frequency distribution of clear-sky HRV reflectances over Spain observed by MSG SEVIRI on 15 July 2011. The solid line is the distribution of clear-sky reflectances identified by the EUMETSAT cloud mask. The dotted line is the histogram of the normalized clear-sky reflectance after subtraction of the clear-sky composite anomaly map. The green arrows symbolize the reduction of spatial variability.

cloud mask depends on the selected reflectance threshold. Due to the use of prior information, this method corresponds to a supervised classification algorithm. For determining the optimal threshold, a suitable measure is sought that combines the frequencies of the four outcomes into one scalar quantity.

One measure that meets our requirements is the Matthews correlation coefficient (MCC, Matthews, 1975). Like the Pearson correlation coefficient for the continuous case, it quantifies the correlation between two binary variables in a range from  $-1$  to  $1$ , with  $1$  corresponding to perfect agreement.

The MCC is defined as follows:

$$\text{MCC} = \frac{\text{tp} \cdot \text{tn} - \text{fp} \cdot \text{fn}}{\sqrt{(\text{tp} + \text{fp}) \cdot (\text{tp} + \text{fn}) \cdot (\text{tn} + \text{fp}) \cdot (\text{tn} + \text{fn})}}. \quad (4)$$

It can be calculated directly from the contingency table from Eq. (4). One advantage of the MCC is its insensitivity to the frequency of both classes. This ensures that our cloud mask performs well in regions and seasons with low, medium and high frequency of clouds. The threshold that corresponds to the maximum of the MCC is chosen as optimal.

The flow chart in Fig. 6 visualizes the HRV cloud mask algorithm. The first step is the calculation of the clear-sky composite. This clear-sky composite consists of HRV reflectances, but the assignment between clear-sky and cloudy pixels is based on the MPEF cloud mask (see Sect. 3.1 for details). In the next iteration we consider the sub-pixel cloud coverage in the MPEF cloud mask to get a clear-sky composite that is based on detected clear-sky HRV pixels. The normalized HRV reflectance field improves with a higher accuracy of the clear-sky composite (Fig. 6, middle plot on the right panel). The variability of the cloudy histogram is



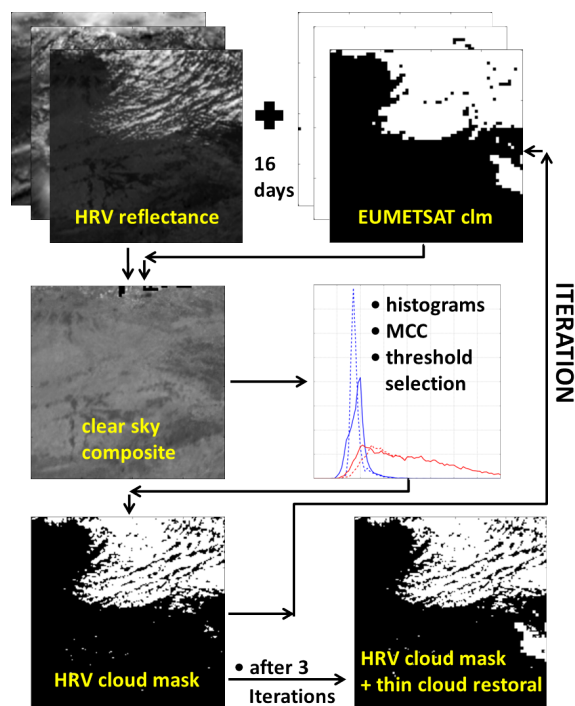


**Fig. 6.** Flow chart of our HRV cloud mask algorithm, based on the HRV reflectance and the EUMETSAT cloud mask as inputs. The clear-sky composite is initially calculated based on the HRV reflectance and the EUMETSAT cloud mask for 16-day periods. The panel showing the histograms represents the threshold selection step based on maximizing the MCC. As a final step, the thin cloud restoral to consider thin clouds is carried out. An iterative approach including the HRV cloud mask is chosen for the calculation of the clear-sky composite for consistency.

decreased as well, because thin cirrus clouds below the defined minimum COT are no longer considered by the HRV cloud mask (Fig. 6).

The calculation of the quality criteria is based on the MPEF cloud mask and the normalized HRV reflectance field. The corresponding reflectance of the maximum of the MCC is defined as the relative threshold  $t_{\text{rel}}$ ;  $t_{\text{rel}}$  of each iteration is then applied to the reflectance field and results in a higher accuracy of the HRV cloud detection algorithm. The MPEF cloud mask is the constant reference mask for this calculation. The resulting HRV cloud mask of this algorithm is used as new input for the whole procedure. The iteration algorithm will stop if the deviation of the relative threshold between two iterations is below 0.001.

A final processing step is introduced to consider thin clouds with a *thin cloud restoral*. The detection of thin cirrus clouds solely based on the broadband information from the HRV channel is difficult. As it is our aim to determine a HRV cloud mask that is complementary to and consistent

with the MPEF cloud mask, we redefine  $3 \times 3$  clear-sky HRV pixel blocks as cloudy if the appropriate pixel of the MPEF cloud mask detects clouds. These redefined HRV pixels are flagged in a different way than cloudy pixels that are introduced as cloudy from the HRV cloud detection algorithm (Fig. 6). This is mainly done due to the fact that this gives the user of the cloud mask the choice of what cloud type will be investigated depending on the application (e.g., clear-sky composites). The thin cloud restoral has no impact on small-scale clouds, which are undetected by the MPEF cloud mask. Our future plan is to use the cloud type description of the Support to Nowcasting and Very Short Range Forecasting (NWCSAF) for the investigation of thin cirrus clouds (see Sect. 5 for details).

#### 4 Results and discussion

In order to assess the quality of the HRV cloud mask, some aspects related to its accuracy are investigated and discussed in this section. The EUMETSAT cloud mask is used as a reference to support the consistency of both cloud masks, and due to the lack of other suitable reference data. For this analysis, the four regions shown in Fig. 2 are used as typical examples for different surface types.

To compare our results with the EUMETSAT cloud mask, the latter mask has been upscaled to HRV resolution.

First, the cloud detection frequency for pixels in the EUMETSAT cloud mask has been determined as a function of the number of cloudy pixels identified by the HRV cloud mask algorithm in the corresponding  $3 \times 3$  HRV pixel blocks. Results have been aggregated for each region over the time period from 1 July until 16 August 2011. The result of this comparison is plotted in Fig. 7. For completely cloudy HRV pixel blocks, we find 100 % agreement with the corresponding EUMETSAT cloud mask classification. In contrast, 10 % of all completely clear HRV pixel blocks are actually identified as cloudy by the EUMETSAT cloud mask. Closer inspection of several corresponding scenes revealed that this deviation is mainly caused by optically thin cirrus clouds, which are not detected by the HRV channel due to their low reflectance. These cases are addressed by the thin cloud restoral and motivated its inclusion in the algorithm. Although the thin cloud restoral works well in general, some artifacts can occur under specific circumstances as described below.

One particular case over the Upper Rhine Valley has been chosen to illustrate the complementary information of the MPEF and the HRV cloud mask (Fig. 8). This case example demonstrates very well how both cloud masks gain different information about the cloud types. Misclassified cloud pixels by the HRV cloud mask against detected cloud pixels by the MPEF cloud mask can be explained by optical thin clouds with a COT underneath a critical threshold (Fig. 8, red pixels). Areas that are contaminated with small-scale shallow

**Table 2.** Results of the HRV cloud mask algorithm averaged over three 16-day periods starting 1 June, 1 July and 1 August 2011. The four regions considered are listed in column 1.  $\overline{Cc}$  is the average cloud cover, and  $\overline{r_{cs}}$  is the spatially averaged temporal median HRV clear-sky reflectance including its standard deviation  $\text{std}(r_{cs})$ . Columns 4 and 5 report the cloud detection thresholds above which a pixel is classified as cloudy.  $t_{\text{abs}}$  lists the absolute threshold without use of the HRV clear-sky reflectance composite, while  $t_{\text{rel}}$  is the threshold relative to the composite. The percentage deviations between the HRV and the EUMETSAT cloud mask are given in columns 6–8. Here,  $\text{Dev}_{\text{abs}}$  and  $\text{Dev}_{\text{rel}}$  are the deviations found using  $t_{\text{abs}}$  and  $t_{\text{rel}}$ , respectively. Column 8 lists the final deviation  $\text{Dev}_{\text{fi}}$  after applying the HRV clear-sky composite and thin cloud restoral.

Regions	$\overline{Cc}$ [%]	$\overline{r_{cs}} \pm \text{std}(r_{cs})$ [–]	$t_{\text{abs}}$ [–]	$t_{\text{rel}}$ [–]	$\text{Dev}_{\text{abs}}$	$\text{Dev}_{\text{rel}}$	$\text{Dev}_{\text{fi}}$
Atlantic	85	$0.068 \pm 0.007$	+0.042	+0.029	7.1	6.1	2.9
The Alps	75	$0.187 \pm 0.022$	+0.080	+0.051	13.6	10.1	8.4
Upper Rhine Val.	79	$0.191 \pm 0.017$	+0.067	+0.048	10.7	8.8	6.5
Spain	40	$0.193 \pm 0.03$	+0.085	+0.044	12.4	10.3	5.3

convection with an optical thickness above our threshold cannot be detected by the MPEF cloud mask (Fig. 8, blue pixels).

The HRV reflectance misses a high amount of cloudy pixels corresponding to thin cirrus clouds. This example demonstrates that the capabilities of the HRV channel for detecting thin cirrus clouds are limited. When considering the brightness temperature difference BT  $10.8\mu\text{m}$ –BT  $3.9\mu\text{m}$ , the thin cirrus clouds can clearly be recognized in the northwestern corner of the region. Usually the brightness temperature difference BT  $10.8\mu\text{m}$ –BT  $12.0\mu\text{m}$  is applied over all surfaces to detect thin cirrus clouds (Derrien et al., 2010b). To give a better feeling of our statement about Fig. 8c, we use the brightness temperature difference BT  $10.8\mu\text{m}$ –BT  $3.9\mu\text{m}$  for that, because it shows a better occurrence of thin cirrus clouds in the northwestern corner in our case example (Frey et al., 2008).

The thin cloud restoral redefines a  $3 \times 3$  pixel block only as cloudy if the entire block is detected as clear by the threshold algorithm. This approach is problematic for situations where small-scale low-level clouds occur underneath a larger cirrus cloud. This effect is visible in Fig. 8. The EUMETSAT cloud mask and the brightness temperature difference BT  $10.8\mu\text{m}$ –BT  $3.9\mu\text{m}$  indicate a larger cloud coverage due to cirrus. Some brighter pixels appear in the northern HRV image section, which are likely caused by small convective clouds. In the vicinity of these clouds, unrealistic gaps in cloud coverage occur.

The most valuable benefit of the HRV cloud mask is the high proportion of small-scale cumulus clouds that are likely missed by the MPEF cloud mask. This effect is indicated by the blue areas in Fig. 8d. Concerning the frequency of cloudy HRV pixels that are assigned as clear by the MPEF cloud mask, we found an amount of 10 % over the Upper Rhine Valley. This frequency demonstrates the number of small-scale cumulus clouds missed by the MPEF cloud mask (false positive) divided by the number of all clouds (true positive + false positive).

The HRV channel is not used by the EUMETSAT cloud detection algorithm. To demonstrate that its broad spectral response is still suitable for an accurate threshold-based

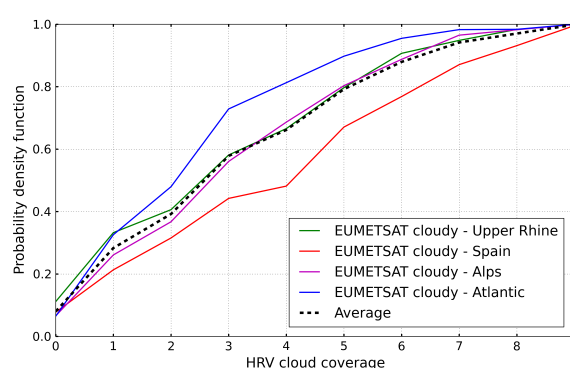
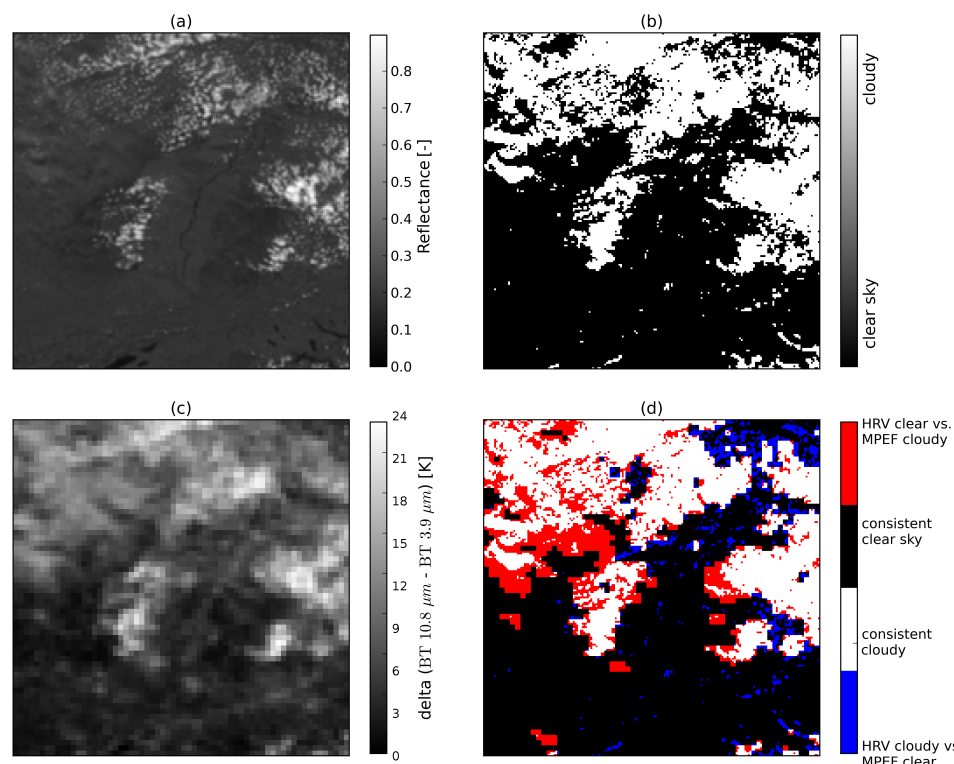


**Fig. 7.** Cloud detection frequency of the EUMETSAT cloud mask versus the number of cloudy HRV pixels detected by the HRV cloud mask for a corresponding  $3 \times 3$  HRV pixel block. The solid colored lines mark the average obtained for all HRV pixel blocks for the four regions between 1 June 2011 and 16 August 2011. The average over all regions is indicated by the dotted line.

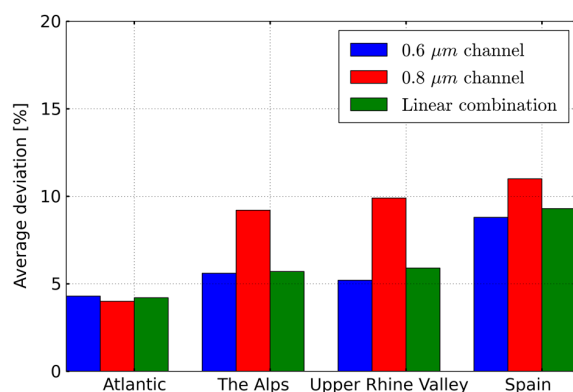
cloud detection, we have compared the results of our algorithm applied to the HRV channel to those obtained with the narrowband channels at  $0.6$  and  $0.8\mu\text{m}$  wavelength and at LRES spatial resolution (Fig. 9). For this purpose, the HRV channel is simulated as a linear combination of the  $0.6$  and  $0.8\mu\text{m}$  reflectances as proposed by Cros et al. (2006) and using the regression coefficients reported by Deneke and Roebeling (2010). The accuracy of the cloud mask applied to the simulated HRV channel lies between those achieved with the  $0.6$  and  $0.8\mu\text{m}$  channels. Over ocean, differences are small, and the best accuracy is found for the  $0.8\mu\text{m}$  channel, as it is slightly darker than the other channels. Over land, best results are obtained with the  $0.6\mu\text{m}$  channel, but the accuracy of the simulated HRV signal is only slightly lower. Over vegetated surfaces, the  $0.8\mu\text{m}$  exhibits a significantly lower skill, while the relatively bright surface over Spain causes an overall degradation of detection accuracy.

Table 2 summarizes the results of our threshold algorithm and lists the final deviations versus the EUMETSAT cloud





**Fig. 8.** (a) SEVIRI HRV reflectance over the Upper Rhine Valley on 5 July 2011, 12:00 UTC and (b) HRV cloud mask (white: cloudy, black: clear-sky). (c) Corresponding brightness temperature difference  $BT\ 10.8\ \mu m - BT\ 3.9\ \mu m$  and (d) difference between MPEF and HRV cloud mask (white: cloudy, black: clear-sky, red: HRV clear-sky versus MPEF cloudy and blue: HRV cloudy versus MPEF clear-sky).



**Fig. 9.** Average deviation of the EUMETSAT cloud mask and our threshold-based cloud mask algorithm at low resolution and applied to the 0.6 and 0.8  $\mu m$  channels and a linear combination of both channels to simulate the HRV signal (see text for details). Results have been calculated for three periods of 16 days starting on 1 June, 1 July and 1 August 2011.

mask. Based on the EUMETSAT cloud mask, all regions but Spain have a high average cloud cover ranging from 75 to 85 %. The Atlantic (1) is a region with frequent passages of frontal systems. The Alps (2) and Upper Rhine Valley (3) are characterized by orographically induced convection. One should recognize that the 12:00 UTC time slot is used for this study, which implies a high level of solar irradiance and thus a well-mixed convective boundary layer (Driedonks, 1982). In contrast, the cloud coverage over northern Spain is relatively low. The large observed differences in average cloud cover for the four regions illustrate the importance of choosing a threshold selection scheme that is insensitive to the relative occurrence frequencies of both classes (see Sect. 3.2).

The high standard deviation of the clear-sky reflectance over the Alps and Spain underlines the high spatial variability of the surface over these regions. This finding correlates with a strong reduction of the thresholds  $t_{abs}$  and  $t_{rel}$ . Here,  $t_{abs}$  is the absolute threshold determined without using the clear-sky composite information, while  $t_{rel}$  is the threshold relative to the clear-sky composite. Both the lower threshold  $t_{rel}$  compared to  $t_{abs}$ , and the resulting lower deviation ( $Dev_{rel}$ ) compared to  $Dev_{abs}$  confirm that our choice of using a clear-sky composite improves the separability of clear

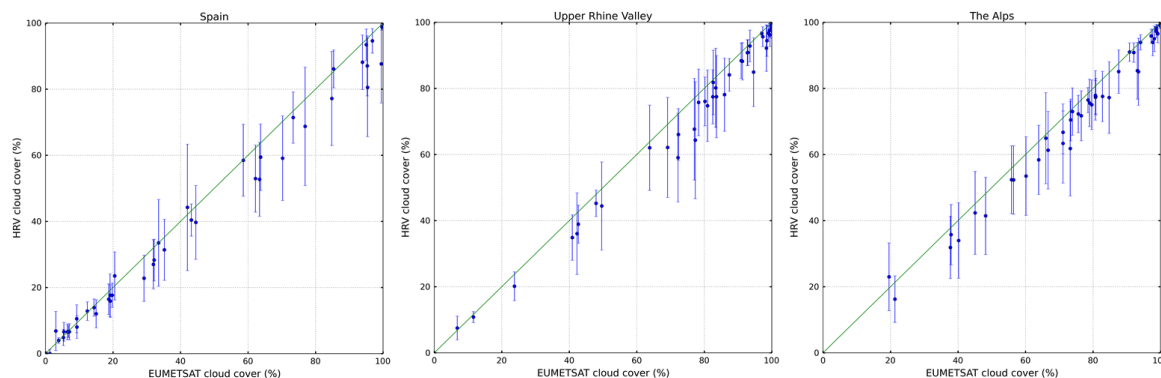


**Fig. 10.** Comparison of the cloud coverage of the EUMETSAT and HRV cloud masks after thin cloud restoral. The blue dots show the cloud coverage, and the error bars illustrate the fraction of deviating HRV pixel classifications, obtained for each time slot and given in percent. Results have been obtained for three periods of 16 days (starting 1 June, 1 July and 1 August 2011).

and cloudy radiances, and thus results in an overall improved classification accuracy.

Even though the clear-sky variability over the Atlantic region is very low with a standard deviation of only 0.007, there is still a significant spread of 0.013 between  $t_{\text{abs}}$  and  $t_{\text{rel}}$ . This effect is caused by the initial clear-sky composite, which includes some brighter pixels corresponding to small clouds missed by the EUMETSAT cloud mask. By applying our iteration scheme, these bright pixels are filtered out, as is reflected by a reduced standard deviation of the clear-sky reflectance.

$\text{Dev}_{\text{fi}}$  is the final deviation after applying the thin cloud restoral. The difference between  $\text{Dev}_{\text{fi}}$  and  $\text{Dev}_{\text{rel}}$  is lowest over the Alps (1.7 %) and the Upper Rhine Valley (2.3 %). This is probably due to the high amount of clouds in general, and convective clouds in particular over these regions, which limit the applicability of the thin cloud restoral. On the other hand, a strong impact of the thin cloud restoral on the deviation of the final HRV cloud mask is found for the Atlantic and Spain. Sample scenes such as Fig. 8 indicate a relatively high amount of thin clouds over these regions.

To identify the overall effect of including the HRV channel for cloud masking, Fig. 10 compares the cloud coverages obtained from the EUMETSAT and HRV cloud masks for the three land regions. In the majority of cases, the average HRV cloud coverage lies below the cloud coverage of the EUMETSAT cloud mask. This systematic difference is composed of two effects: first, thin cirrus clouds that are missed by the HRV cloud mask but at least partly corrected for by the thin cloud restoral; second, SEVIRI LRES pixels that are counted as completely cloud-filled by the EUMETSAT cloud mask, but are identified as broken by the HRV cloud mask. While it is impossible to separate both effects without independent reference data, the latter seems to dominate.

The blue error bars indicate the fraction of deviating classifications between both cloud masks found for each time slot.

Generally, the fraction rises with increasing cloud amount, until it reaches a value of about 80 % where it starts to fall again. Thus, partly cloudy conditions cause the highest deviations. This result is expected, because the HRV cloud mask can gain additional information about partly cloud-filled pixels and cloud edges compared due to its higher spatial resolution.

## 5 Summary and conclusions

In this study we have presented and evaluated a threshold-based HRV cloud mask that is based on the EUMETSAT cloud mask and extends it to a 3-fold higher spatial resolution while maintaining consistency with its results. The optimal threshold to differentiate between clear-sky and cloudy radiances is chosen by maximizing the Matthews correlation coefficient (MCC), a quality measure for binary classifications that is not influenced by the ratio of cloudy to clear pixels, to ensure the best agreement of our cloud mask with the EUMETSAT cloud mask. Clear-sky anomaly maps are used to account for regions with high variability in surface reflectance. As a result, the overlap in the clear and cloudy histograms, and thus the uncertainty in the classification, is significantly reduced. An iterative approach is chosen to include the HRV cloud mask information in the calculation of the clear-sky anomaly maps, with convergence generally achieved after two iterations.

A thin cloud restoral is done to account, for example, for thin cirrus clouds that are not detected by the high-resolution visible channel, in order to ensure that the HRV cloud mask results are consistent with the EUMETSAT cloud mask. Completely clear  $3 \times 3$  HRV pixel blocks are redefined as cloudy if the corresponding LRES pixel is reported as cloudy in the EUMETSAT cloud mask. Some remaining artifacts after this cloud restoral are found, which are explained and illustrated in Fig. 8. These redefined pixel blocks are flagged

in a different way than the cloudy pixels that are introduced by the HRV cloud mask. The thin cloud restoral causes some biases, which have been mentioned already. Our future plan is to use the NWCSAF cloud type description to improve the detection of thin cirrus clouds in the HRV cloud mask (Dybbroe et al., 2005). The HRV cloud mask aims to resolve sub-pixel small-scale clouds that are missed by the MPEF cloud mask. In our example, we found an amount of 10 % of these small-scale cumulus clouds over the Upper Rhine Valley. This study shows that the HRV channel offers important sub-pixel information for the remaining low-resolution channels.

On average, 10 % of all  $3 \times 3$  clear-sky HRV pixel blocks are missed by our threshold test and restored to cloudy pixels, which occurs mainly for thin cirrus clouds. Our results indicate that the HRV cloud mask performs very reliably in cloudy conditions. The frequency of cloudy LRES pixels that are found to be broken in our data set is 16 %. The highest frequency with 24.3 % occurs over the Alps and the lowest fraction over the Atlantic (4.6 %). The amount of broken pixels reaches 15.5 % over Spain and 19.4 % over the Upper Rhine Valley. The high values over the Upper Rhine Valley and the Alps are expected and underline the frequent occurrence of small-scale convective cumuli clouds over these regions. Deviations between the EUMETSAT cloud mask and the HRV cloud mask after thin cloud restoral occur for 5.8 % of the HRV pixels. This deviation results from an overestimate of the cloud fraction due to partially cloudy HRV pixel blocks, which are reported as completely cloudy by the EUMETSAT cloud mask.

This HRV-based cloud mask is part of our wider effort to extend the cloud physical properties retrieval (Roebeling et al., 2006; Roebeling et al., 2008) to the high spatial resolution of the HRV channel, including an estimate of cloud optical thickness (Carbajal Henken et al., 2011) and other cloud properties. It offers also the possibility of applying the cloud mask as a tool to study the geometric size of convective clouds including their temporal evolution in the future. Similar approaches will be essential to utilize the data from future satellite missions optimally, such as Meteosat Third Generation, whose imager has different spatial resolutions for the solar and infrared channels. For a disk-wide application of the HRV cloud mask, more regions with a higher amount of cirrus clouds or high aerosol loads should be considered.

To validate the HRV cloud mask, we have used the MPEF cloud mask as a reference and pointed out the consistency between both masks, but they have different limitations. The cloud retrieval evaluation workshop (CREW) introduces some studies that will be used as independent validation data for the HRV cloud mask in further research (Roebeling et al., 2012). However, more validation has to be done to quantify the accuracy of the HRV cloud mask and the improvements of using the HRV channel for cloud detection schemes. Ideally, the comparison should include MODIS and CloudSat

data as has already been done with the MPEF cloud mask (Ricciardelli et al., 2008).

**Acknowledgements.** The authors thank A. Macke and A. Hünerbein of the Leibniz Institute for Tropospheric Research (TROPOS), who provided many helpful comments and suggestions on previous versions of this paper. The Meteosat-9 data used in this study were provided by EUMETSAT. We thank the two anonymous reviewers for improving this paper.

Edited by: A. Kokhanovsky

## References

- Carbajal Henken, C., Schmeits, M. J., Deneke, H. M., and Roebeling, R. A.: Using MSG-SEVIRI cloud physical properties and weather radar observations for the detection of Cb/TCu clouds, *J. Appl. Meteorol. Clim.*, 50, 1587–1600, 2011.
- Cros, S., Albuissou, M., and Wald, L.: Simulating Meteosat-7 broadband radiances using two visible channels of Meteosat-8, *Sol. Energy*, 80, 361–367, 2006.
- Deneke, H. M. and Roebeling, R. A.: Downscaling of METEOSAT SEVIRI 0.6 and 0.8  $\mu\text{m}$  channel radiances utilizing the high-resolution visible channel, *Atmos. Chem. Phys.*, 10, 9761–9772, doi:10.5194/acp-10-9761-2010, 2010.
- Derrien, M., Gléau, H. L., and Raoul, M.-P.: The use of the high resolution visible in SAFNWC/MSG cloud mask, in: *Proceedings of the 2010 EUMETSAT Meteorological Satellite Conference*, 20–24 September 2010, Córdoba, Spain, 57 pp., 2010a.
- Derrien, M., Gléau, H. L., and Fernandez, P.: Algorithm theoretical basis document for Cloud products (CMAPGE01 v3.0, CT-PGE02 v2.0 & CTTH-PGE03 v2.1), [ftp://ftp.eumetsat.int/pub/MET/out/watts/SAFMeteoF/SAF-NWC-CDOP-MFL-SCI-ATBD-01\\_v3.1d.pdf](ftp://ftp.eumetsat.int/pub/MET/out/watts/SAFMeteoF/SAF-NWC-CDOP-MFL-SCI-ATBD-01_v3.1d.pdf) (last access: 5 June 2013), 2010b.
- Driedonks, A. G. M.: Sensitivity analysis of the equations for a convective mixed layer, *Bound.-Lay. Meteorol.*, 22, 475–480, 1982.
- Dybbroe, A., Karlsson, K. G., and Thoss, A.: NWCSAF AVHRR cloud detection and analysis using dynamic thresholds and radiative transfer modeling, Part I: Algorithm description, *J. Appl. Meteorol.*, 44, 39–54, 2005.
- EUMETSAT: Cloud Detection for MSG – Algorithm Theoretical Basis Document, [http://www.eumetsat.int/groups/ops/documents/document/PDF\\_MET\\_ATBD\\_CLOUD\\_DETECTIO-N.pdf](http://www.eumetsat.int/groups/ops/documents/document/PDF_MET_ATBD_CLOUD_DETECTIO-N.pdf) (last access: 14 August 2012), 2007.
- Forster, P., Ramaswamy, V., Artaxo, P., Bernsten, T., Betts, R., Fahey, D. W., Haywood, J., Lean, J., Lowe, D. C., Myhre, G., Nganga, J., Prinn, R., Raga, G., Schulz, M. and Van Dorland, R.: Changes in Atmospheric Constituents and in Radiative Forcing, in: *Climate Change 2007: The Physical Science Basis, Contribution of Working Group I to the Fourth Assessment Report of the Intergovernmental Panel on Climate Change*, edited by: Solomon, S., Qin, D., Manning, M., Chen, Z., Marquis, M., Averyt, K. B., Tignor, M. and Miller, H. L., Cambridge University Press, Cambridge, UK and New York, NY, USA, 129–234, 2007.

- Frey, R., Ackerman, S. A., Liu, Y., Strabala, K. I., Zhang, H., Key, J., and Wang, X.: Cloud detection with MODIS: Part I. Improvements in the MODIS Cloud Mask for Collection 5, *J. Atmos. Ocean. Tech.*, 25, 1057–1072, 2008.
- Ipe, A., Clerbaux, N., Bertrand, C., Dewitte, S., and Gonzalez, L.: Pixel-scale composite top-of-the-atmosphere clear-sky reflectances for Meteosat-7 visible data, *J. Geophys. Res.*, 108, 4612, doi:10.1029/2002JD002771, 2003.
- Klüser, L., Rosenfeld, D., Macke, A., and Holzer-Popp, T.: Observations of shallow convective clouds generated by solar heating of dark smoke plumes, *Atmos. Chem. Phys.*, 8, 2833–2840, doi:10.5194/acp-8-2833-2008, 2008.
- Lacis, A. A. and Hansen, J. E.: A parameterization for the absorption of solar radiation in the Earth's atmosphere, *J. Atmos. Sci.*, 31, 118–133, 1974.
- Lensky, I. M. and Rosenfeld, D.: Clouds-Aerosols-Precipitation Satellite Analysis Tool (CAPSAT), *Atmos. Chem. Phys.*, 8, 6739–6753, doi:10.5194/acp-8-6739-2008, 2008.
- Liou, K. N.: An Introduction to Atmospheric Radiation, in: *International Geophysics Series 25*, Academic Press, 392 pp., 1980.
- Matthews, B. W.: Comparison of the predicted and observed secondary structure of T4 phage lysozyme, *Biochim. Biophys. Acta*, 405, 442–451, 1975.
- Minnis, P. and Harrison, E. F.: Diurnal variability of regional cloud and clear-sky radiative parameters derived from goes data, Part iii: November 1978 radiative parameters, *J. Clim. Appl. Meteorol.*, 23, 993–1011, 1984.
- Ricciardelli, E., Romano, F., and Cuomo, V.: Physical, statistical and temporal analysis approaches for cloud identification using MSG-SEVIRI data, in: *Proceedings of the 2008 EUMETSAT Meteorological Satellite Conference*, 8–12 September 2008, Darmstadt, Germany, 2008.
- Roebeling, R. A. and van Meijgaard, E.: Evaluation of the daylight cycle of model predicted cloud amount and condensed water path over Europe with observations from MSG-SEVIRI, *J. Climate*, 22, 1749–1766, 2009.
- Roebeling, R. A., Feijt, A. J., and Stammes, P.: Cloud property retrievals for climate monitoring: implications of differences between SEVIRI on METEOSAT-8 and AVHRR on NOAA-17, *J. Geophys. Res.*, 111, 206–222, 2006.
- Roebeling, R. A., Deneke, H., and Feijt, A. J.: Validation of cloud liquid water path retrievals from SEVIRI using one year of CloudNET observations, *J. Appl. Meteorol. Clim.*, 47, 206–222, 2008.
- Roebeling, R., Baum, B., Bennartz, R., Hamann, U., Heidinger, A., Thoss, A., and Walther, A.: Outcome of the third cloud retrieval evaluation workshop, in: *Proceedings of the 2012 Radiation Processes in the Atmosphere and Ocean (IRS2012)*, 6–10 August 2012, Berlin, Germany, 416–419, doi:10.1063/1.4804795, 2012.
- Rossow, W. B., Garder, L. C., and Lacis, A. A.: Global, seasonal cloud variations from satellite radiance measurements, Part I: Sensitivity of analysis, *J. Climate*, 2, 419–458, 1989.
- Saunders, R. W. and Kriebel, K. T.: An improved method for detecting clear sky radiances from AVHRR data, *Int. J. Remote Sens.*, 9, 123–150, 1988.
- Schmetz, J. P., Pili, P., Tjemkes, S., Just, D., Kerkmann, J., Rota, S., and Ratier, A.: An introduction to Meteosat Second Generation (MSG), *B. Am. Meteorol. Soc.*, 83, 977–992, 2002.
- Yang, Y., Girolamo, L., and Mazzoni, D.: Selection of the automated thresholding algorithm for the Multi-angle Imaging SpectroRadiometer Radiometric Camera by – Camera Cloud Mask over land, *Remote Sens. Environ.*, 107, 159–171, 2007.

## **4.2 Second publication: Meteosat-based characterization of the spatiotemporal evolution of warm convective cloud fields over Central Europe**

The content of this chapter has already been published in the manuscript “Meteosat-Based Characterization of the Spatiotemporal Evolution of Warm Convective Cloud Fields over Central Europe” by Sebastian Bley, Hartwig Deneke and Fabian Senf in the journal “Journal of Applied Meteorology and Climatology” in 2016 with the doi: 10.1175/JAMC-D-15-0335.1.

Reprinted with permission by the authors from Journal of Applied Meteorology and Climatology. 2016, 55, 2181–2195. Copyright 2016 by American Meteorological Society.

## **Meteosat-Based Characterization of the Spatiotemporal Evolution of Warm Convective Cloud Fields over Central Europe**

SEBASTIAN BLEY, HARTWIG DENEKE, AND FABIAN SENF

*Leibniz Institute for Tropospheric Research, Leipzig, Germany*

(Manuscript received 13 November 2015, in final form 14 June 2016)

### ABSTRACT

The spatiotemporal evolution of warm convective cloud fields over central Europe is investigated on the basis of 30 cases using observations from the Spinning Enhanced Visible and Infrared Imager (SEVIRI) on board the geostationary Meteosat platforms. Cloud fields are tracked in successive satellite images using cloud motion vectors. The time-lagged autocorrelation is calculated for spectral reflectance and cloud property fields using boxes of  $16 \times 16$  pixels and adopting both Lagrangian and Eulerian perspectives. The  $0.6\text{-}\mu\text{m}$  reflectance, cloud optical depth, and water path show a similar characteristic Lagrangian decorrelation time of about 30 min. In contrast, significantly lower decorrelation times are observed for the cloud effective radius and droplet density. It is shown that the Eulerian decorrelation time can be decomposed into an advective component and a convective component using the spatial autocorrelation function. In an Eulerian frame cloud fields generally decorrelate faster than in a Lagrangian one. The Eulerian decorrelation time contains contributions from the spatial decorrelation of the cloud field advected by the horizontal wind. A typical spatial decorrelation length of 7 km is observed, which suggests that sampling of SEVIRI observations is better in the temporal domain than in the spatial domain when investigating small-scale convective clouds. An along-track time series of box-averaged cloud liquid water path is derived and compared with the time series that would be measured at a fixed location. Supported by previous results, it is argued that this makes it possible to discriminate between local changes such as condensation and evaporation on the one hand and advective changes on the other hand.


## 1. Introduction

Warm convective clouds are highly variable in space and time and cover large areas of Earth (Turner et al. 2007). Through the transport of energy and moisture, they couple the boundary layer and the free troposphere. Their bright cloud tops reflect the incoming sunlight, which strongly modulates the atmospheric radiation budget (Trenberth et al. 2009). Because of our lack of understanding of relevant processes and feedbacks, low-level

clouds remain a dominant source of uncertainty in climate projections (Clement et al. 2009).

The central motivation of this study is to find suitable techniques and quantities that allow a spatiotemporal characterization of convective cloud fields and their life cycle from space, and can subsequently serve, for example, as metrics for evaluating parameterizations of cumulus convection in climate models (Dorrestijn et al. 2013). This characterization provides complementary information about the spatial structure and temporal changes of cloud properties to serve as a fingerprint of underlying dynamical and microphysical processes. In addition, information on the spatial structure of cloud fields as given by the power spectrum are essential to realistically represent cloud radiative effects in models and observations (Davis et al. 1996).

In an early global study based on satellite observations, the frequency of fractional cloudiness on scales smaller than  $50\text{--}200\text{ km}^2$  was found to be 20%–30% (Rossow and Garder 1993). Albrecht (1989) already pointed out the high uncertainties of the global albedo in climate models due to the crude representation of

 Denotes Open Access content.

 Supplemental information related to this paper is available at the Journals Online website: <http://dx.doi.org/10.1175/JAMC-D-15-0335.s1>.

*Corresponding author address:* Sebastian Bley, Remote Sensing of Atmospheric Processes, Leibniz Institute for Tropospheric Research, Permoserstr. 15, Leipzig, Germany.  
E-mail: [bley@tropos.de](mailto:bley@tropos.de)

DOI: 10.1175/JAMC-D-15-0335.1

© 2016 American Meteorological Society

cumulus cloud coverage, which still affect current models. It has been suggested that intercomparisons of observations, large-eddy simulations (LES), and single-column models (SCM) are essential for improving such parameterizations (Lenderink et al. 2004). Brown et al. (2002) designed a LES model of shallow cumulus convection over land as basis for testing cloud parameterizations in numerical weather prediction and climate models. High-resolution models, however, also have problems in representing clouds realistically, as can be determined by comparisons with observations. In recent years the spatiotemporal resolution of models has been steadily increased to better resolve relevant small-scale cloud processes. One promising source of observations for the evaluation of high-resolution models is meteorological satellites because of their global coverage. In contrast to polar-orbiting satellites, geostationary satellites like Meteosat have the capability to observe and track cumulus clouds from their early developing stage onward and are the focus of the present study.

Separating cloudy from cloud-free areas is an essential first step in the retrieval of cloud physical properties from satellite. Roebeling et al. (2006) developed an algorithm to retrieve the cloud optical thickness ( $\tau$ ), the cloud droplet effective radius ( $r_e$ ), and the liquid water path (LWP) from solar channels during daytime. However, the investigation of warm convective cloud fields based on these retrieved properties is challenging because of low LWP values and small clouds sizes. Fractional cloudiness induces small-scale optical property variations and thus high uncertainties (Han et al. 1994). This can be explained by small clouds and cloud-free areas that are smaller than the actual satellite resolution (Koren et al. 2008). In particular the retrieval of  $r_e$  is very sensitive to the spatial satellite resolution. Wolters et al. (2010) identified that  $r_e$  is highly overestimated at lower satellite resolutions because of variability and the nonlinear relation between the absorbing reflectances and  $r_e$ . These uncertainties also propagate to estimates of the LWP, which is generally assumed to be proportional to the product of  $\tau$  and  $r_e$  (Horvath et al. 2014).

These cloud property uncertainties demonstrate that validation of cloud property retrievals with ground-based or other satellite measurements is required (Roebeling et al. 2008). However, comparing convective cloud properties obtained from satellite with instantaneous ground-based measurements is challenging because of their rapid changes in space and time (Feijt and Jonker 2000; Deneke et al. 2009). Despite these uncertainties, Meteosat observations are the best available option to characterize the spatiotemporal evolution of cloud fields over Europe, and thus offer unique reference data for model evaluation. Up to now, however,

this potential has not been fully exploited, also because of the lack of established techniques and quantities for such an evaluation.

In prior studies, Cahalan et al. (1982) performed a spatiotemporal statistical analysis of day-to-day changes in cloudiness using data from the scanning radiometer aboard the polar-orbiting National Oceanic and Atmospheric Administration satellites. They calculated characteristic time and length scales from decorrelation functions of time- and space-lagged infrared (IR) images and showed that Lagrangian correlation times are always larger than the Eulerian. They, however, focused on relatively large spatial and temporal scales on the order of several hundred kilometers and several days, respectively. For the characterization of statistical cloud properties on a kilometer scale, Slobodda et al. (2015) investigated decorrelation lengths for different measurements in the solar and IR part of the spectrum over Europe and using Meteosat observations. They stated that visible and near-IR observations, which are basis for cloud property retrievals, decorrelate much faster than IR fields, which are related to cloud-top temperature and obtain their signals from higher atmospheric layers. Feijt and Jonker (2000) showed that temporal scales of variability in LWP derived from ground-based microwave measurements can be matched to spatial scales in satellite-retrieved fields of LWP.

A spatiotemporal characterization of convective cloud fields does potentially have, however, a wide applicability, ranging from forecasts of solar irradiance in the context of solar power generation (Hammer et al. 1999) to the detection of convective initiation (Senf et al. 2015). Toward this, the Eulerian perspective and the Lagrangian perspective will be contrasted. While the former is typical for ground-based measurements, we argue that the latter is better suited for a process-based characterization of clouds, as it allows a separation of advective and convective changes. Taking these findings into account has high implications for observation networks. We also aim for the identification of quantities that are suitable for model comparison. We therefore consider not only Meteosat reflectances but also optical and microphysical cloud properties and high-resolution wind data. Here, the temporal changes of satellite-derived LWP fields receive particular attention in our correlation analysis because LWP is readily available from models, and changes can be attributed to physical processes affecting condensation and evaporation of cloud droplets. Please note that precipitation and glaciation processes also influence the evolution of LWP fields; however, they are not considered in our study.



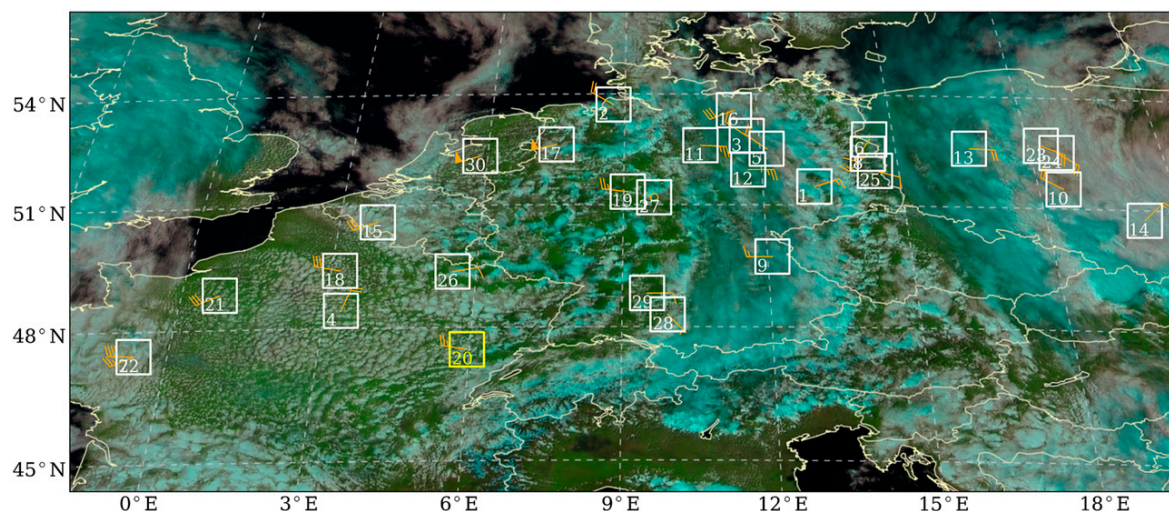


FIG. 1. Overview map of the selected cases. The underlying RGB image (Lensky and Rosenfeld 2008) is a composite of the 0.6-, 0.8-, and 1.6- $\mu\text{m}$  channels and the HRV channel from MSG SEVIRI showing the cloud scene of case 20 at 1200 UTC 17 May 2012. The white rectangles indicate the track starting area along with the number of the trajectory. The orange barbs illustrate the cloud motion vectors for the respective case. Note that the cloud scenery is different for each of the cases except case 20.

Section 2 provides an overview of the data, and section 3 describes our main methodology for the study. In section 4, we present the results and discuss how they relate to similar past studies. Section 5 summarizes conclusions and gives suggestions for future studies.

## 2. Data

Data from the Spinning Enhanced Visible and Infrared Imager (SEVIRI) are used in this analysis. This optical imaging radiometer is the main payload on board the geostationary Meteosat Second Generation (MSG) satellites, which are operated by EUMETSAT. In addition to 11 narrowband channels (solar and IR) with a nadir spatial resolution of  $3 \times 3 \text{ km}^2$ , one broadband high-resolution visible (HRV) channel ( $1 \times 1 \text{ km}^2$  in nadir) is applied. A detailed technical description of MSG is given by Schmetz et al. (2002).

For this paper, 30 cases from the years 2012 and 2013 have been selected from Meteosat's rapid-scan service (RSS) covering Europe with a 5-min repeat cycle from a satellite position at  $9.5^\circ\text{E}$  above the equator. The cases show low-level broken cumulus clouds in different meteorological environments. Detailed information about the meteorological conditions can be found in section 4a. *Meteosat-8* provided this service until 9 April 2013, when it was replaced by *Meteosat-9*. Our domain of interest covers Germany and parts of eastern, western, and central Europe (Fig. 1). The white rectangles indicate the starting box of each track,

which is labeled with a track number. Because of the viewing geometry of Meteosat, the box area varies from approximately  $50 \times 110 \text{ km}^2$  in the north to  $50 \times 90 \text{ km}^2$  in the south of the domain. The orange barbs represent the calculated cloud motion velocity (CMV) and direction. In the center of our domain, one pixel has a sampling size of about 6 km (northward) by 3.6 km (eastward) and 2 km (northward) by 1.2 km (eastward) for the narrowband channels and the HRV channel, respectively.

For the analysis, the EUMETSAT Satellite Application Facility on Support to Nowcasting and Very Short Range Forecasting (NWC SAF) software package (Derrien and Le Gléau 2005) was used together with the KNMI cloud physical properties (CPP) retrieval (Roebeling et al. 2006), which has been developed in a framework of the Satellite Application Facility on Climate Monitoring (CM-SAF; Schulz et al. 2009). With the NWC SAF software, the cloud mask (CMA), cloud type (CT), cloud-top height (CTH), and high-resolution wind (HRW) products have been derived. The quantities  $\tau$ ,  $r_e$ , and LWP have been retrieved for cloudy pixels with CPP;  $\tau$  and  $r_e$  retrievals use simulated lookup tables for cloudy 0.6- and 1.6- $\mu\text{m}$  reflectances and are described in more detail in Roebeling et al. (2006). All these cloud properties except the HRW product ( $1 \times 1 \text{ km}^2$ ) have the MSG standard resolution of  $3 \times 3 \text{ km}^2$ . The estimation of cloud properties within CPP assumes a vertically homogeneous cloud. However, observations of shallow cumulus clouds indicate



a linear increasing liquid water content (LWC) with height within the cloud (Nicholls and Leighton 1986). Since the focus of this study is the characterization of warm convective clouds, the relation

$$\text{LWP} = \frac{5}{9} \rho_w \tau \times r_e \quad (1)$$

is used to estimate the LWP, assuming adiabatic clouds where  $\rho_w$  is the density of liquid water [see Wood and Hartmann (2006) for further discussion]. As a fourth cloud-field variable, the cloud droplet number concentration can be expressed as

$$N_d = \alpha \tau^{0.5} \times r_e^{-2.5}, \quad (2)$$

assuming adiabatic clouds with a monotonic increasing LWC and  $r_e$  (Quaas et al. 2006). The constant  $\alpha = 1.37 \times 10^{-5} \text{ m}^{-0.5}$  as given by Brenguier et al. (2000) is used in our study.

The selected cases show a high degree of spatial cloud variability. Cloudy pixels might indeed contain partially cloud-free regions in the subpixel range that are smaller than SEVIRI's narrowband spatial resolution (Roebeling et al. 2006). Consequently, SEVIRI's narrowband observations as well as retrieved cloud products might be strongly affected by this subpixel variability (Deneke et al. 2009; Wolters et al. 2010). Because of the coarse spatial resolution of MSG,  $\tau$  is usually underestimated while  $r_e$  is generally overestimated. This effect depends on viewing geometry (e.g., Horvath et al. 2014) and becomes even more pronounced for broken cumulus clouds (Wolters et al. 2010; Marshak et al. 2006). The resulting cloud property uncertainties and biases are not further investigated or corrected for this study. Instead, we focus on the characterization of the cloud-field structure as well as the spatiotemporal evolution of cloud properties. Both processes reduce the autocorrelation between space and time-lagged cloud fields.

Shallow cumulus clouds cannot be detected from Meteosat in their early initiation phase because of the limited sensor resolution. Even cumulus mediocris or congestus are oftentimes smaller than the area probed by a standard-resolution Meteosat pixel ( $\approx 20 \text{ km}^2$ ). For that reason, we additionally make use of the HRV channel, which covers a pixel area of  $1.9\text{--}2.4 \text{ km}^2$  in our domain. Furthermore, a high-resolution visible cloud mask (HRV-CMa) is calculated to separate between cloudy and cloud-free regions and to improve the case selection (Bley and Deneke 2013). We eliminate all cases where the CT products detect ice clouds and assume nonprecipitating cloud

fields, because rain formation mainly involves ice-related processes in our domain.

### 3. Method

#### a. Cloud-field tracking

Because of the relatively coarse spatial resolution of MSG, we are not able to derive characteristics representative of single cumulus clouds. Instead, we determine the statistics of a spatially extended convective cloud field within a selected box. To get a sufficient number of pixels representative of a cloud field, we analyze boxes containing convective clouds within an area of  $16 \times 16$  low-resolution or  $48 \times 48$  HRV pixels [ $\sim (60 \times 96) \text{ km}^2$ ]. The cloud fields are tracked temporally through successive satellite images from MSG. This is done in a two-step procedure.

Initially, the NWC SAF HRW product is calculated and used as a first guess of the horizontal wind (García-Pereda 2013). This product is based on a cross-correlation method and contains atmospheric motion vectors (AMVs) for pixels that are characterized by particular tracers (e.g., cloud edges) that can be matched in subsequent satellite images. We have adapted the default configuration files of the algorithm to get more motion vectors representative for the motion of low-level broken clouds, which are normally rejected by the stringent quality tests of operational AMV products (Bedka and Mecikalski 2005). Details can be found in appendix A, including the configuration file that is contained in the online supplemental material. To also consider slow cloud motions, the shortest possible time interval of 10 min is chosen. The most important input to the HRW product for our applications is the HRV channel, as the low-resolution channels are not able to properly resolve the cloud edges of small convective clouds. The output of the HRW product contains all AMVs that are found in a specific height level. We average all AMVs within our area of interest for each height level. This mean AMV yields the direction and shift within a 10-min time interval that is applied to the central pixel of the box. To identify the height level that represents the cloud-field motion best, the autocorrelation between the actual and shifted box is calculated for each level (see section 3b). The AMV that yields to the highest autocorrelation is then chosen for the tracking. The optimal AMV is divided by a factor of 2 to obtain the displacement of the cloud field at full 5-min resolution. The motion vectors are then assembled for different time steps to obtain a trajectory offering a Lagrangian perspective of the evolving cloud field (Fig. 2). As a final quality check, we tested whether the decorrelation time for the field within an Eulerian box

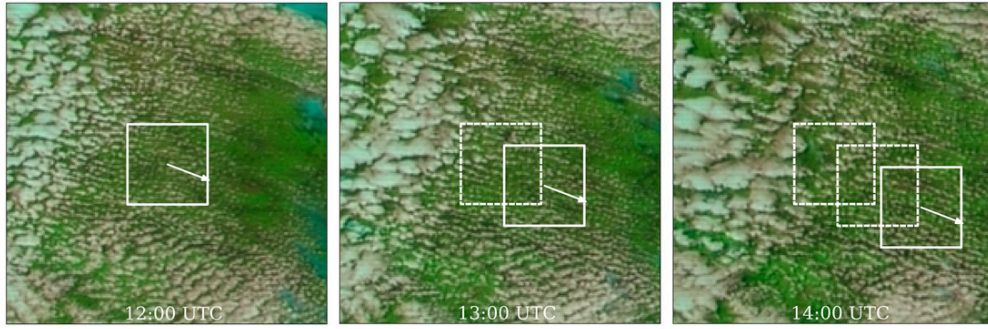


FIG. 2. Illustration of a  $48 \times 48$  box that moves along its trajectory. The white arrow indicates the direction and distance for the next center of the box, starting from the center of the previous box.

is higher than that along the Lagrangian trajectory. This happens if the mean cloud motion is so small that it cannot be accurately quantified by AMVs, which are limited to integer pixel resolution. In this case, a neighboring box yielding a higher autocorrelation for a time lag of 30 min is sought. If such a box is found, it is used to redefine the trajectory.

#### b. Autocorrelation for successive cloud fields

The autocorrelation function  $r$  that describes the similarity of successive cloud fields is used in this study to quantify the temporal persistence of cloud structures and is used as basis of our spatiotemporal analysis of clouds fields. To avoid edge effects on the box sides, the cloud fields are multiplied by a normalized Hamming window filter function.

The autocorrelation function is calculated in three different ways. First, it is calculated as time-lagged autocorrelation function for a fixed box (Euler), then along the cloud motion trajectory (Lagrange), and also for a fixed time but for different discrete displacement vectors in  $x$  and  $y$  directions to obtain the spatial autocorrelation. Figure 3 illustrates schematically how the box shifts are applied. The scheme is plotted in two dimensions collapsing the two spatial dimensions into one for easier visualization. However, the spatial box shift is not only performed in the  $x$  direction but also in the  $y$  direction.

Each Lagrangian trajectory consists of  $N = 24$  motion vectors that connect the 25 box centers to form a 2-h track with a time resolution of  $\Delta t = 5$  min. For a time lag of  $k\Delta t$ , the average autocorrelation is defined as

$$R_k = \frac{1}{N-k} \sum_{n=1}^{N-k} r(n, n+k) \quad (3)$$

for successively determined autocorrelation functions  $r(n, n+k)$  correlating the cloud field at time  $n\Delta t$  with the field at  $(n+k)\Delta t$ . The average autocorrelation function

$R_k$  represents a robust measure of the temporal persistence of a cloud field and reduces statistical variations. For the calculation of Eulerian and Lagrangian decorrelation times, time lags up to  $k = 12$ , that is, up to 60 min, are considered. For the determination of decorrelation lengths, a maximum pixel shift in row- or columnwise direction of  $k = 10$  is applied.

#### c. Decorrelation time and length

The autocorrelation as function of time lag or pixel shift typically has been found to follow an exponential decay with sufficient accuracy for our purposes.

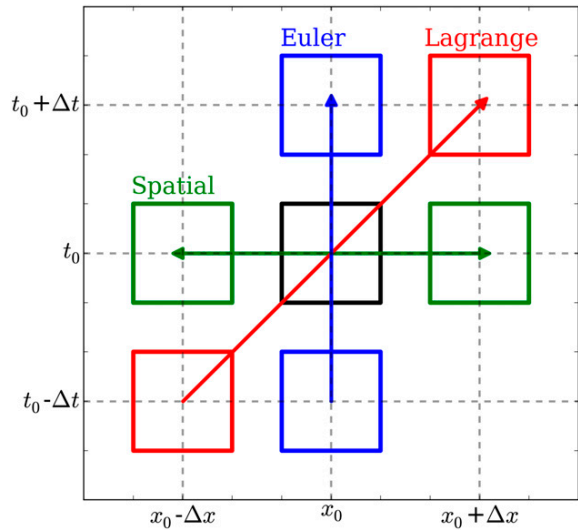


FIG. 3. Schematic diagram illustrating the way by which the Lagrangian, Eulerian, and spatial autocorrelations are applied with respect to time and space dimensions. The arrows indicate the box shift for the different approaches with constant location but varying time (blue), constant time but different spatial shifts (green), and varying time and location (red) related to the cloud-field tracks.

Therefore, the average Eulerian autocorrelation  $R_{k,E}$ , the average Lagrangian autocorrelation  $R_{k,L}$ , and the average spatial cross-correlation  $R_{k,S}$  are approximated by

$$R_{k,E} = e^{-(k\Delta t)/\tau_{D,E}}, \quad (4)$$

$$R_{k,L} = e^{-(k\Delta t)/\tau_{D,L}}, \quad \text{and} \quad (5)$$

$$R_{k,S} = e^{-(k\Delta x)/\lambda_{D,x}}, \quad (6)$$

where  $\Delta t$  and  $\Delta x$  represent the time step of 5 min and spatial distance of a pixel shift, respectively. The quantities  $\tau_{D,E}$ ,  $\tau_{D,L}$ , and  $\lambda_{D,x}$  stand for the characteristic time and space scales at which the convective cloud field has substantially changed its structure from its initial pattern. A similar definition of characteristic scales was applied by Cahalan et al. (1982). Practically, the Eulerian ( $\tau_{D,E}$ ), and Lagrangian ( $\tau_{D,L}$ ) decorrelation times as well as the decorrelation lengths ( $\lambda_D$ ) are calculated as the intersection between the  $e^{-1}$  line and the linear fit between  $R_k > e^{-1}$  and  $R_k < e^{-1}$ .

The simplest statistical model yielding the described decorrelation behavior is an autoregressive process of first order (Von Storch and Zwiers 2002), which describes a noise-driven system with some persistence. More complex statistical models, like an autoregressive process of second order, will exhibit a different decorrelation function and might ultimately better describe the observations. This has, however, not been pursued in our study and is left for future research.

#### 4. Results and discussion

In this section, we quantify the statistical parameters for all analyzed cases including their uncertainties. Relevant satellite attributes that influence the spatio-temporal characteristics of warm convective cloud fields are discussed. In section 4d, we present two case studies and their associated LWP time series including a separation between advectively and convectively induced changes of their field-averaged LWP.

##### a. Meteorological conditions

In total, 30 cases were selected in the period from April to August from the years 2012 and 2013. The spring and summer period is chosen because of favorable meteorological conditions for warm convective clouds over central Europe. The cases are characterized by different environmental conditions with respect to the cloud motion velocity and direction, synoptic situation, and cloud extent. (An overview of all tracked convective cloud fields, including the exact time and the meteorological conditions, is given in Table B1 in appendix B.)

Additionally the calculated characteristic spatiotemporal scales are included. All cloud fields are analyzed for 2 h covering the early afternoon, which is usually the time of day with the highest convection potential.

Four example cloud fields are shown in Fig. 4. Figures 4a and 4b show convective clouds forming in postfrontal cloud air conditions connected with relatively high wind speeds over northern Germany (Fig. 4a) and Poland (Fig. 4b). Both examples indicate homogeneous cloud patterns lateral to the wind direction. In contrast, Figs. 4c and 4d demonstrate example scenes with slow wind speeds with no constant wind directions.

In central Europe, warm convective cloud fields typically develop after the passage of cold fronts connected with low pressure systems when cold and humid air is advected from the Atlantic Ocean and North Sea (cases 2–8, 10, 15–22, 30). Because of large-scale horizontal advection of humid air, these cloud fields are sometimes stable over long distances ( $\sim 100$  km). Warm convective cloud fields with very low average cloud motions ( $\text{CMV} < 5 \text{ m s}^{-1}$ ) mainly occur in warm sectors or prefrontal conditions with low horizontal gradients (cases 9, 25–29). This leads to the initiation of convective clouds that can grow into deep convective systems (Senf et al. 2015). The other cases (1, 11–14, 23, 24) are associated with low pressure systems over southern and eastern Europe.

The spatial distribution of LWP,  $\tau$ ,  $r_e$ , and  $N_d$  for one selected case over Poland on 19 May 2013 is visualized in Fig. 5. The convective cloud field formed around noontime in southeasterly warm air advection due to a low pressure system over Italy. Moderate-speed CMVs were observed with  $5.5 \text{ m s}^{-1}$  in the  $x$  direction and  $6 \text{ m s}^{-1}$  in the  $y$  direction. The LWP field exhibited a spatial decorrelation length of 8 km in the north–south direction and 6.5 km in the east–west direction. All cloud properties are estimated at SEVIRI's standard resolution with a typical pixel area of  $21 \text{ km}^2$ . To illustrate the large subpixel variability in these cloud scenes, a semitransparent overlay of a high-resolution red-green-blue (RGB) image is used in Fig. 5. In general, cloudy pixels that are considered by the CPP retrieval might contain cloudy and cloud-free areas. Consequentially  $\tau$  and LWP are usually underestimated, while  $r_e$  is overestimated (Coakley et al. 2005; Jonkheid et al. 2012). However, the LWP uncertainty is likely still smaller for these broken liquid water cloud fields than that for mixed-phase clouds (Jonkheid et al. 2012). As mentioned before, we do not elaborate on these uncertainties, which have been extensively studied in the scientific literature (e.g., Zinner and Mayer 2006). Instead, we focus here on the question whether they are well suited to characterize the temporal evolution of



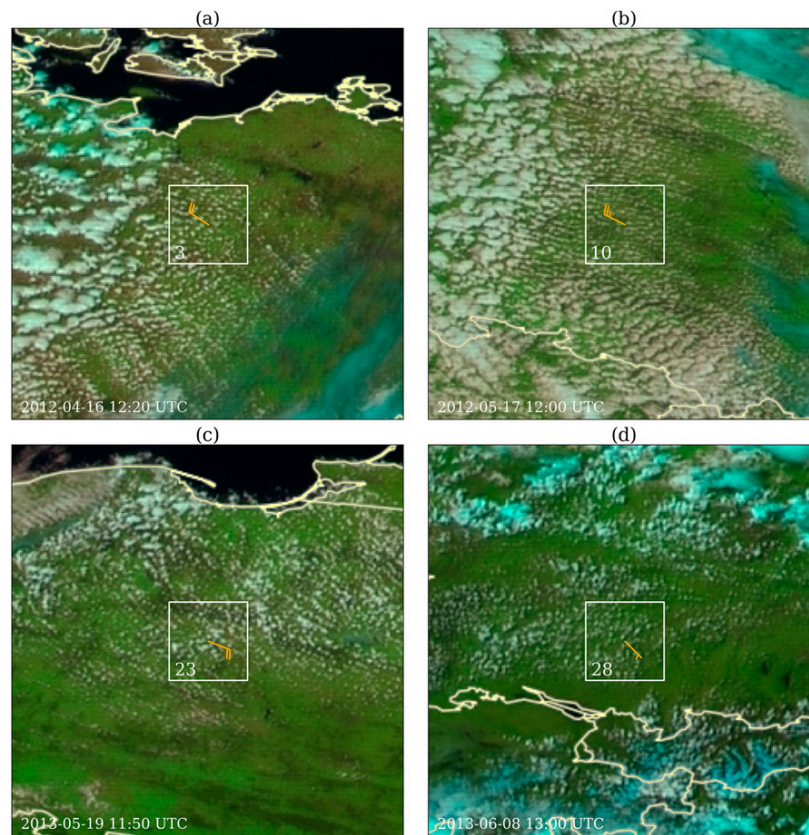


FIG. 4. Four selected cases displayed with the same markers as in Fig. 1, but magnified. The RGB images show postfrontal cases over (a) Germany and (b) Poland, (c) a case over Poland that is associated with a low over southern Europe, and (d) a case for a scattered cloud field over southern Germany in a low horizontal wind gradient environment.

cloud fields and allow a more physically based description than that offered by radiances.

*b. Comparison of radiances and cloud properties with respect to their correlation behavior*

In this section, we present the decorrelation times obtained for the different spectral reflectance channels of MSG and compare them to those found for various retrieved cloud properties. This analysis is done to determine the temporal persistence of the different parameters. Furthermore, we demonstrate the reliability of our cloud-field-tracking method.

The following results are based on Eq. (3) and calculated for the Lagrangian tracks (listed in Table B1). As described earlier, these tracks are based on the NWC SAF HRV motion vectors, which are mainly calculated from HRV reflectance images. Figure 6 contrasts the Eulerian (Fig. 6a) and Lagrangian (Fig. 6b) autocorrelation function for the  $0.6\text{-}\mu\text{m}$  channel, the  $0.8\text{-}\mu\text{m}$  channel, the HRV channel, and a coarse-grained HRV channel.

The coarse-grained HRV channel has been obtained from the standard HRV channel by averaging  $3 \times 3$  pixels to approximate the standard MSG horizontal resolution. This averaging has been performed to test the sensitivity of the decorrelation time to spatial resolution.

At this point, we caution that 30 cases might be too few to assess whether some of the smaller differences in the average decorrelation times are statistically significant. However, larger differences are likely robust, especially those found when contrasting the decorrelation times for different cloud properties.

The average decorrelation times for all spectral channels are nearly 2 times longer for the Lagrangian than for the Eulerian perspective. Regardless of the perspectives, the  $0.6\text{-}\mu\text{m}$  channel shows the highest decorrelation times, while the HRV channel exhibits rather low values. This is likely caused by the threefold higher spatial resolution of the HRV channel, which better resolves small-scale variability in the inhomogeneous structure of convective cloud fields. If this small-scale and evidently short-lived

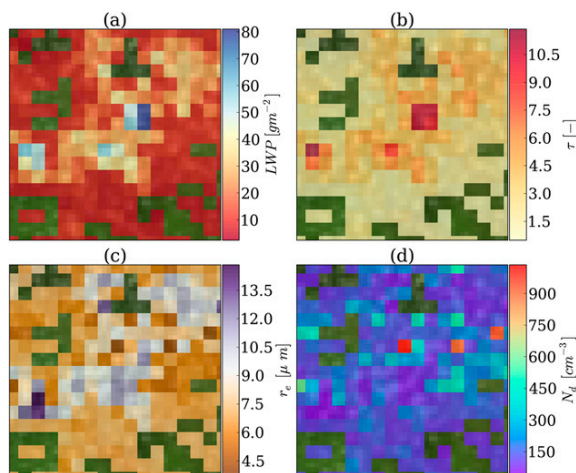


FIG. 5. Two-dimensional fields of cloud properties for case 23 on 19 May 2013 over Poland. The RGB composite is plotted in the background. Illustrated are (a) LWP, (b)  $\tau$ , (c)  $r_e$ , and (d)  $N_d$ . While the cloud properties contain only  $16 \times 16$  low-resolution pixels, the underlying RGB image involves  $48 \times 48$  HRV pixels.

cloud variability is removed by smoothing to lower resolution, an increase in the temporal autocorrelation is found. As the broadband spectral response of the HRV channel overlaps the response functions of the 0.6- and 0.8- $\mu\text{m}$  channels, the temporal autocorrelation of the HRV channel is expected to lie between that of both narrowband channels. This is in fact observed, with a Lagrangian decorrelation time for the coarse-grained HRV channel of 31 min, which lies between  $\tau_{D,L(0.8\mu\text{m})}$  (27.7 min) and  $\tau_{D,L(0.6\mu\text{m})}$  (33.2 min). In the Eulerian perspective, the relatively higher  $\tau_{D,E(0.8\mu\text{m})}$  is likely caused by stationary patterns in the underlying surface reflectance caused by the strong reflectance of vegetation at 0.8- $\mu\text{m}$  wavelength.

In the next step, the correlation analysis is repeated for different cloud properties of the convective cloud fields. The result for  $\tau$ ,  $r_e$ , LWP, and  $N_d$  is shown in Fig. 7. We have additionally added the autocorrelation of the 0.6- $\mu\text{m}$  reflectance as reference. In both perspectives, the correlation functions of the 0.6- $\mu\text{m}$  reflectance and  $\tau$  show the best results and are hardly distinguishable. This is expected, because the retrieval of  $\tau$  is highly dependent on the 0.6- $\mu\text{m}$  reflectance (Nakajima and King 1990; Roebeling et al. 2006) and therefore shares similar spatial statistics. The shortest decorrelation times are found for  $N_d$  and  $r_e$ , with both decorrelating faster than 20 min. It remains unclear whether this behavior is physically caused or is attributable to uncertainties in the retrievals. In contrast,  $\tau_{D,L(\text{LWP})}$  (31 min) lies in a similar range with  $\tau_{D,L(\tau)}$  (34.1 min) and  $\tau_{D,L(0.6\mu\text{m})}$  (33.2 min). The shaded areas demonstrate a high standard deviation

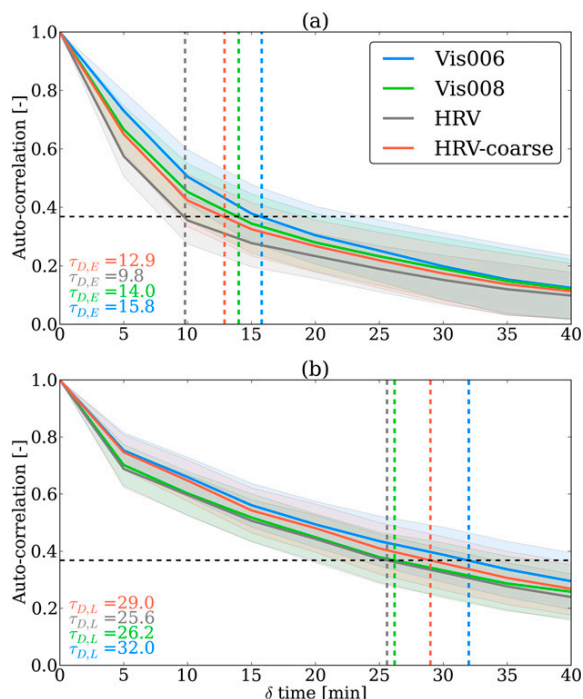


FIG. 6. (a) Eulerian and (b) Lagrangian autocorrelation function averaged for all cases and applied to MSG's standard visible channels 0.6 and 0.8  $\mu\text{m}$ , the HRV channel, and an additional coarse-grained HRV channel with MSG's standard resolution. The shaded areas illustrate the standard deviation, and the dashed vertical lines show the decorrelation times  $\tau_D$  for the four channels. The horizontal black line marks the decorrelation threshold.

of approximately  $\pm 5$  min, which has been determined from the case-to-case variations. In conclusion, even besides possible shortcomings in the retrievals of cloud properties due to subpixel variability, the structures of  $\tau$  and LWP fields can be used to characterize the spatiotemporal evolution of warm convective cloud fields. In contrast to radiances, LWP in particular has the advantage of being a physically meaningful and interpretable quantity, which is readily available as output from atmospheric models. Hence, it can offer better insights into the underlying physical processes of clouds, and is well suited for model evaluation purposes. Our results also demonstrate, however, that the observed decorrelation time depends on sensor resolution, which needs to be taken into account in such a model evaluation study.

### c. Spatiotemporal characteristics of LWP fields

The relation between  $\tau_{D,E}$ ,  $\tau_{D,L}$ , and the CMVs is displayed in Fig. 8 for all analyzed cases. While  $\tau_{D,E}$  decays with increasing CMV,  $\tau_{D,L}$  remains relatively constant, having a mean value of 31 min. The average Eulerian decorrelation time is 15.5 min. For CMVs lower than  $5 \text{ m s}^{-2}$ ,

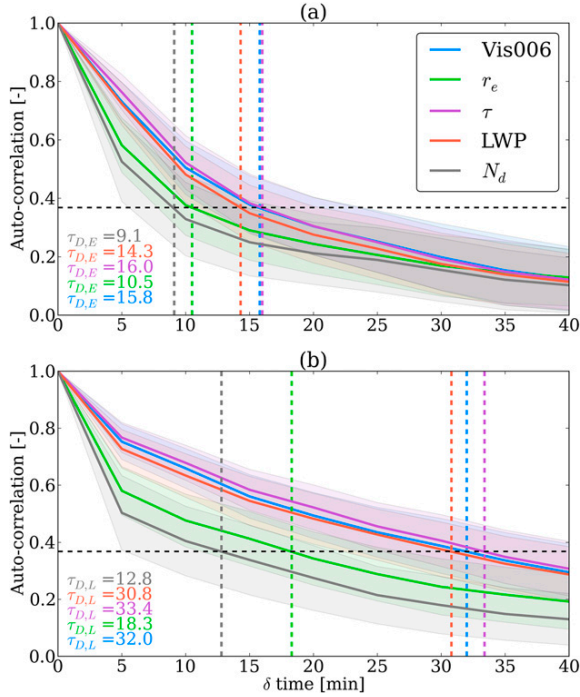


FIG. 7. As in Fig. 6, but on the basis of cloud products ( $r_e$ ,  $\tau$ , LWP, and  $N_d$ ). The autocorrelation function of the 0.6- $\mu\text{m}$  channel is added for comparison.

$\tau_{D,E}$  and  $\tau_{D,L}$  are hardly distinguishable because the resulting track length is smaller than the box area, and the Eulerian and Lagrangian cloud fields strongly overlap. If the actual CMV increases above this value,  $\tau_{D,E}$  drops rapidly. The strong decay in  $\tau_{D,E}$  is caused by the fact that the convective cloud fields that are subsequently advected into the box are both temporally and spatially separated from the instantaneous cloud field. Thus, the advection-based change in the LWP structures is added to the internal or Lagrangian change of the LWP fields, an effect that increases with wind speed. The shaded red and blue areas indicate the standard deviation of  $\tau_{D,L}$  and  $\tau_{D,E}$  for a running average over different cloud motion categories.

We now assume that the statistical properties of the LWP fields are, to the first order, stationary, homogeneous, and described by Eqs. (4)–(6). As a result, the Eulerian time scale is decreased by perturbations of the spatial scales  $\lambda_{D,x}$  and  $\lambda_{D,y}$  that are advected by the cloud motion; that is,

$$\frac{1}{\tau_{D,E}} = \frac{1}{\tau_{D,L}} + \frac{|u|}{\lambda_{D,x}} + \frac{|v|}{\lambda_{D,y}}. \quad (7)$$

Here,  $u$  and  $v$  are the cloud motion velocities in the  $x$  and  $y$  directions, respectively. Please note that all time and space

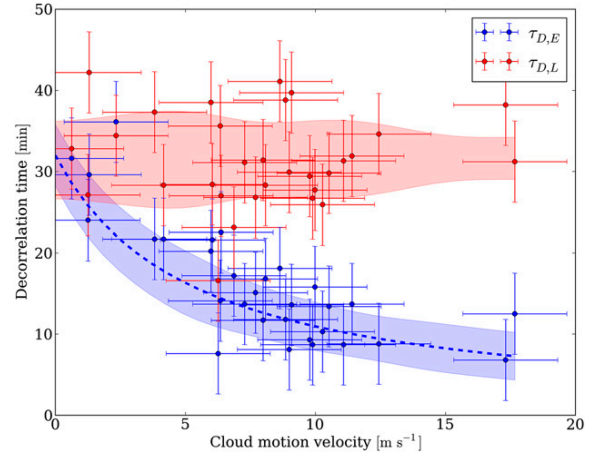


FIG. 8. Relation between the Eulerian (blue) and Lagrangian (red) decorrelation time  $\tau_D$  and the CMV from MSG observations. The error bars represent the uncertainty of the CMV ( $2 \text{ m s}^{-1}$ ) and of  $\tau_D$  (5 min), while the shaded colored areas indicate the standard deviation. The blue dashed line shows the calculated Eulerian function given by Eq. (7).

scales are positively defined. In the limit of  $u$  and  $v$  approaching  $0 \text{ m s}^{-1}$ ,  $\tau_{D,E}$  and  $\tau_{D,L}$  become equal. In the limit of a conserved, frozen LWP structure in a Lagrangian reference frame, that is,  $\tau_{D,L} \rightarrow \infty$ ,  $\tau_{D,E}$  is solely determined by advection and only depends on  $u$ ,  $v$ ,  $\lambda_{D,x}$ , and  $\lambda_{D,y}$ .

The above relation (7) is shown in Fig. 8 by a dashed blue line as a function of CMV, where constant, case-average values of  $\tau_{D,L} = 31 \text{ min}$  and  $\lambda_{D,x} = 7.3 \text{ km}$  have been assumed. For faster CMVs, derived  $\tau_{D,E}$  converge to approximately 5–10 min because of the temporal resolution constraints. A CMV uncertainty of  $2 \text{ m s}^{-1}$  is estimated from the discretization bias, which corresponds to the speed needed for one HRV pixel shift within 5 min. The uncertainty of the decorrelation time is around 5 min and has been derived from the standard deviation of  $\tau_{D,L}$  across all cases.

The above relation linking Eulerian and Lagrangian time scales has important implications for the interpretation of remote sensing observations. When analyzing the temporal characteristics of a time series of ground-based observations, one has to keep in mind that the observed changes obtained from a single point measurement are always a combination of an inherent, Lagrangian temporal change, and an advective component that depends on both wind speed and a decorrelation length scale. Tracking these cloud fields in a Lagrangian reference frame allows us to separate both contributions but can be only performed with either geostationary satellite observations or a network of ground-based measurements with sufficient spatial sampling like scanning radars or cloud cameras.



Figure 9 contrasts the observed and the estimated Eulerian decorrelation times. The estimated Eulerian decorrelation time is given by the reciprocal of Eq. (7) and illustrates the link between the observed Lagrangian decorrelation time, the cloud motion velocity, and the spatial decorrelation length. The values show a rather good correlation for low decorrelation times between 10 and 20 min that are associated with high cloud motion velocities, while the spread strongly increases for high decorrelation times. The error bars of the estimated decorrelation times that are based on Gaussian error propagation even increase up to 70% for the high decorrelation times. These deviations are due to the sensor limitations of SEVIRI that lead to high tracking uncertainties especially for low cloud motions in subpixel range. However, the Pearson correlation coefficient of 0.81 demonstrates a reliable connection of the different spatiotemporal scales.

In addition to the temporal characteristics, the spatial characteristics of the cloud fields are considered by calculating the autocorrelation  $R_{k,S}$  of the LWP fields as a function of distance from the actual cloud-field position. The quantities  $\lambda_{D,x}$  and  $\lambda_{D,y}$  are related to the typical spatial scales of LWP in the  $x$  and  $y$  directions, respectively. Averaged over all cases,  $\lambda_{D,x}$  is 6.5 km and  $\lambda_{D,y}$  is 8 km, with a standard deviation of 2 km for both. The difference between the two values might result from the different sensor resolutions in both directions. Figure 10 shows the relation between  $\lambda_{D,x}$ ,  $\lambda_{D,y}$ , and the mean cloud diameter. The cloud diameter is determined as mean diameter of connected cloudy areas in a box referring to pixels that have a LWP higher than zero. An increase of the correlation length with increasing cloud diameter is observed. This implies that cumulus clouds lead to an even shorter decorrelation length. In contrast, we expect that much longer decorrelation lengths are obtained for more homogeneous stratocumulus cloud decks.

A statistical link between the spatial and temporal scales of cumulus cloud fields was already demonstrated by Feijt and Jonker (2000). They showed that for a cumulus and stratocumulus case, the temporal scales of a high-resolution LWP time series measured at one station could be matched to the spatial scales inferred from an LWP field obtained from a polar-orbiting satellite. The relation between correlation and distance reported here is also consistent with the findings of Slobodda et al. (2015). They report an exponential decrease of correlation with increasing distance especially for the three solar MSG channels (0.6, 0.8, and 1.6  $\mu\text{m}$ ), which carry information about the cloud microphysical and optical properties. Further, they concluded that correlation lengths are smaller for scenes with lower cloud coverage. The much larger

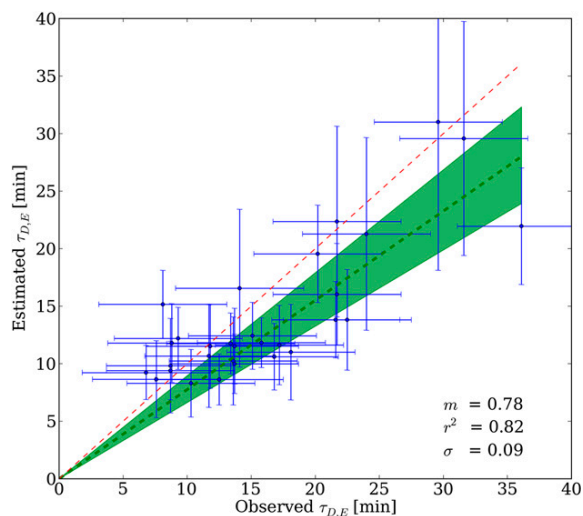


FIG. 9. Relation between the observed and estimated Eulerian decorrelation times. The estimated time connects the Lagrangian decorrelation time with the spatial decorrelation length and the cloud motion velocity according to Eq. (7). The observed average error is given as 5 min, while the estimated error results from Gaussian error propagation. The red dashed line illustrates the identity line. The green dashed line shows the linear fit function, and the surrounding shaded area spans the 5th and 95th percentiles using a bootstrap approach that indicates the error variability.

decorrelation distances reported by Slobodda et al. (2015) can result from the differences in methodology and our selection of scenes with cumulus convection. In their study, time series of fixed pixels representing ground-based measurement sites have been correlated as a function of pixel distance. We, however, apply the correlation analysis to cloud-field structures in boxes that are significantly larger than the field characteristic scales. Furthermore, the decorrelation distance and time increase strongly if the considered area is increased (Cahalan et al. 1982). For a large region over the Pacific Ocean, they found correlation lengths of up to 600 km and Lagrangian correlation time scales exceeding two days. Because of the differences in region area, methodology, and data, a comparison of our results with their reported values is not possible.

#### d. Temporal evolution of the cloud field-averaged LWP

The total temporal change of the box-averaged  $\overline{\text{LWP}}$  is given by

$$D_t(\overline{\text{LWP}}) = \partial_t(\overline{\text{LWP}}) + \mathbf{u} \cdot \nabla(\overline{\text{LWP}}). \quad (8)$$

Here, the total derivative  $D_t(\overline{\text{LWP}})$  is given as sum of the partial derivative  $\partial_t(\overline{\text{LWP}})$  and the advection of the gradient  $\nabla(\overline{\text{LWP}})$  with horizontal wind speed  $\mathbf{u}$ .

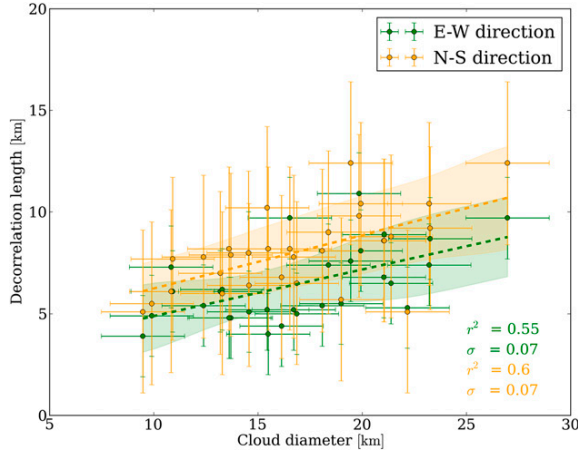


FIG. 10. Relation between the decorrelation length  $\lambda_D$  in the east-west (green) and north-south (orange) directions and the average cloud diameter  $d$ . The error bars represent the uncertainty of  $d$  (2 km) and  $\lambda_D$  (4 km), while the shaded colored areas indicate the standard deviation. The solid lines show the linear fit of both functions.

In this part of the study, we investigate the temporal change in average LWP for warm convective clouds. LWP is connected to the total mass of condensed water assuming that changes in box area and contributions from frozen hydrometeors can be neglected. Reformulating Eq. (8), a discretized version is given by

$$\Delta_t(\overline{\text{LWP}}) = \delta_t(\overline{\text{LWP}}) + u\delta_x(\overline{\text{LWP}}) + v\delta_y(\overline{\text{LWP}}), \quad (9)$$

where  $\Delta_t(\overline{\text{LWP}})$ ,  $\delta_t(\overline{\text{LWP}})$ , and  $\delta_{x,y}(\overline{\text{LWP}})$  denote the Lagrangian change, Eulerian change, and local spatial differences, respectively. On the one hand, if  $\delta_t(\overline{\text{LWP}})$  is obtained from the Eulerian perspective, it can be directly compared with ground-based measurements. On the other hand, if we assume that  $\overline{\text{LWP}}$  is affected by neither precipitation nor glaciation,  $\Delta_t(\overline{\text{LWP}})$  is directly linked to evaporation and condensation within the cloud field.

The derivative  $\Delta_t(\overline{\text{LWP}})$  is determined along the Lagrangian trajectory. Consequently  $\Delta_t(\overline{\text{LWP}}) > 0$  implies an increase in the mass of liquid water, that is, condensation, while  $\Delta_t(\overline{\text{LWP}}) < 0$  implies evaporation. The advective part is divided into two terms, the spatial change along the  $x$  direction given by  $\delta_x(\overline{\text{LWP}})$  and along the  $y$  direction given by  $\delta_y(\overline{\text{LWP}})$ , and multiplied by the CMVs  $u$  and  $v$ , respectively. As in Eq. (7),  $\Delta_t(\overline{\text{LWP}})$  and  $\delta_t(\overline{\text{LWP}})$  are equal if the advective part is zero.

The time series  $\Delta_t(\overline{\text{LWP}})$  and  $\delta_t(\overline{\text{LWP}})$  and the total average LWP in both perspectives are shown in Fig. 11 for two exemplary cases. The bars illustrate the magnitude of the LWP change within 5 min but are scaled to

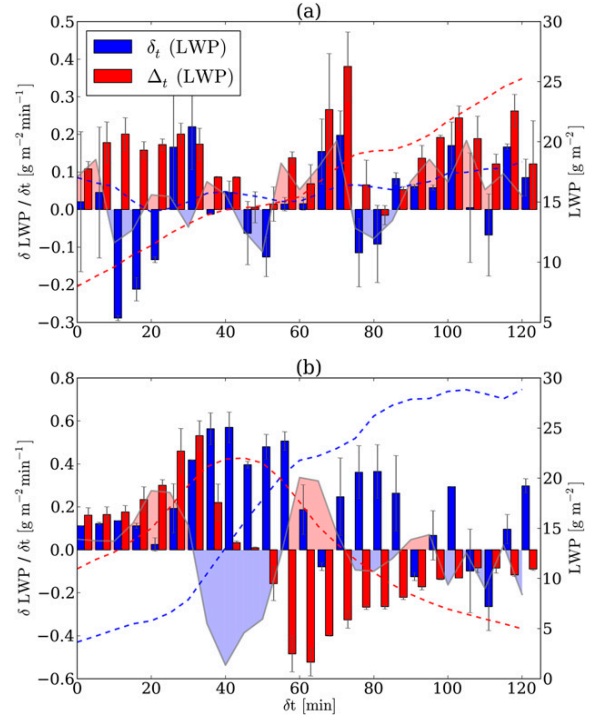


FIG. 11. Time series of the box-averaged LWP changes  $\delta_t(\overline{\text{LWP}})$  and  $\Delta_t(\overline{\text{LWP}})$  for the Eulerian (blue bars) and the Lagrangian (red bars) perspective, respectively. The error bars illustrate the standard deviation, and the gray line shows the absolute difference between  $\Delta_t(\overline{\text{LWP}})$  and  $\delta_t(\overline{\text{LWP}})$ . Red shaded areas indicate  $|\Delta_t(\overline{\text{LWP}})| > |\delta_t(\overline{\text{LWP}})|$ , whereas blue areas indicate the opposite. The y axis on the right-hand side demonstrates the Eulerian (blue dashed line) as well as the Lagrangian (red dashed line) time series of the cloud-field average LWP. Shown are (a) case 2 and (b) case 30.

rate per minute. The right y axis represents the cloud-field-averaged LWP time series concerning the Eulerian (blue line) and the Lagrangian (red line) perspective. The shaded areas display the absolute difference between  $\Delta_t(\overline{\text{LWP}})$  and  $\delta_t(\overline{\text{LWP}})$ . For red areas, the Lagrangian changes dominate the local tendencies. Figure 11a shows case 2 over northern Germany close to the North Sea. A cold front passed the region before the start of the track. The advection velocity was  $9 \text{ m s}^{-1}$ , which caused a track length of approximately 60 km. Although the boxes are overlapping for most of the track, Eulerian and Lagrangian changes are quite different. The average LWP is clearly increasing in the Lagrangian perspective, while the LWP change at a fixed location is much smaller, resulting in only a slight increase in LWP. This implies that cumulus clouds grow along their path because of condensation. However, this increase is masked to a large extent by advection in the Eulerian perspective. In contrast, case 30 (see Fig. 11b) represents an example for a rather high CMV of  $18 \text{ m s}^{-1}$ .



For a fixed location, the mean LWP is continuously increasing, while the tracked cloud field exhibits a different temporal evolution. A maximum  $\overline{\text{LWP}}$  of around  $20 \text{ g m}^{-2}$  is reached after 40 min, before it drops down again to a small value of  $5 \text{ g m}^{-2}$ , indicating the dissipation of the cloud field.

These two cases illustrate that the temporal changes of cloud properties are dependent on the observational perspective, and that the Lagrangian is preferable over the Eulerian perspective for a physical interpretation of governing processes. This is especially true in the presence of strong winds and large gradients in the cloud properties. The accuracy of the Lagrangian analysis is, however, affected by tracking uncertainties in addition to other uncertainties, which has to be taken into account in the interpretation of quantitative results. In the limit of low CMVs, both perspectives should converge to the same result. In our setup, however, the limited resolution of motion vectors that is fixed to multiples of the pixel resolution introduces complications for very low wind speeds.

## 5. Conclusions and outlook

In the present study, we have investigated the spatiotemporal evolution of warm convective cloud fields obtained from Meteosat SEVIRI observations. An advantage of Meteosat and similar geostationary satellites is their ability to monitor convective clouds and to fully resolve the cloud life cycle from the early stages of development on. We have used 30 cases of convective clouds under different synoptic conditions over central Europe as the basis of this investigation.

Solar reflectances have been used together with cloud products (HRV-CMa, CT,  $\tau$ ,  $r_e$ , LWP,  $N_d$ , and CMV) to characterize the spatiotemporal evolution of convective cloud fields. First, trajectories have been determined from sequences of HRV images. Boxes covering  $16 \times 16$  SEVIRI standard-resolution pixels have been used to obtain an estimate of the mean properties of the convective clouds. The temporal and spatial persistence of different cloud properties has been studied with special focus on the differences between the Eulerian (i.e., fixed in space) and the Lagrangian (i.e., track following) perspectives. Assuming a Gaussian function for the autocorrelation function, which corresponds to the assumption of a first-order autoregressive process, the  $e$ -folding value has been determined as characteristic time and space scales.

The decorrelation times of SEVIRI's solar reflectances has been studied first. The decorrelation times for the  $0.6\text{-}\mu\text{m}$  channel are generally larger than the decorrelation times for the  $0.8\text{-}\mu\text{m}$  channel, likely because of influence of surface reflectance in particular caused by vegetation. In addition, the decorrelation of

the HRV channel at high spatial resolution ( $1.2 \times 2 \text{ km}^2$ ) and SEVIRI standard resolution ( $3.6 \times 6 \text{ km}^2$ ) has been compared, which has been obtained by coarse graining. The reduction in resolution results in an increase of around 3–5 min in the corresponding decorrelation times. This implies that small-scale variability in cloud structures decorrelate faster, and thus the decorrelation times are highly sensitive to the spatial resolution of the satellite sensor.

The decorrelation times of different retrieved cloud products have been determined and compared to those obtained for the reflectances. It has been found that fields of  $r_e$  and  $N_d$  exhibited much less persistence than LWP and  $\tau$ , which showed comparable decorrelation times to the  $0.6\text{-}\mu\text{m}$  channel. This implies that  $r_e$  and  $N_d$  are not suited as tracers for tracking. It remains unclear whether this behavior is attributable to physical reasons or is the consequence of retrieval uncertainties.

Based on our previous findings, LWP fields have been used in our further analyses, as LWP is a quantity that should be insensitive to surface heterogeneity, facilitates a process-based interpretation, and is readily available from atmospheric models and thus allows a direct comparison with model results.

The temporal evolution of box-averaged LWP was contrasted for cloud fields adopting both the Lagrangian and Eulerian perspectives. Excluding precipitation and freezing, changes in LWP in a Lagrangian reference frame are attributable to condensation and evaporation, which is essentially triggered by local convection and mixing processes. For our cases, an average decorrelation time of about 31 min has been found. The budget in an Eulerian or fixed-in-space reference frame can be significantly influenced by the advection of LWP gradients. Thus, the Eulerian decorrelation time is always lower than the Lagrangian one and depends also on the wind speed and the spatial decorrelation length scale. Typical decorrelation lengths have been found to be 6.5 km in the  $x$  direction and 8 km in the  $y$  direction. The differences between Eulerian and Lagrangian time series have been discussed for two cases.

Several sources for uncertainties have been identified that can affect the relation between the characteristic scales. The spatial decorrelation scale of 7.3 km is close to the sensor resolution of Meteosat. Furthermore, warm convective clouds often exhibit slow cloud motion velocities. This leads to uncertainties in our cloud-field tracking, because the spatial resolution of the narrowband channels and hence also the cloud properties is approximately  $3.6 \times 6 \text{ km}^2$ , which is coarser than the displacement of the cloud field within 5 min. To overcome this limitation and take into account subpixel shifts for an accurate estimation of spatial scales,

TABLE B1. Overview of cases including the track number, time and date of the track starting box as well as its longitude and latitude, the average CMV, the track length between the central pixel of the starting box and the central pixel of the ending box, the Eulerian ( $\tau_{D,E}$ ) and Lagrangian ( $\tau_{D,L}$ ) decorrelation time, and the decorrelation length in the  $x$  direction ( $\lambda_{D,x}$ ) and  $y$  direction ( $\lambda_{D,y}$ ).

Track	Time and date	Lon (°E)	Lat (°N)	CMV (m s <sup>-1</sup> )	Track length (km)	$\tau_{D,E}$ (min)	$\tau_{D,L}$ (min)	$\lambda_{D,x}$ (km)	$\lambda_{D,y}$ (km)
001	1200 UTC 14 Apr 2012	13.12	51.5	6.0	43.1	20.2	38.5	10.9	9.8
002	0930 UTC 16 Apr 2012	8.73	53.72	8.6	62.2	18.1	41.1	5.1	6.4
003	1220 UTC 16 Apr 2012	11.72	52.85	8.9	63.8	11.8	38.8	5.2	7.8
004	1220 UTC 16 Apr 2012	3.33	48.44	11.1	79.8	8.7	31.3	5	6.5
005	1340 UTC 16 Apr 2012	12.14	52.5	9.1	65.4	13.6	39.7	4.4	6.8
006	1200 UTC 21 Apr 2012	14.45	52.78	6.9	49.5	17.2	23.1	4	8.2
007	1200 UTC 21 Apr 2012	-0.68	47.44	12.4	89.6	8.8	34.6	7.4	9
008	1200 UTC 21 Apr 2012	14.37	52.39	7.7	55.4	15.1	26.8	5.2	10.2
009	1330 UTC 4 May 2012	12.1	49.7	3.8	27.5	21.7	37.3	7.3	6.1
010	1200 UTC 17 May 2012	18.54	51.53	10.3	74.0	10.3	25.9	5.5	5.7
011	1230 UTC 22 May 2012	10.69	52.59	6.4	45.9	22.5	27.0	6.1	7
012	1230 UTC 22 May 2012	11.7	51.94	6.3	45.7	14.1	35.6	6.2	6
013	1230 UTC 22 May 2012	16.66	52.57	6.3	45.1	7.6	16.6	3.9	5.1
014	1200 UTC 25 May 2012	20.14	50.75	6.0	43.5	21.6	28.4	6.8	8.6
015	1020 UTC 13 Apr 2013	3.8	50.6	10.5	75.8	13.4	29.8	8.7	9.2
016	1130 UTC 16 Apr 2013	11.47	53.56	10.0	71.9	15.8	27.7	7.6	12.4
017	1250 UTC 18 Apr 2013	7.5	52.6	17.7	127.2	12.5	31.2	8.9	8.6
018	1200 UTC 12 May 2013	3.18	49.4	9.8	70.4	9.3	29.4	7.4	10.4
019	1240 UTC 12 May 2013	9.09	51.35	9.0	64.8	8.1	29.9	9.7	12.4
020	1240 UTC 12 May 2013	5.94	47.49	8.0	57.5	11.7	31.4	5.3	5.1
021	1140 UTC 15 May 2013	0.78	48.84	11.4	82.2	13.7	31.9	6.5	8.8
022	1250 UTC 15 May 2013	-0.68	47.44	9.9	71.3	8.7	26.7	5.4	8.1
023	1150 UTC 19 May 2013	18.3	52.67	7.3	52.4	13.7	31.1	4.8	7.9
024	1230 UTC 19 May 2013	18.6	52.5	8.1	58.2	16.8	28.3	4.8	8.2
025	1250 UTC 19 May 2013	14.47	51.92	4.2	30.0	21.7	28.3	6.1	7.7
026	1100 UTC 8 Jun 2013	5.51	49.34	2.3	16.8	36.1	34.4	8.1	10.4
027	1100 UTC 8 Jun 2013	9.645	51.2	0.6	4.5	31.6	32.8	8	8
028	1300 UTC 8 Jun 2013	9.92	48.3	1.3	9.1	24.0	27.1	4.9	5.5
029	1300 UTC 8 Jun 2013	9.5	48.8	1.3	9.4	29.6	42.2	5.4	7.8
030	1250 UTC 15 Jun 2013	5.82	52.32	17.3	124.7	6.8	38.2	9.7	8.2

the use of the HRV channel with a threefold higher spatial resolution is essential.

This study demonstrates that the spatiotemporal characterization of warm convective clouds is currently limited by the spatial sensor resolution of Meteosat. Carbajal Henken et al. (2011) already found that SEVIRI's standard resolution is not sufficient to fully resolve the small-scale spatial variability required for the identification of warm convective clouds, and used an estimate of  $\tau$  based on the HRV channel. The additional use of the HRV channel can thus not only improve the tracking accuracy (Zinner et al. 2008), but can also help to better resolve small-scale cloud variability. A successful application of the HRV reflectances to improve the spatial resolution of narrowband images was presented by Deneke and Roebeling (2010). Bley and Deneke (2013) developed an HRV-CMa to improve the detection of small-scale convective clouds. The HRV channel was further applied to sharpen partly cloudy IR satellite pixels for improving convective initiation detection schemes (Mecikalski et al. 2013).

These studies support the concept that the HRV channel can help to overcome the limitations due to

SEVIRI's standard spatial resolution noted in this work. Within the framework of the Germany-wide research initiative High Definition Clouds and Precipitation for Climate Prediction [HD(CP)<sup>2</sup>] (Dipankar et al. 2015), the authors are therefore currently developing a cloud property retrieval based on the HRV channel, which includes downscaled cloud properties ( $\tau$ ,  $r_e$ , and LWP). Future plans also include the application of the spatiotemporal analysis presented here to the high-resolution simulations of icosahedral nonhydrostatic (ICON)-LES, which cover Germany with a horizontal resolution of 150 m.

The analysis demonstrates the advantage of the Lagrangian perspective for studying convective and advective processes that are influenced by cloud variability. These results should be considered in future modeling studies to evaluate and improve stochastic parameterizations of cumulus convection. Further comparisons of the spatiotemporal characteristics of convective clouds with high-resolution model results are essential to better understand and reduce their uncertainties.

On the one hand, the methods used in this investigation can serve as basis for an evaluation of the realistic

representation of clouds in ICON-LES including their spatiotemporal behavior. On the other hand, the high resolution of the model runs enable a quantification of the resolution dependence of the temporal and spatial scales determined in this article, and can thus help to quantify the information gains expected from future geostationary satellites such as Meteosat Third Generation with improved spatial and temporal resolutions. It will have a 10-min standard repeat cycle for the full disk (Stuhlmann et al. 2005) and an improved spatial resolution of 1 km for all solar channels, which will offer the great opportunity to investigate the temporal evolution of cumulus cloud fields over other relevant climatic regions (e.g., the Atlantic warm pool) using the techniques introduced here.

**Acknowledgments.** The position of the first author was funded by the German Ministry of Education and Research (BMBF) under Grant 01LK1210B. The study has been done in the framework of the Germany-wide research initiative High Definition Clouds and Precipitation for Climate Prediction [HD(CP)<sup>2</sup>]. Fabian Senf acknowledges funding within the Hans Ertel Centre for Weather Research. We thank EUMETSAT as well as the NWC SAF and the KNMI CPP teams for providing data and retrieval algorithms and in addition Zsófia Kocsis for her valuable suggestions regarding the configuration of the NWC SAF HRW retrieval. Many thanks also are given to our colleagues, especially to Andreas Macke and Johannes Quaas, for their support and feedback on earlier versions of the manuscript. We also thank the four anonymous reviewers for their thoughtful comments and suggestions, which helped to improve the final version of the manuscript.

## APPENDIX A

### Configuration of the HRW Tools

The configuration file of the HRW product has been adapted to obtain more tracers especially for small cumulus structures with low reflectance values. This could be realized by considering more tracers for the vector calculation even for a slightly smaller quality threshold. More details can be found in the configuration text file that is available in the online supplemental material.

## APPENDIX B

### Overview of Cases

Table B1 gives an overview of all analyzed cases including the track identification number, date and time of

the track starting box as well as its longitude and latitude, the average CMV, the track length between the central pixel of the starting box and the central pixel of the ending box, the Eulerian ( $\tau_{D,E}$ ) and Lagrangian ( $\tau_{D,L}$ ) decorrelation time, and the decorrelation length in the  $x$  ( $\lambda_{D,x}$ ) and  $y$  ( $\lambda_{D,y}$ ) directions.

## REFERENCES

- Albrecht, B. A., 1989: Aerosols, cloud microphysics, and fractional cloudiness. *Science*, **245**, 1227–1230, doi:10.1126/science.245.4923.1227.
- Bedka, K. M., and J. R. Mecikalski, 2005: Application of satellite-derived atmospheric motion vectors for estimating mesoscale flows. *J. Appl. Meteor.*, **44**, 1761–1772, doi:10.1175/JAM2264.1.
- Bley, S., and H. Deneke, 2013: A threshold-based cloud mask for the high-resolution visible channel of Meteosat Second Generation SEVIRI. *Atmos. Meas. Tech.*, **6**, 2713–2723, doi:10.5194/amt-6-2713-2013.
- Brenguier, J.-L., H. Pawlowska, L. Schüller, R. Preusker, J. Fischer, and Y. Fouquart, 2000: Radiative properties of boundary layer clouds: Droplet effective radius versus number concentration. *J. Atmos. Sci.*, **57**, 803–821, doi:10.1175/1520-0469(2000)057<0803:RPOBLC>2.0.CO;2.
- Brown, A., and Coauthors, 2002: Large-eddy simulation of the diurnal cycle of shallow cumulus convection over land. *Quart. J. Roy. Meteor. Soc.*, **128**, 1075–1093, doi:10.1256/Q003590002320373210.
- Cahalan, R. F., D. A. Short, and G. R. North, 1982: Cloud fluctuation statistics. *Mon. Wea. Rev.*, **110**, 26–43, doi:10.1175/1520-0493(1982)110<0026:CFS>2.0.CO;2.
- Carbajal Henken, C., M. J. Schmeits, H. Deneke, and R. A. Roebeling, 2011: Using MSG-SEVIRI cloud physical properties and weather radar observations for the detection of Cb/TCu clouds. *J. Appl. Meteor. Climatol.*, **50**, 1587–1600, doi:10.1175/2011JAMC2601.1.
- Clement, A. C., R. Burgman, and J. R. Norris, 2009: Observational and model evidence for positive low-level cloud feedback. *Science*, **325**, 460–464, doi:10.1126/science.1171255.
- Coakley, J. A., M. A. Friedman, and W. R. Tahnk, 2005: Retrieval of cloud properties for partly cloudy imager pixels. *J. Atmos. Oceanic Technol.*, **22**, 3–17, doi:10.1175/JTECH-1681.1.
- Davis, A., A. Marshak, W. Wiscombe, and R. Cahalan, 1996: Scale invariance of liquid water distributions in marine stratocumulus. Part I: Spectral properties and stationarity issues. *J. Atmos. Sci.*, **53**, 1538–1558, doi:10.1175/1520-0469(1996)053<1538:SIOLWD>2.0.CO;2.
- Deneke, H. M., and R. A. Roebeling, 2010: Downscaling of Meteosat SEVIRI 0.6 and 0.8  $\mu\text{m}$  channel radiances utilizing the high-resolution visible channel. *Atmos. Chem. Phys.*, **10**, 9761–9772, doi:10.5194/acp-10-9761-2010.
- , W. H. Knap, and C. Simmer, 2009: Multiresolution analysis of the temporal variance and correlation of transmittance and reflectance of an atmospheric column. *J. Geophys. Res.*, **114**, D17206, doi:10.1029/2008JD011680.
- Derrien, M., and H. Le Gléau, 2005: MSG/SEVIRI cloud mask and type from SAFNWC. *Int. J. Remote Sens.*, **26**, 4707–4732, doi:10.1080/01431160500166128.
- Dipankar, A., B. Stevens, R. Heinze, C. Moseley, G. Zängl, M. Giorgetta, and S. Brdar, 2015: Large eddy simulation using the general circulation model ICON. *J. Adv. Model. Earth Syst.*, **7**, 963–986, doi:10.1002/2015MS000431.

- Dorrestijn, J., D. T. Crommelin, A. P. Siebesma, and H. J. J. Jonker, 2013: Stochastic parameterization of shallow cumulus convection estimated from high-resolution model data. *Theor. Comput. Fluid Dyn.*, **27**, 133–148, doi:[10.1007/s00162-012-0281-y](https://doi.org/10.1007/s00162-012-0281-y).
- Feijt, A., and H. Jonker, 2000: Comparison of scaling parameters from spatial and temporal distributions of cloud properties. *J. Geophys. Res.*, **105**, 29 089–29 097, doi:[10.1029/2000JD900414](https://doi.org/10.1029/2000JD900414).
- García-Pereda, J., 2013: High resolution winds (HRW—PGE09 v4.0). Algorithm Theoretical Basis Doc. SAF/NWC/CDOP/INM/SCI/ATBD/09, 78 pp. [Available online at [http://www.nwscf.org/HTMLContributions/SUM/SAF-NWC-CDOP2-INM-SCI-ATBD-09\\_v4.0.pdf](http://www.nwscf.org/HTMLContributions/SUM/SAF-NWC-CDOP2-INM-SCI-ATBD-09_v4.0.pdf).]
- Hammer, A., D. Heinemann, E. Lorenz, and B. Lückehe, 1999: Short-term forecasting of solar radiation: A statistical approach using satellite data. *Sol. Energy*, **67**, 139–150, doi:[10.1016/S0038-092X\(00\)00038-4](https://doi.org/10.1016/S0038-092X(00)00038-4).
- Han, Q., W. B. Rossow, and A. A. Lacis, 1994: Near-global survey of effective droplet radii in liquid water clouds using ISCCP data. *J. Climate*, **7**, 465–497, doi:[10.1175/1520-0442\(1994\)007<0465:NGSOED>2.0.CO;2](https://doi.org/10.1175/1520-0442(1994)007<0465:NGSOED>2.0.CO;2).
- Horvath, A., C. Seethala, and H. Deneke, 2014: View angle dependence of MODIS liquid water path retrievals in warm oceanic clouds. *J. Geophys. Res.*, **119**, 8304–8328, doi:[10.1002/2013JD021355](https://doi.org/10.1002/2013JD021355).
- Jonkheid, B. J., R. A. Roebeling, and E. van Meijgaard, 2012: A fast SEVIRI simulator for quantifying retrieval uncertainties in the CM SAF cloud physical property algorithm. *Atmos. Chem. Phys.*, **12**, 10 957–10 969, doi:[10.5194/acp-12-10957-2012](https://doi.org/10.5194/acp-12-10957-2012).
- Koren, I., L. Oreopoulos, G. Feingold, L. A. Remer, and O. Altartaz, 2008: How small is a small cloud? *Atmos. Chem. Phys.*, **8**, 3855–3864, doi:[10.5194/acp-8-3855-2008](https://doi.org/10.5194/acp-8-3855-2008).
- Lenderink, G., and Coauthors, 2004: The diurnal cycle of shallow cumulus clouds over land: A single-column model intercomparison study. *Quart. J. Roy. Meteor. Soc.*, **130**, 3339–3364, doi:[10.1256/qj.03.122](https://doi.org/10.1256/qj.03.122).
- Lensky, I. M., and D. Rosenfeld, 2008: Clouds-Aerosols-Precipitation Satellite Analysis Tool (CAPSAT). *Atmos. Chem. Phys.*, **8**, 6739–6753, doi:[10.5194/acp-8-6739-2008](https://doi.org/10.5194/acp-8-6739-2008).
- Marshak, A., S. Platnick, T. Várnai, G. Wen, and R. F. Cahalan, 2006: Impact of three-dimensional radiative effects on satellite retrievals of cloud droplet sizes. *J. Geophys. Res.*, **111**, D09207, doi:[10.1029/2005JD006686](https://doi.org/10.1029/2005JD006686).
- Mecikalski, J. R., M. Koenig, and C. P. Jewett, 2013: Application of high-resolution visible sharpening of partly cloudy pixels in Meteosat Second Generation infrared imagery. *Atmos. Res.*, **134**, 1–11, doi:[10.1016/j.atmosres.2013.07.014](https://doi.org/10.1016/j.atmosres.2013.07.014).
- Nakajima, T., and M. D. King, 1990: Determination of the optical thickness and effective particle radius of clouds from reflected solar radiation measurements. Part I: Theory. *J. Atmos. Sci.*, **47**, 1878–1893, doi:[10.1175/1520-0469\(1990\)047<1878:DOTOTA>2.0.CO;2](https://doi.org/10.1175/1520-0469(1990)047<1878:DOTOTA>2.0.CO;2).
- Nicholls, S., and J. Leighton, 1986: An observational study of the structure of stratiform cloud sheets: Part I. Structure. *Quart. J. Roy. Meteor. Soc.*, **112**, 431–460, doi:[10.1002/qj.49711247209](https://doi.org/10.1002/qj.49711247209).
- Quaas, J., O. Boucher, and U. Lohmann, 2006: Constraining the total aerosol indirect effect in the LMDZ and ECHAM4 GCMs using MODIS satellite data. *Atmos. Chem. Phys.*, **6**, 947–955, doi:[10.5194/acp-6-947-2006](https://doi.org/10.5194/acp-6-947-2006).
- Roebeling, R. A., A. J. Feijt, and P. Stammes, 2006: Cloud property retrievals for climate monitoring: Implications of differences between Spinning Enhanced Visible and Infrared Imager (SEVIRI) on *Meteosat-8* and Advanced Very High Resolution Radiometer (AVHRR) on *NOAA-17*. *J. Geophys. Res.*, **111**, D20210, doi:[10.1029/2005JD006990](https://doi.org/10.1029/2005JD006990).
- , H. M. Deneke, and A. J. Feijt, 2008: Validation of cloud liquid water path retrievals from SEVIRI using one year of CloudNET observations. *J. Appl. Meteor. Climatol.*, **47**, 206–222, doi:[10.1175/2007JAMC1661.1](https://doi.org/10.1175/2007JAMC1661.1).
- Rossow, W. B., and L. C. Garder, 1993: Cloud detection using satellite measurements of infrared and visible radiances for ISCCP. *J. Climate*, **6**, 2341–2369, doi:[10.1175/1520-0442\(1993\)006<2341:CDUSMO>2.0.CO;2](https://doi.org/10.1175/1520-0442(1993)006<2341:CDUSMO>2.0.CO;2).
- Schmetz, J., P. Pili, S. Tjemkes, D. Just, J. Kerkmann, S. Rota, and A. Ratier, 2002: An introduction to Meteosat Second Generation (MSG). *Bull. Amer. Meteor. Soc.*, **83**, 977–992, doi:[10.1175/1520-0477\(2002\)083<0977:AITMSG>2.3.CO;2](https://doi.org/10.1175/1520-0477(2002)083<0977:AITMSG>2.3.CO;2).
- Schulz, J., and Coauthors, 2009: Operational climate monitoring from space: the EUMETSAT Satellite Application Facility on Climate Monitoring (CM-SAF). *Atmos. Chem. Phys.*, **9**, 1687–1709, doi:[10.5194/acp-9-1687-2009](https://doi.org/10.5194/acp-9-1687-2009).
- Senf, F., F. Dietzsch, A. Hünnerbein, and H. Deneke, 2015: Characterization of initiation and growth of selected severe convective storms over central Europe with MSG-SEVIRI. *J. Appl. Meteor. Climatol.*, **54**, 207–224, doi:[10.1175/JAMC-D-14-0144.1](https://doi.org/10.1175/JAMC-D-14-0144.1).
- Slobodda, J., A. Hünnerbein, R. Lindstrot, R. Preusker, K. Ebell, and J. Fischer, 2015: Multichannel analysis of correlation length of SEVIRI images around ground-based cloud observatories to determine their representativeness. *Atmos. Meas. Tech.*, **8**, 567–578, doi:[10.5194/amt-8-567-2015](https://doi.org/10.5194/amt-8-567-2015).
- Stuhlmann, R., A. Rodriguez, S. Tjemkes, J. Grandell, A. Arriaga, J.-L. Bézy, D. Aminou, and P. Bensi, 2005: Plans for EUMETSAT's Third Generation Meteosat geostationary satellite programme. *Adv. Space Res.*, **36**, 975–981, doi:[10.1016/j.asr.2005.03.091](https://doi.org/10.1016/j.asr.2005.03.091).
- Trenberth, K. E., J. T. Fasullo, and J. Kiehl, 2009: Earth's global energy budget. *Bull. Amer. Meteor. Soc.*, **90**, 311–323, doi:[10.1175/2008BAMS2634.1](https://doi.org/10.1175/2008BAMS2634.1).
- Turner, D. D., and Coauthors, 2007: Thin liquid water clouds: Their importance and our challenge. *Bull. Amer. Meteor. Soc.*, **88**, 177–190, doi:[10.1175/BAMS-88-2-177](https://doi.org/10.1175/BAMS-88-2-177).
- Von Storch, H., and F. W. Zwiers, 2002: *Statistical Analysis in Climate Research*. Cambridge University Press, 496 pp.
- Wolters, E. L. A., H. M. Deneke, B. J. J. M. van den Hurk, J. F. Meirink, and R. A. Roebeling, 2010: Broken and inhomogeneous cloud impact on satellite cloud particle effective radius and cloud-phase retrievals. *J. Geophys. Res.*, **115**, D10214, doi:[10.1029/2009JD012205](https://doi.org/10.1029/2009JD012205).
- Wood, R., and D. L. Hartmann, 2006: Spatial variability of liquid water path in marine low cloud: The importance of mesoscale cellular convection. *J. Climate*, **19**, 1748–1764, doi:[10.1175/JCLI3702.1](https://doi.org/10.1175/JCLI3702.1).
- Zinner, T., and B. Mayer, 2006: Remote sensing of stratocumulus clouds: Uncertainties and biases due to inhomogeneity. *J. Geophys. Res.*, **111**, D14209, doi:[10.1029/2005JD006955](https://doi.org/10.1029/2005JD006955).
- , H. Mannstein, and A. Taffer, 2008: Cb-TRAM: Tracking and monitoring severe convection from onset over rapid development to mature phase using multi-channel *Meteosat-8* SEVIRI data. *Meteor. Atmos. Phys.*, **101**, 191–210, doi:[10.1007/s00703-008-0290-y](https://doi.org/10.1007/s00703-008-0290-y).

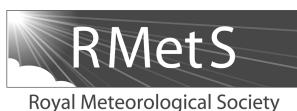
---

### **4.3 Third publication: Metrics for the evaluation of warm convective cloud fields in a large eddy simulation with Meteosat images**

The content of this chapter has already been published in the manuscript “Metrics for the evaluation of warm convective cloud fields in a large eddy simulation with Meteosat images” by Sebastian Bley, Hartwig Deneke, Fabian Senf and Leonhard Scheck in the journal “Quarterly Journal of the Royal Meteorological Society” in 2017 with the doi: 10.1002/qj.3067.

Reprinted with permission by the authors from Journal of Quarterly Journal of the Royal Meteorological Society. 2017, 143, 2050–2060.

Copyright 2017 by the authors. Quarterly Journal of the Royal Meteorological Society published by John Wiley & Sons Ltd on behalf of the Royal Meteorological Society. This is an open access article under the terms of the Creative Commons Attribution License, which permits use, distribution and reproduction in any medium, provided the original work is properly cited.



## Metrics for the evaluation of warm convective cloud fields in a large-eddy simulation with Meteosat images

Sebastian Bley,<sup>a\*</sup> Hartwig Deneke,<sup>a</sup> Fabian Senf<sup>a</sup> and Leonhard Scheck<sup>b</sup>

<sup>a</sup>Leibniz Institute for Tropospheric Research, Leipzig, Germany

<sup>b</sup>Meteorological Institute Munich, Ludwig-Maximilian University of Munich, Germany

\*Correspondence to: S. Bley, TROPOS, Permoserstrasse 15, 04318 Leipzig, Germany.  
E-mail: sebastian.bley@tropos.de

The representation of warm convective clouds in atmospheric models and satellite observations can considerably deviate from each other partly due to different spatial resolutions. This study aims to establish appropriate metrics to evaluate high-resolution simulations of convective clouds by the ICON Large-Eddy Model (ICON-LEM) with observations from Meteosat SEVIRI over Germany. The time series and frequency distributions of convective cloud fraction and liquid water path (LWP) are analyzed. Furthermore, the study focuses on size distributions and decorrelation scales of warm convective cloud fields. The investigated metrics possess a pronounced sensitivity to the apparent spatial resolution. At the fine spatial scale, the simulations show higher occurrence frequencies of large LWP values and a factor of two to four smaller convective cloud fractions. Coarse-graining of simulated fields to the optical resolution of Meteosat essentially removes the differences between the observed and simulated metrics. The distribution of simulated cloud sizes compares well with the observations and can be represented by a power law, with a moderate resolution sensitivity. A lower limit of cloud sizes is identified, which is 8–10 times the native grid resolution of the model. This likely marks the effective model resolution beyond which the scaling behaviour of considered metrics is not reliable, implying that a further increase in spatial resolution would be desirable to better resolve cloud processes below 1 km. It is finally shown that ICON-LEM is consistent with spatio-temporal decorrelation scales observed with Meteosat having values of 30 min and 7 km, if transferred to the true optical satellite resolution. However, the simulated Lagrangian decorrelation times drop to 10 min at 1 km resolution, a scale covered by the upcoming generation of geostationary satellites.

**Key Words:** warm convective cloud fields; model evaluation; geostationary satellite remote sensing; cloud field metrics; resolution sensitivity; large-eddy simulation

Received 12 December 2016; Revised 10 March 2017; Accepted 3 May 2017; Published online in Wiley Online Library

### 1. Introduction

The realistic representation of clouds in general circulation models (GCMs) in general, and convective clouds in particular, remains a fundamental challenge of climate research (Bony *et al.*, 2015). This difficulty arises in part from the coarse horizontal resolution ( $\sim 100$  km) of GCMs, which does not allow one to resolve individual clouds nor the underlying turbulent, microphysical and convective processes. Instead, subgrid-scale processes below the model resolution have to be parametrized. To evaluate and improve these parametrizations, and to advance our understanding of the effects of such small-scale processes, the characterization of the spatio-temporal characteristics of

convective clouds across all relevant scales based on observations and high-resolution models is essential. Towards this goal, suitable metrics for comparing observations and model results are required, and their sensitivity to the spatial resolution of the underlying data needs to be quantified.

Weisman *et al.* (1997) reported a strong sensitivity of the temporal evolution of convective cloud systems to the grid resolution of the atmospheric model. They also demonstrated that a resolution below 1 km is necessary to resolve the cellular structure of cumulus clouds. The cloud size distribution and the morphology of simulated clouds has also been found to be sensitive to the horizontal resolution (Nagasawa *et al.*, 2006). Brown (1999) showed that the cloud size distribution is clearly



shifted towards smaller clouds if the grid resolution of their large-eddy simulation (LES) model is increased up to 20 m. They also found that the higher frequency of smaller clouds is compensated by a reduction of larger clouds, resulting in no significant change of the total cloud fraction (CF). In contrast, Neggers *et al.* (2003) demonstrated that the sizes of the dominating clouds are robust in their LES model considering a horizontal grid spacing from 25 to 100 m. Heus and Seifert (2013) tracked shallow cumulus clouds in a LES with 25 m grid resolution covering a relatively large domain, and investigated the resulting cloud size distributions. Applying different liquid water path (LWP) thresholds for cloud masking, a power law dependency was observed, with exponents ranging from  $-2.2$  to  $-2.9$ . Moreover, they found the cloud size distributions for different resolution set-ups start to converge if only clouds larger than the effective model resolution are considered. The latter was assumed to be six times the grid resolution in their study. Dorrestijn *et al.* (2012) pointed out that a spatial resolution of at least 100 m is required to realistically resolve convective dynamics of small-scale clouds in numerical models. At the same time, large-domain calculations are needed to obtain meaningful cloud statistics (Stevens *et al.*, 2002). Based on 30 m resolution Landsat observations, Koren *et al.* (2008) showed that, as the spatial resolution of the satellite sensor decreases, an increasing fraction of small clouds are missed. Cloudy pixels also increasingly contain significant clear-sky contributions from the cloud-free surface. Overall, the CF was found to be strongly overestimated due to the resolution sensitivity. The described effects will result in significant and resolution-dependent uncertainties in derived cloud properties, and highlight the sensitivity of satellite products to sensor resolution.

Due to the increasing capacity of supercomputers, large-domain simulations at a cloud-resolving scale are becoming feasible, and show, for example, a better timing of the diurnal cycle of convection (Hohenegger *et al.*, 2008). Within the High Definition Clouds and Precipitation for Climate Prediction (HD(CP)<sup>2</sup>) project, a number of LESs were conducted with the ICOSahedral Non-hydrostatic (ICON) atmospheric model (Dipankar *et al.*, 2015) covering a large domain over Germany. These ICON-LEM runs were carried out on a 156 m grid, and thus partially resolve turbulence and large eddies, and allow study of their influence on shallow cumulus convection. A comprehensive evaluation of the ability of ICON simulations to reproduce the general thermodynamic and cloud-precipitation characteristics was performed by Heinze *et al.* (2016). This resulted in the overall agreement that high-resolution ICON-LEM simulations enable an improved understanding of cloud and precipitation processes, and can serve as reference for the development of novel cloud parametrizations in GCMs. Our study extends the efforts of Heinze *et al.* (2016) and assesses the representation of warm convective cloud fields including their spatio-temporal variability in more detail.

One challenge for the evaluation of high-resolution and large-domain simulations is the lack of suitable reference observations. Polar-orbiting satellite instruments like MODIS provide global datasets with high spatial resolution ( $\sim 250$ – $1000$  m), but do not allow to evaluate the temporal evolution of convective cloud fields. In contrast, the geostationary Meteosat satellites observe Central Europe with a 5 min repeat cycle, but only at a nadir resolution of  $\sim 3$  km, which is relatively coarse in comparison to the typical size of warm convective clouds. Nevertheless, Meteosat offers the unique opportunity to characterize both the spatial and the temporal variability of small-scale convective cloud fields, and to use these characteristics for model evaluation. Towards this goal, Bley *et al.* (2016) introduced metrics to characterize the spatio-temporal evolution of convective cloud fields. Considering the fields of the retrieved liquid water path, a characteristic decorrelation time-scale of 30 min in a Lagrangian reference frame, and a decorrelation length-scale of 7 km was identified. However, these scales are only valid at the coarse horizontal resolution of Meteosat ( $\sim 3.1 \times 6$  km<sup>2</sup>), and a decrease of the

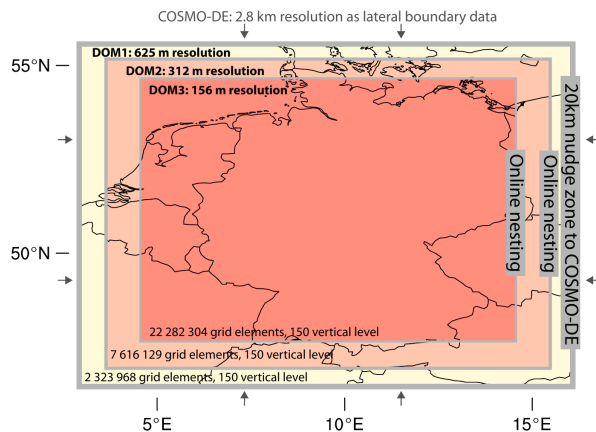


**Figure 1.** ICON-LEM domain and its two nests with grid refinement. The open lateral boundaries are relaxed towards the COSMO-DE analysis (Heinze *et al.*, 2016). [Colour figure can be viewed at [wileyonlinelibrary.com](http://wileyonlinelibrary.com)].

decorrelation time when considering the high-resolution visible (HRV) channel with  $1.2 \times 2.1$  km<sup>2</sup> horizontal resolution was also observed. This suggests a strong resolution dependency of the decorrelation scales on spatial resolution. Typical lifetimes of cumulus clouds simulated by LES lie between 20 and 40 min, but small clouds dissipate much faster after a few minutes (Jiang *et al.*, 2006).

The central goal of the present study is to establish appropriate metrics to evaluate the representation of convective cloud fields in ICON-LEM with observations from the Spinning Enhanced Visible and Infrared Imager (SEVIRI) on board Meteosat, and to investigate the effects of model and sensor resolution. The main research questions can be summarized as:

- (i) Does ICON-LEM realistically simulate the CF frequency distribution of LWP, as well as the horizontal structure and temporal evolution of convective cloud fields?
- (ii) How sensitive is the comparison of satellite observations and model results to the spatial resolution of the satellite instrument and model grid?
- (iii) Can we understand some limitations of the Meteosat observations using the much higher-resolved ICON-LEM results?

For this study, ICON-LEM simulations are carried out with three horizontal grid resolutions of 156, 312 and 625 m. This allows us to analyze differences in the cloud fields arising from different model resolutions, and to separate model-inherent resolution effects from those resulting from a coarse-graining of the model outputs.

The ICON-LEM, COSMO-DE and Meteosat data used in this study are briefly described in section 2. Results are presented and discussed in section 3. The main conclusions and an outlook are given in section 4.

## 2. Data and methods

### 2.1. Simulations

The ICON-LEM model is based on the unified modelling system for climate and numerical weather forecast ICON (ICOSahedral Non-hydrostatic), which has been extended to a LES that partially resolves turbulence and convection within the HD(CP)<sup>2</sup> project. For the unresolved scales, a new three-dimensional turbulence scheme based on the classical Smagorinsky scheme has been implemented on a triangular grid (Dipankar *et al.*, 2015).

Within the project, four ICON-LEM runs have been performed for 24–26 April and 2 May 2013 with a very high spatial resolution of 156 m over a large domain covering Germany (Figure 1). The four simulated days comprise a range of typical weather conditions

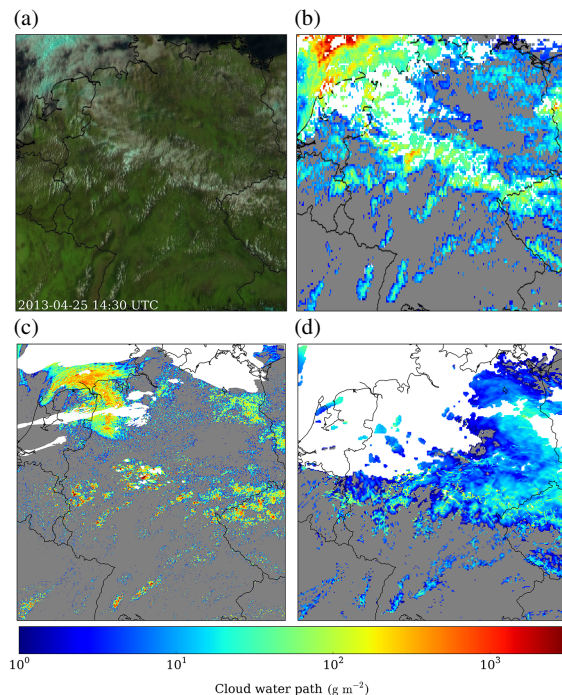


**Figure 2.** Case-study over the HD(CP)<sup>2</sup> domain on 25 April 2013 at 1430 UTC with (a) the high-resolution natural colour RGB image from Meteosat  $\mathcal{O}(1 \times 2 \text{ km}^2)$ , (b) the cloud liquid water path (LWP) retrieved from Meteosat  $\mathcal{O}(4 \times 6 \text{ km}^2)$ , (c) simulated by ICON-LEM  $\mathcal{O}(156 \text{ m})$  and (d) simulated by COSMO-DE  $\mathcal{O}(2.8 \text{ km})$ . The cyan colours identify high cirrus clouds and deep convective cloud systems that contain ice particles, attributable to the strong absorption in the near infrared  $1.6 \mu\text{m}$  channel. All frozen cloud fraction is visually filtered out by the white mask in (b)–(d). [Colour figure can be viewed at [wileyonlinelibrary.com](http://wileyonlinelibrary.com)].

for Germany and the spring season. One-way nesting of ICON-LEM simulations is performed with grid refinement steps ranging from 624 to 312 m and 156 m in the innermost domain. As the grid spacings of the ICON-LEM runs are somewhat higher than those used typically in LES models for cloud studies, these runs could also be classified as ‘near-LES’ experiments (Mechem *et al.*, 2012).

ICON-LEM is used in a real-case configuration with prescribed lateral boundary conditions and a nesting approach (Heinze *et al.*, 2016). ICON-LEM is not run in a semi-idealized set-up like most other LES models, but uses the realistic land surface model TERRA which is also used in COSMO-DE (Heinze *et al.*, 2016). Each simulation day is initialized at 0000 UTC from the operational COSMO-DE analysis and runs for 24 h. The two-moment mixed-phase bulk microphysical parametrization of Seifert and Beheng (2005) is applied.

Apart from the great challenge to carry out such high-performance simulations at the German Supercomputing Centre (DKRZ), massive storage capacities are also needed to write the model output to disk (Heinze *et al.*, 2016). Data output of 50 terabytes was generated for one day of simulation. The three-dimensional model variables were mapped to a regular grid with 1 km grid spacing and written out every hour. Variables on the unstructured high-resolution model grid were written to files only once or twice a day during MODIS overpasses. The two-dimensional data output for the cloud properties is archived at 156, 312 and 625 m grid spacing and a 1 s time frequency, albeit sub-sampled to 1 min time steps for the present study to reduce the computing time for the analysis. Simulations from all three nests are compared. To avoid precipitation and glaciation effects that could influence the evolution of total cloud water, only the LWP is considered. Furthermore, to increase comparability to the satellite observations, we removed all columns of LWP that contain less than  $1 \text{ g m}^{-2}$  to reflect the sensitivity limit of the satellite sensors.

For comparison, COSMO-DE simulations have been carried out based on the operational set-up with 2.8 km horizontal grid resolution, but with the two-moment microphysical scheme also used in ICON-LEM (Seifert and Beheng, 2005). The initial and boundary conditions are prescribed by COSMO-EU on 7 km horizontal resolution. The COSMO-DE output has a 15 min temporal resolution, and contains the atmospheric pressure, temperature, water vapour mixing ratio and liquid water mixing ratio, which are used for calculation of the LWP. The liquid water mixing ratio already includes the subgrid-scale cloud information as used in the radiation scheme.

The performance of ICON-LEM in terms of boundary-layer variables, clouds and precipitation has already been evaluated by Heinze *et al.* (2016) using a comprehensive database including *in situ* and remote-sensing observations as well as reference model data from the COSMO-DE model. The key results of their study can be summarized as follows. COSMO-DE and ICON-LEM show a similar good performance with respect to cloud distributions and the large-scale situation, as both models are forced with nearly identical initial and boundary conditions. In ICON-LEM, shallow cumulus clouds are simulated as too large, which is likely attributable to the effective model resolution. Applying the ICON-LEM output to forward simulations relying on the look-up table-based Method for Fast Satellite Image Synthesis (MFASIS; Scheck *et al.*, 2016) shows similar cloud size distributions to the observations for cloud sizes between 1 and 100 km. Heinze *et al.* (2016) also show substantial improvements in the variability of the ICON-LEM LWP in  $25 \times 25 \text{ km}^2$  grid boxes compared to COSMO-DE.

## 2.2. Observations

Satellite data are taken from SEVIRI, which is the main payload on board the geostationary Meteosat Second Generation (MSG) satellites operated by EUMETSAT. The LWP is calculated using the Cloud Physical Properties retrieval (CPP; Roebeling *et al.*, 2006) developed in the framework of the Satellite Application Facility on Climate Monitoring (CM SAF; Schulz *et al.*, 2009). The lower part of the LWP distribution might be under-represented by MSG due to its detection limit, which mainly affects thin cirrus clouds and low small cumulus clouds. These highly variable clouds cause large uncertainties in the MSG retrieval of cloud optical thickness ( $\tau$ ) and droplet effective radius ( $r_e$ ), and further lead to an underestimation of the LWP due to the plane-parallel albedo bias. Geostationary satellite retrievals generally underestimate the LWP especially for broken cumulus clouds (e.g. Marshak *et al.*, 2006; Wolters *et al.*, 2010). This effect also depends on the viewing geometry (Horvath *et al.*, 2014), and causes LWP uncertainties that influence the spatio-temporal characteristics of convective cloud fields. In the following, all ice-containing clouds have been identified with a cloud phase flag and filtered out. This has been done to emphasize the focus on liquid water clouds of the present study. However it should be noted that cloud phase determination from satellite is also subject to some uncertainties. The standard nadir sampling resolution of SEVIRI is  $\sim 3 \times 3 \text{ km}^2$  with a 5 min repeat cycle in the rapid scan mode. However, the horizontal resolution decreases for an increasing distance from the Equator due to the viewing geometry, having a pixel area of about  $\sim 3.1 \times 6 \text{ km}^2$  in the centre of our domain. The real optical resolution of MSG is lower as characterized by the modulation transfer function (MTF) and the pixels are oversampled in the image rectification process by a factor of about 1.6 (Deneke and Roebeling, 2010). Thus the effective area of a pixel is slightly larger than the actual sampling resolution.

## 2.3. Scene selection

From the simulated ICON-LEM days, we selected two types of scene. First, domain-scale cloud scenes from one particular



day, 25 April 2013, were selected for the investigation of LWP frequency distribution (FD) and time series (TS) as well as the distribution of cloud sizes. For this day, Figure 2 shows the modelled and satellite-retrieved fields of LWP at 1430 UTC. To provide an overview of the synoptic situation and the thermodynamic phase of clouds, the satellite observations are shown as day natural colour red-green-blue (RGB) composite (Lensky and Rosenfeld, 2008). We eliminate the effect of larger-scale cloud fields that are advected into the model domain from the northwest by only considering the lower half of the domain for the calculation of FD and TS. Furthermore, cloud cover that touches the evaluation domain borders has been removed.

Second, we consider local-scale cloud scenes of a size of around  $62 \times 62 \text{ km}^2$  from all four simulated days. Corresponding boxes have a size of  $400 \times 400$  ( $24 \times 24$ ) grid cells for ICON-LEM (COSMO-DE) simulations and are centred around developing warm convective cloud fields. This box size has been chosen to ensure preferably homogeneous advection conditions for an accurate tracking and to comprise a sufficient number of warm convective clouds at the same time to obtain robust cloud field statistics. However, the cloud cases have been subjectively selected, imposing an upper limit on cloud fraction of 0.4 and 0.8 for ICON-LEM and COSMO-DE fields, respectively. A set of ten cloud cases is identified and tracked forward in time. A Fast Fourier Transform is used to calculate the spatial phase shift, determined by the maximum correlation (Anuta, 1970). This phase shift is finally transformed into a pixel shift for each of the 1 min time steps. For the local-scale cloud scenes, relations between average cloud aspect ratio and viewing angle dependence as well as the effects of resolution on spatio-temporal decorrelation scales are investigated on this data basis.

We do not expect ICON-LEM and COSMO-DE to perfectly match the MSG observations for small-scale convective clouds with respect to time and location. Rather we aim to compare the general statistics of simulated spatio-temporal decorrelation scales with the observational results obtained between April and July 2013 in our earlier study (Bley *et al.*, 2016).

#### 2.4. Spatial resolution

The spatial resolution is a fundamental characteristic of atmospheric models and satellite instruments, which can influence not only the cloud properties but also the whole cloud field statistics, such as the distribution of cloud sizes and CF (Koren *et al.*, 2008). Particularly for the characterization of warm convective cloud fields, the spatial resolution needs to be considered carefully.

We emphasize that there can be an inherent difference between the resolution at which the data are provided, called the native resolution here, and the optical or effective resolution, for satellite observations and model simulations, respectively. For Meteosat observations, the optical resolution is lower than the native resolution, by a factor of 1.6 (section 2.2 gives details). For numerical simulations, the effective resolution is always coarser than the native grid resolution and represents a range at which the variability of physical processes can be resolved. With the term 'native resolution' we are assigning the grid spacing of the model data and the original pixel size of the satellite data in the present study. For the comparison of data at very different native resolutions, a third type of resolution, the coarsened-resolution comes into play which is used to convert the higher-resolved data into their lower-resolved counterpart. The ICON-LEM model has three different native grid resolutions, which are abbreviated by  $\mathcal{O}(156 \text{ m})$ ,  $\mathcal{O}(312 \text{ m})$  and  $\mathcal{O}(625 \text{ m})$  in the present study. The COSMO-DE model has a spatial resolution of  $\mathcal{O}(2.8 \text{ km})$  and the Meteosat native pixel resolution is  $\mathcal{O}(3.6 \times 6 \text{ km}^2)$  for the narrowband channels and  $\mathcal{O}(1.2 \times 2 \text{ km}^2)$  for the HRV channel. As stated above, the optical resolution of Meteosat is a factor 1.6 larger than the native pixel

resolution. Hence, for comparison of ICON-LEM and Meteosat warm convective cloud fields, a coarse-graining of ICON-LEM cloud fields to 7 km average pixel size is performed, although ignoring the anisotropy in the observation grid.

The coarse-graining is performed sequentially. The original field is divided into small subdomains of  $2 \times 2$  size for which the average is calculated and retained. After the first coarse-graining step, the resulting field has smaller pixel size by a factor of four.  $\sigma$  represents the number of coarse-graining iterations. The ICON-LEM cloud fields are gradually coarse-grained to  $156 \times 2^\sigma \text{ m}$  until 7000 m spatial resolution is reached. COSMO-DE is coarse-grained to 5.6 km resolution. For the coarse-grained cloud fields, to avoid confusion over the origin of these cloud fields, the following notation is introduced:  $\mathcal{C}(\text{native resolution} \rightarrow \text{coarse-grained resolution})$ .

### 3. Metrics

In this section, results from the investigated metrics are presented and discussed. As metrics for the evaluation of warm convective clouds in the ICON-LEM model with Meteosat observations and COSMO-DE data, we first consider the frequency distribution and time series of LWP and CF. The effect of the cloud aspect ratio, spatial resolution and viewing geometry is subsequently addressed. In the following, the frequency distribution of cloud sizes is analyzed for the native resolution and coarse-grained to the optical resolution of Meteosat. The power laws are also compared to the observations. Convective cloud field tracking is finally applied to evaluate the decorrelation time- and length-scales. The model results are related to spatio-temporal characteristics achieved in Bley *et al.* (2016). The main focus of these investigated metrics lies on the spatial resolution sensitivity.

#### 3.1. Frequency distribution of LWP

Figure 3 shows an example LWP distribution for a local-scale cloud field from the ICON-LEM model over southern Germany on 25 April 2013 at 1300 UTC. The image demonstrates how a warm convective cloud field is captured by the optical Meteosat resolution of 7 km (right-hand side). The fine LWP structures that are simulated by ICON-LEM  $\mathcal{O}(156 \text{ m})$ ,  $\mathcal{O}(312 \text{ m})$  and  $\mathcal{O}(625 \text{ m})$  (left-hand side) are completely smoothed down by a coarse-graining to 7 km with a substantial decreasing frequency of high LWP values. Coarse-graining of the LWP fields additionally leads to a strong increase in the CF, because larger clouds grow faster in the coarse-graining than smaller clouds disappear in the gaps (Koren *et al.*, 2008). For the case example in Figure 3, the CF of 0.23 in ICON-LEM  $\mathcal{O}(156 \text{ m})$  is increased to 0.69 when going to ICON-LEM  $\mathcal{C}(156 \text{ m} \rightarrow 7 \text{ km})$ . Also, the spatial decorrelation length ( $\lambda$ ) changes drastically from  $\lambda = 733 \text{ m}$  to  $\lambda = 4531 \text{ m}$ , implying that the cloud sizes are increasing and that a part of the texture information is lost.  $\lambda$  represents a measure of the change of spatial coherence of the horizontal cloud field structure, and indicates how far the box can be still displaced before the LWP structure between the displaced and the initial cloud field is decorrelated (Bley *et al.*, 2016). The resolution sensitivity of CF and  $\lambda$  is discussed in more detail in sections 3.3 and 3.5.

Most of the fine LWP structure from ICON-LEM  $\mathcal{O}(156 \text{ m})$  can be still obtained from ICON-LEM  $\mathcal{C}(156 \text{ m} \rightarrow 1250 \text{ m})$ . However, coarse-graining to 7 km clearly eliminates the original 156 m structure. Every pixel in the 7 km box includes a substantial amount of unresolved sub-pixel variability. Using complementary data from the HRV channel with  $1.2 \times 2 \text{ km}^2$  resolution can help to resolve a part of this variability (Bley *et al.*, 2016).

Figure 3 further indicates a nonlinear relation between the spatial resolution and CF as well as  $\lambda$ . The change in LWP structure, CF and  $\lambda$  is much more pronounced between  $\mathcal{C}(156 \text{ m} \rightarrow 625 \text{ m})$  and  $\mathcal{C}(156 \text{ m} \rightarrow 2500 \text{ m})$  than between  $\mathcal{O}(156 \text{ m})$  and  $\mathcal{C}(156 \text{ m} \rightarrow 625 \text{ m})$ , although the resolution is

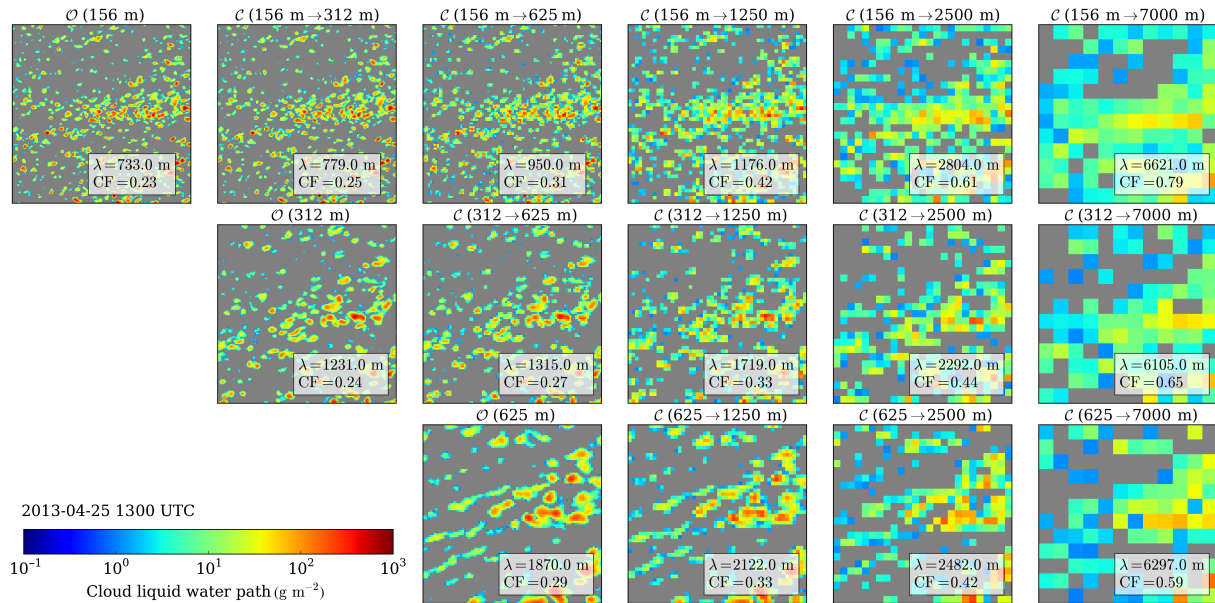


**Figure 3.** Example of a local-scale ICON-LEM  $62 \times 62 \text{ km}^2$  cloud field showing the LWP over Southern Germany on 25 April 2013. The first row shows the native resolution and coarse-grained cloud fields, originated from ICON-LEM  $O(156 \text{ m})$ , the second row from ICON-LEM  $O(312 \text{ m})$  and the third row from  $O(625 \text{ m})$ . The grey background indicates cloud-free areas;  $\lambda$  is the decorrelation length and CF the convective cloud fraction for each cloud field. [Colour figure can be viewed at [wileyonlinelibrary.com](http://wileyonlinelibrary.com)].

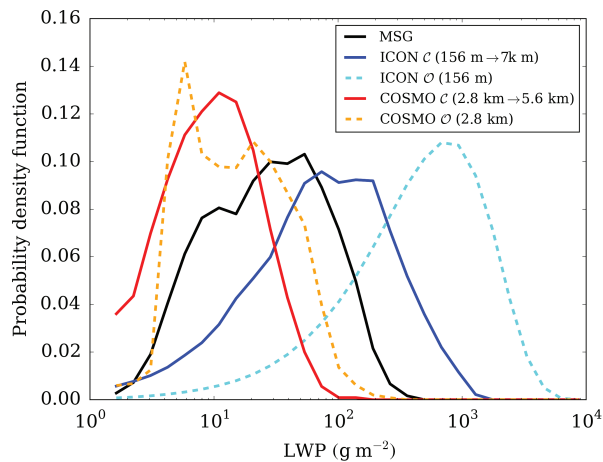


**Figure 4.** Probability density function (PDF) of the domain-scale LWP with warm convective clouds retrieved by MSG (black) and simulated by ICON-LEM  $C(156 \text{ m} \rightarrow 7 \text{ km})$  (blue solid) and COSMO-DE  $C(2.8 \text{ km} \rightarrow 5.6 \text{ km})$  (red solid) on 25 April 2013 between 0900 and 1530 UTC. The dashed lines indicate the ICON-LEM  $O(156 \text{ m})$  and COSMO-DE  $O(2.8 \text{ km})$  functions at their native resolution. [Colour figure can be viewed at [wileyonlinelibrary.com](http://wileyonlinelibrary.com)].

quadrupled in both cases. This is most likely related to the effective resolution of the model and will be discussed in detail in section 3.5

The domain-scale LWP frequency distribution averaged between 0900 and 1530 UTC is presented in Figure 4. ICON-LEM and COSMO-DE are coarse-grained towards Meteosat resolution for a solid comparison. The original ICON-LEM  $O(156 \text{ m})$  and COSMO-DE  $O(2.8 \text{ km})$  data are also shown for a demonstration of the resolution sensitivity.

On the one hand, COSMO-DE at native resolution underestimates the typical range of LWP values compared to the observations – a situation that becomes even worse after coarse-graining to  $C(2.8 \text{ km} \rightarrow 5.6 \text{ km})$ . On the other hand, the high-resolution simulations performed by ICON-LEM achieve LWP values at native resolution that are more than one magnitude

larger. Coarse-graining brings the ICON-LEM LWP values closer to the observations, but still a significant overestimation remains. This might be a real model deficit and be caused by the fact that too much water is accumulated at convection scales of 1 km and more, which would have been distributed over much smaller cloud scales in reality. A comparison of observed and simulated cloud size distributions will be discussed in depth in section 3.4. In general, Figure 4 reveals the strong resolution sensitivity of LWP.

Heinze *et al.* (2016) evaluated the combined liquid and ice cloud water path (CWP) for all days over the full HD(CP)<sup>2</sup> domain and concluded that ICON-LEM simulates clouds better than COSMO-DE in comparison to the satellite-retrieved CWP. The MODIS CWP retrieval was found to agree better with ICON-LEM than the MSG retrieval, which is likely attributable to the higher resolution of the MODIS instrument ( $1 \times 1 \text{ km}^2$ ). While MODIS seems to be a better reference dataset to evaluate small-scale cloud structures in ICON-LEM, only MSG as a geostationary instrument with a high temporal sampling is able to resolve the temporal evolution of warm convective clouds. The temporal development of a warm convective cloud field is analyzed in the next section.

### 3.2. Time series of LWP and CF

Due to the high spatio-temporal LWP inhomogeneity of warm convective clouds, we do not expect a perfect agreement between simulations and observations with respect to time and location of individual cumulus clouds. Therefore, the evaluation of the LWP time series is performed for the domain scale.

Figure 5 shows the time series of the in-cloud averaged LWP, the CF and the area-average LWP, again for the native resolution of MSG, ICON-LEM and COSMO-DE and for COSMO-DE and ICON-LEM also coarse-grained. In contrast to the LWP frequency distribution, the ICON-LEM  $C(156 \text{ m} \rightarrow 7 \text{ km})$  time series is in a much better agreement with MSG than with COSMO-DE  $C(2.8 \text{ km} \rightarrow 5.6 \text{ km})$ . However, the upper quartile range is substantially higher, in both the native and the coarse-grained ICON-LEM distribution, which is also supported by Figure 4. The MSG retrieval indicates an artifact around 1400 UTC which is most likely caused by a particular scattering angle of  $\sim 135^\circ$  around

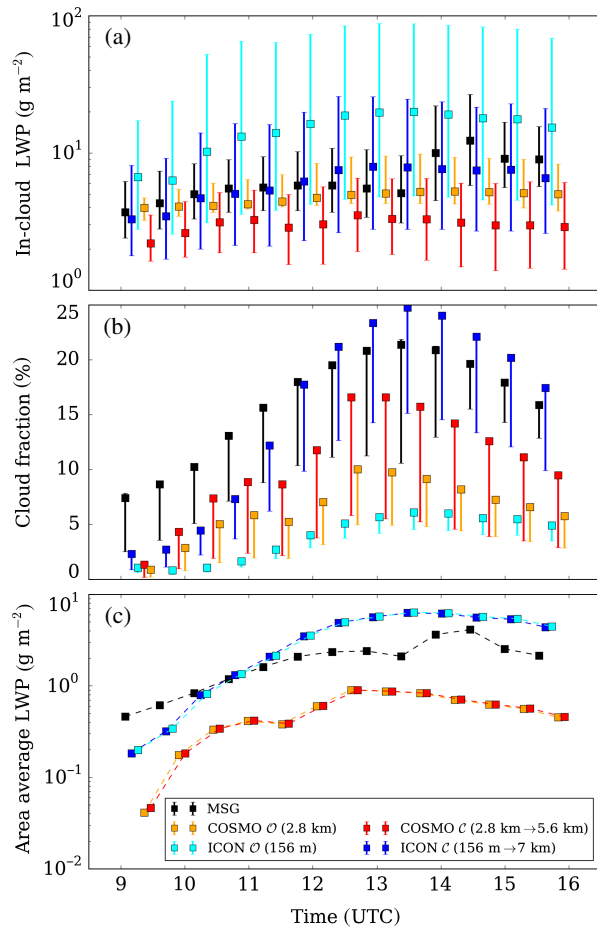


**Figure 5.** Time series of (a) the in-cloud LWP, (b) the CF and (c) the domain-scale average LWP retrieved by MSG (black), and simulated by ICON-LEM  $\mathcal{O}$  (156 m) (cyan), ICON-LEM  $\mathcal{C}$  (156 m  $\rightarrow$  7 km) (blue) and COSMO-DE  $\mathcal{O}$  (2.8 km) (orange) and COSMO-DE  $\mathcal{C}$  (2.8 km  $\rightarrow$  5.6 km) (red). The in-cloud LWP errorbars represent the interquartile range, CF errorbars indicate the sensitivity of the CF on the LWP threshold of  $\text{LWP} > 1 \text{ g m}^{-2}$  (marker) and  $\text{LWP} > 5 \text{ g m}^{-2}$  (lower range). [Colour figure can be viewed at [wileyonlinelibrary.com](#)].

the cloudbow caused by liquid water droplets (Cho *et al.*, 2015). In conclusion, this shows that also the time series of quartile values of the in-cloud LWP is very sensitive to the spatial resolution.

This resolution sensitivity can be perfectly demonstrated with the time series of the CF (Figure 5(b)). Understanding the sensitivities and changes in CF is very important for climate projections, but a reliable comparison between satellite observations and model results of the CF is challenging due to different aspects. Due to the detection sensitivity, MSG basically excludes thin clouds with a LWP lower than  $1 \text{ g m}^{-2}$ . A cloud mask filter is consequently applied to the ICON-LEM, COSMO-DE and MSG cloud fields, defining LWP pixels above  $1 \text{ g m}^{-2}$  as cloudy, otherwise as cloud-free. The CF is also sensitive to the LWP threshold which is applied for the CF in our study. We therefore show the CF for  $\text{LWP} > 1 \text{ g m}^{-2}$  and  $\text{LWP} > 5 \text{ g m}^{-2}$  in the present study.

Figure 5(b) shows that observed convective CF increases from  $\sim 8\%$  in the morning hours to a peak around 20% between 1300 and 1400 UTC. The simulated CFs at native model resolution, which peak at 5% (9%) for ICON-LEM (COSMO-DE), are significantly increased by coarse-graining. COSMO-DE still remains below the observational level whereas ICON-LEM slightly overestimates the peak values in the early afternoon. Both simulations, and especially coarse-grained ICON-LEM, exhibit an overestimation of the diurnal amplitude of convective CF.

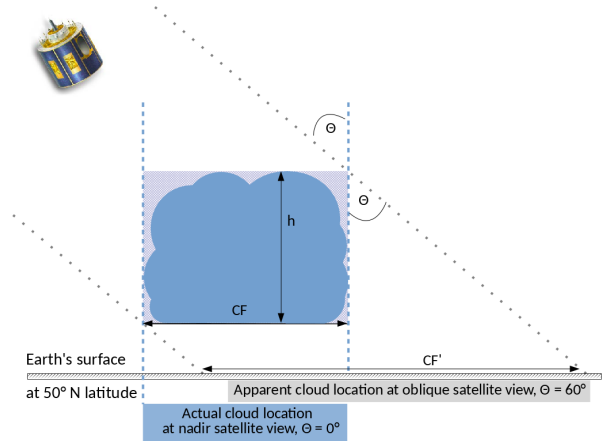


**Figure 6.** Sketch of the projected location of a cloud on the surface, seen from nadir perspective (blue) and from geostationary satellite perspective with a satellite zenith angle of  $60^\circ$  (grey). [Colour figure can be viewed at [wileyonlinelibrary.com](#)].

However, the timing of the CF peaks seems to be in better agreement for ICON-LEM and MSG. In the late afternoon, the simulations and observation display a decreasing CF, which is likely attributable to dissolving clouds or phase transition into ice clouds due to cloud deepening. (Senf *et al.*, 2015).

Figures 5(a) and (b) clearly demonstrate a sensitivity to the spatial resolution, which affects the comparison between observations and models. Figure 5(c) presents the area-averaged LWP, which combines the in-cloud LWP and the CF and gives information about the total liquid water amount within the domain. Now the effect of the spatial resolution is eliminated, only the cloud bow artifact in the MSG retrieval is still apparent. A better agreement is found between ICON-LEM and MSG than for the COSMO-DE LWP which significantly underestimates the total amount of liquid water. From a budget point of view, the efficiency of the liquid water production of water vapour is significantly increased when going from convection-permitting scales of COSMO-DE to very high resolution of ICON-LEM (Baldauf *et al.*, 2011). This increase goes even beyond the observational values leading to an overestimation of simulated convectively generated liquid water.

In conclusion, this analysis demonstrates that higher-resolution simulations are able to reduce biases in liquid cloud properties that show up in the coarser convection-permitting simulations. An overcorrection seems to happen in which the negative bias in convective CF and total liquid water amount changes into a positive bias in the high-resolution runs.

### 3.3. Cloud aspect ratio and viewing geometry

A further important aspect that can influence the CF, but has not been discussed so far in this study, is the cloud aspect ratio, which leads to CF uncertainties due to the slanted viewing geometry of MSG. Due to the position of MSG in the geostationary orbit, observations over Central Europe are performed at high satellite viewing angles between  $45^\circ$  and  $65^\circ$ . This oblique viewing perspective leads to three-dimensional radiative interactions between cloud edges that are not considered in current one-dimensional cloud retrievals (Várnai and Marshak, 2007). That the viewing geometry also influences the CF and causes high uncertainties in data record of the average cloudiness has already been studied by Evan *et al.* (2007).

Figure 6 contrasts the projected location of a cloud over Germany, seen from nadir and from geostationary satellite view under a zenith viewing angle  $\theta$  of  $60^\circ$ . When clouds of a certain height  $h$  are viewed from space by zenith angle  $\theta$  and azimuth angle  $\phi$ , an apparent northward shift  $\Delta y \approx h \tan \theta$ , the



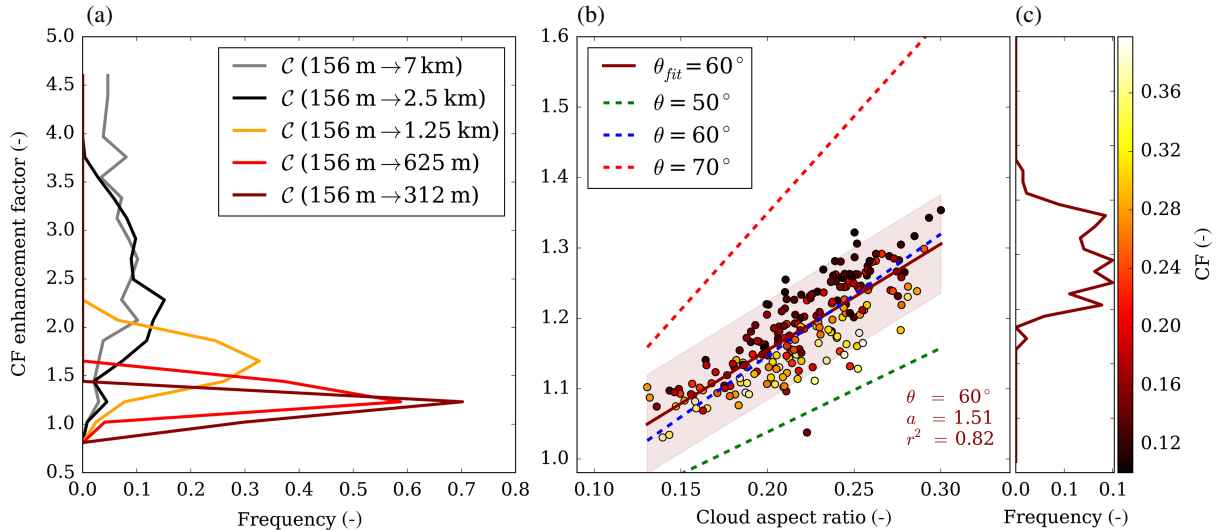


**Figure 7.** (a) Frequency distribution of the CF enhancement factor on a local scale for  $62 \times 62 \text{ km}^2$  ICON-LEM  $\mathcal{O}(156 \text{ m})$  warm convective cloud fields and coarse-grained. (b) CF enhancement factor due to artificial oblique viewing geometry applied to ICON-LEM  $\mathcal{O}(156 \text{ m})$  cloud fields in relation to the cloud aspect ratio for a  $60^\circ$  satellite zenith angle. The solid dark red line indicates the linear regression with slope  $a$  and correlation coefficient  $r^2$ . The dashed lines represent the theoretical curves for varying zenith angle, (c) is the CF enhancement factor frequency for  $60^\circ$ . [Colour figure can be viewed at [wileyonlinelibrary.com](http://wileyonlinelibrary.com)].

so-called parallax shift, happens (e.g. Kostka *et al.*, 2014, gives further discussion). We use this relation and apply an artificial viewing angle to the ICON-LEM cloud fields to imitate a satellite instrument that observes the simulated cloud field from the geostationary orbit. Since the longitude position of the satellite ( $9.5^\circ$ ) lies in our ICON-LEM domain, we furthermore neglect shifts in the longitude direction. From Figure 6, an increased cloud diameter and corresponding cloud area is calculated. The gain in cloud area is given by  $\text{CAR} \tan \theta$ , where the cloud aspect ratio CAR is defined as cloud geometrical thickness divided by the cloud diameter. Furthermore, we account for the overlap of closely located cloud towers.

The enhancement factor of CF is plotted in Figure 7 for the set of local-scale cloud scenes. It represents the change in coarse-grained convective CF relative to the initial CF of the cloud field at  $156 \text{ m}$  spatial resolution. The viewing geometry effect causes CF enhancement factors of  $1.2$ – $1.4$  for the ICON-LEM  $\mathcal{O}(156 \text{ m})$  cloud fields. This effect appears small in comparison to the CF enhancement, supported by Figure 5(b). Figure 7(a) quantifies the increase in the CF for the same convective cloud fields as in Figure 7(b), but as the result of decreasing spatial resolution due to coarse-graining. This CF enhancement already exceeds at  $\mathcal{C}(156 \text{ m} \rightarrow 1250 \text{ m})$  the viewing geometry CF enhancement, which demonstrates that coarse-graining to  $7 \text{ km}$  substantially predominates over the influence of the viewing geometry. One should note that Figure 7(b) is only shown for ICON-LEM  $\mathcal{O}(156 \text{ m})$  and not for any coarser resolution, because coarse-graining is only done in the horizontal direction. This would result in considerably lower aspect ratios, which most likely lead to smaller CF enhancement factors.

One uncertainty, which we cannot account for, is the aspect ratio. The mean aspect ratio for all local-scale cloud scenes is  $0.2$ , ranging from  $0.1$  to  $0.27$ . These values only overlap at the lower end of aspect ratios calculated in (e.g.) Benner and Curry (1998) or Kassianov *et al.* (2005), who found values between  $0.2$  and  $1$ . Therefore, ICON-LEM aspect ratios seem to be slightly too small, which might be caused by numerical diffusion at the scale of the effective resolution. We also suggest that the ratio between vertical and horizontal grid box size might influence the distribution of cloud aspect ratios. Uncertainties in the cloud aspect ratios can cause high uncertainties in the representation of cloud radiation interactions. Han and Ellingson (1999) found a strong influence of the estimated cloud aspect ratios on results

in the long-wave radiation transfer calculations. Furthermore, adiabaticity of convective clouds and hence the liquid water distribution depends on cloud geometrical thickness (Merk *et al.*, 2016). The CF strongly increases for increasing aspect ratios and is even higher for higher zenith angles (Figure 7(b)). The highest CF enhancement appears for low CF between  $0.1$  and  $0.2$ , which is consistent with results from Minnis (1989). The MSG retrieval gives reliable information neither about the cloud thickness nor the cloud-base height. Analysis of data from active satellite sensors can help to better evaluate the aspect ratios, however this goes far beyond our study focus.

In summary, coarse-graining the ICON-LEM cloud fields to MSG resolution dominates the CF enhancement factor in comparison to the viewing angle effect. Although the latter effect seems to be rather weak in the present study, it needs to be carefully considered for deeper convective clouds and long-term global trends of CF from different satellite instruments (Evan *et al.*, 2007).

### 3.4. Cloud size distribution

For evaluation of ICON-LEM cloud size distributions and the investigation of their resolution sensitivity, a binary cloud mask is generated by applying a  $1 \text{ g m}^{-2}$  threshold to the domain-scale LWP fields. From this cloud mask, connected cloud regions are labelled using a connectivity clustering method. For each cloud object, an area-equivalent diameter is calculated. The relative occurrence frequencies of the number of cloud objects within a certain size range are divided by the domain area which results in the unit  $\text{km}^{-3}$ . Note that the normalization of the resulting density functions was performed with respect to equidistant size ranges to be comparable with the studies of Heus and Seifert (2013) and Heinze *et al.* (2016), even though we present our cloud size distributions in log space.

Figure 8 shows the frequency distribution  $n(L)$  of clouds with a given cloud size  $L$ . Different studies show that a power law is the most appropriate way to fit the horizontal cloud size distribution (Benner and Curry, 1998; Zhao and Di Girolamo, 2007; Wood and Field, 2011). We calculate the power law exponent as the slope of the least squares fit to the data in logarithmic space.

The frequency distribution of cloud sizes is well represented by a power law with exponent  $\beta$  ranging from  $-2.3$  to  $-3.2$ .

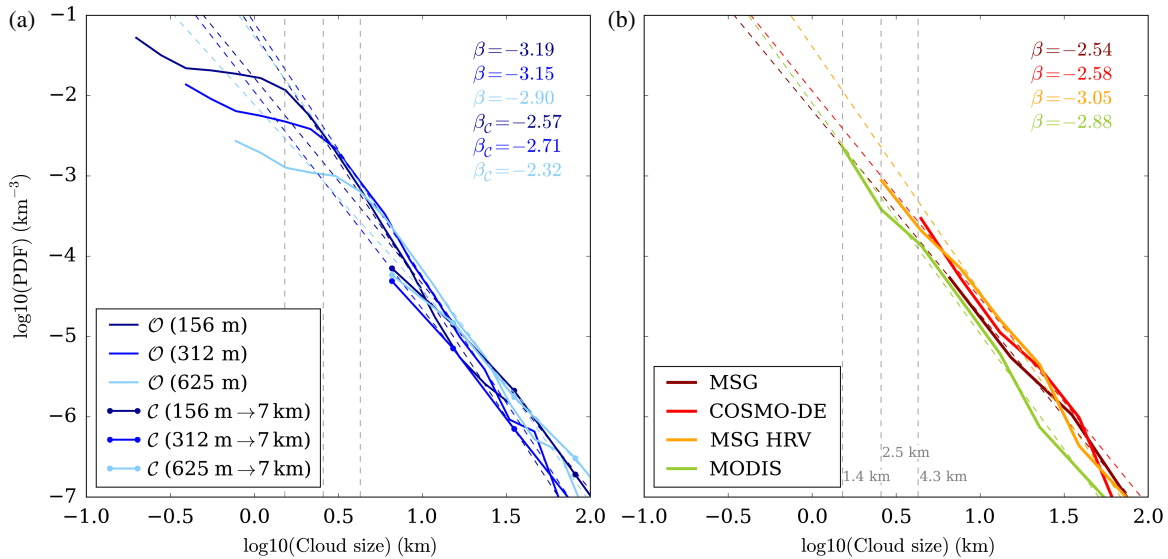


**Figure 8.** Domain-scale frequency distribution for cloud sizes (a) simulated by ICON-LEM and (b) observed by Meteosat (dark red), the Meteosat HRV mask (orange) and MODIS (green) and simulated by COSMO-DE (red) on 25 April 2013. The native ICON-LEM curves are shown as solid lines, and the coarse-grained distributions are additionally marked by filled circles. Linear regressions of the size distributions between different size ranges are indicated by dashed lines which can be described by the power law with exponent  $\beta$ . The standard error of the linear regression is  $\sim 0.1$  for the original ICON-LEM distributions,  $\sim 0.15$  for MSG, MODIS, MSG-HRV mask and COSMO-DE and  $\sim 0.3$  for the coarse-grained ICON-LEM functions. [Colour figure can be viewed at [wileyonlinelibrary.com](http://wileyonlinelibrary.com)].

Exponents between  $-2.3$  and  $-2.7$  are found for the coarse-grained fields and MSG, whereas a somewhat steeper decline with exponents between  $-2.9$  and  $-3.2$  is obtained for higher-resolution cloud fields. However, the power laws only show a moderate resolution sensitivity, which is consistent with a study by Wood and Field (2011), who demonstrated that sensor resolution is not found to strongly influence the power law. Koren *et al.* (2008) investigated the resolution sensitivity of the cloud size distribution by comparing Landsat and MODIS data with 30 m and 1 km spatial resolution, respectively. They concluded that, at any spatial resolution, a substantial number of small clouds are missed and that clouds below the sensor detection limit are more numerous than the detectable ones.

The ICON-LEM power law range between  $-2.9$  and  $-3.2$  is consistent with power laws obtained in a LES study by Heus and Seifert (2013) who found  $-2.2$  to  $-2.9$ . Heinze *et al.* (2016) calculated MODIS-like ICON-LEM satellite images based on a fast radiative transfer method (Scheck *et al.*, 2016) for calculating the distribution of cloud sizes from the visible images, resulting in  $\beta = -3.1$ .

Using the Meteosat HRV mask for the object-based analysis yields an exponent of  $\beta = -3.05$ , which is also in an excellent agreement with the ICON-LEM slopes. Considering the fit standard errors of  $0.1$ – $0.3$ , the coarse-grained power laws remain consistent with other satellite-based studies like Zhao and Di Girolamo (2007), who estimated  $\beta = -2.85$ . Due to the relatively small number of data points for the COSMO-DE, MSG and coarse-grained ICON-LEM fits, these power laws should be interpreted with caution.

While the parameters of the fitted power laws show just a moderate resolution sensitivity, the ICON-LEM distributions start to strongly deviate from the power laws for sizes smaller than 1.4 km, 2.5 km and 4.3 km for ICON-LEM  $\mathcal{O}(156 \text{ m})$ , ICON-LEM  $\mathcal{O}(312 \text{ m})$  and ICON-LEM  $\mathcal{O}(625 \text{ m})$ , respectively. These cloud sizes are in the range of the effective model resolution, which is about 8–10 times the native grid resolution (Zängl *et al.*, 2015). Consequently, ICON-LEM suppresses clouds that are smaller than this effective resolution. This clearly has implications for the planning of high-resolution simulations of cloud processes: if a reliable description of cloud and precipitation processes at a 1 km scale is targeted, then the native model resolution has to

be chosen to be 156 m or higher to avoid the impact of artificial numerical smoothing.

### 3.5. Decorrelation length- and time-scales

We follow the methodology of Bley *et al.* (2016) and investigate the decorrelation scales and their resolution sensitivity in ICON-LEM warm convective cloud fields. Based on MSG observations, Bley *et al.* (2016) estimated the average cloud lifetime of warm convective clouds by approaching a Lagrangian perspective. In the present study, simulated warm convective cloud fields are analyzed in a similar way. A set of ten local-scale cloud scenes are analyzed. The decorrelation length is calculated for a horizontal displacement of a box at constant time. The Lagrangian decorrelation time is calculated along the trajectory, while the Eulerian decorrelation time is obtained for a constant location. While the Lagrangian decorrelation time is expected to be generally larger than the Eulerian decorrelation time, the latter is also beneficial to estimate the impact of advective processes onto the local decorrelation behaviour.

Figure 9 shows the decorrelation length, Eulerian decorrelation time and Lagrangian decorrelation time as averages of ten ICON-LEM and COSMO-DE fields of warm convective clouds in relation to the reciprocal horizontal resolution. The black diamonds illustrate the MSG scales obtained by Bley *et al.* (2016). Two red diamonds show the COSMO-DE decorrelation lengths for its original 2.8 km and coarse-grained 5.6 km resolution, but no decorrelation time scales were calculated due to its coarse temporal sampling of 15 min, which does not allow the determination of reliable cloud field tracks (Bley *et al.*, 2016).

An excellent agreement is found between the observed and the ICON-LEM  $\mathcal{C}(7 \text{ km})$  scales within the error range. The spatial decorrelation scales of COSMO-DE  $\mathcal{O}(2.8 \text{ km})$  and COSMO-DE  $\mathcal{C}(5.6 \text{ km})$  also match well with the ICON-LEM scales within the respective reciprocal resolution. In contrast, ICON-LEM cloud fields at 156 m resolution exhibit substantially lower decorrelation lengths of 1 km and Lagrangian decorrelation times of 10 min. This result also demonstrates a high amount of unresolved cloud variability in the coarse-grained ICON-LEM and MSG cloud fields, which causes the high-resolution sensitivity of the decorrelation scales.

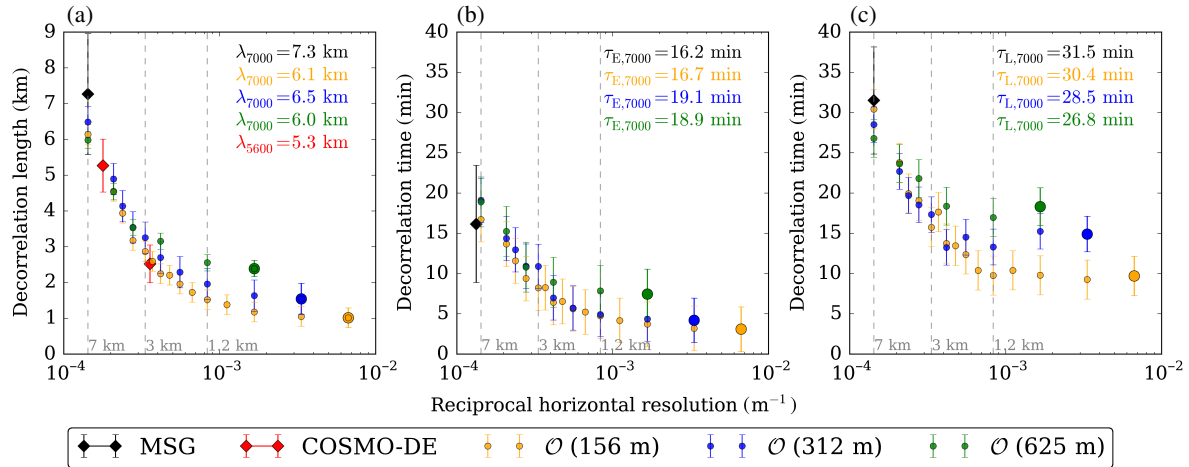


**Figure 9.** (a) Spatial decorrelation length and (b) Eulerian and (c) Lagrangian decorrelation times in relation to the reciprocal horizontal resolution of simulations from ICON-LEM  $\mathcal{O}$ (156 m) (yellow),  $\mathcal{O}$ (312 m) (blue) and  $\mathcal{O}$ (625 m) (green), COSMO-DE (red) and observations by MSG (black) of warm convective cloud fields on a local scale averaged over ten  $62 \times 62 \text{ km}^2$  LWP fields. The large circles represent the ICON-LEM scales for their native resolution, and smaller circles indicate the coarse-grained ICON-LEM scales. The vertical error bars indicate the standard deviation between the different cases for ICON-LEM, COSMO-DE and MSG. [Colour figure can be viewed at [wileyonlinelibrary.com](http://wileyonlinelibrary.com)].

Bley *et al.* (2016) found average spatial decorrelation scales of 7 km and Lagrangian decorrelation times of 30 min. It was further shown that the decorrelation scales start to decrease when the HRV channel with  $1 \times 2 \text{ km}^2$  resolution is utilized. The metrics which are presented here for characterizing the decorrelation scales give the opportunity to understand more clearly the resolution sensitivity of decorrelation scales.

The ICON-LEM cloud fields of 156, 312 and 625 m native resolution attain similar decorrelation scales between 4 and 7 km spatial resolution. At higher spatial resolution, they start to deviate from each other. Consequently, and similar to the distribution of cloud sizes (Figure 8), the decorrelation scales below the effective model resolution are not fully resolved. The Lagrangian decorrelation times exhibit the highest deviations between the different ICON-LEM runs, which is caused by uncertainties in the tracking. Thus, an accurate tracking is necessary to study warm convective cloud fields in a Lagrangian reference frame. An extrapolation of the resolution dependency of considered decorrelation scales beyond the effective model resolution is not physically meaningful. This also holds true for all other considered metrics.

With the MSG SEVIRI rapid scan, we are able to characterize the changes in convective cloud fields with an update frequency of 5 min, which is sufficient for its spatial resolution. The biggest limit of MSG is the spatial resolution, which leads to a substantial overestimation of the CF and decorrelation scales and underestimation of the LWP. The future generation of European geostationary satellites, the Meteosat Third Generation, will give great opportunity to bring down these limits to a spatial resolution of 1 km or even 500 m for selected channels (Stuhlmann *et al.*, 2005). The analyzed scaling behaviour of Figure 9 suggests the conclusion that the planned temporal update frequency of 10 min for the operational scan schedule and 2.5 min for the rapid scan are still sufficient to thoroughly characterize the decorrelation properties, including an estimate of the cloud lifetime, of convective cloud fields at the corresponding spatial scales.

#### 4. Summary and conclusions

In the present study, several metrics have been investigated to evaluate the representation of convective clouds in the high-resolution atmospheric model ICON-LEM with observations from the geostationary Meteosat SEVIRI instrument. ICON-LEM simulations covering a large domain at 156 m grid resolution

and containing convective cloud fields have been analyzed and compared to Meteosat observations and simulations with the COSMO-DE model. A variety of metrics including the time series of convective cloud fraction and LWP, the frequency distributions of LWP and cloud size, and the spatial and temporal decorrelation length-scales, have been considered. Using the cloud fields at three ICON-LEM native grid resolutions and after coarse-graining, the sensitivity of these metrics to the spatial resolution of the model and the observations has also been quantified.

The evaluation is performed on two types of cloud scenes: the one defined on the domain scale and including a variety of local conditions and the other one defined on the local scale following a convective cloud field during its temporal evolution in a Lagrangian perspective. For the latter, a set of ten cloud cases was collected with areal coverage of  $62 \times 62 \text{ km}^2$ . Cloud fields containing ice have been excluded to avoid complications caused by mixed-phase and precipitating clouds. We have further imposed an upper limit on the CF for the simulated cloud fields, to focus on broken convective cloud fields with a high degree of spatial inhomogeneity.

On a domain scale, we analyzed the spatial and temporal LWP and convective CF distribution as well as the cloud size distributions of convective cloud fields. On the local scale, spatio-temporal statistics of simulated cloud fields are compared to MSG observations. Sequences of LWP fields from ICON-LEM with a 1 min repeat cycle have been used to determine cloud field tracks to evaluate along-track correlation statistics and to study the resolution sensitivity on these scales. For this issue, ICON-LEM is gradually coarse-grained to the MSG resolution.

The main results are summarized as follows:

- (i) The coarse-grained ICON-LEM fields show improvements in the representation of the frequency distribution of the LWP, convective CF and cloud sizes compared to convection-permitting simulations of COSMO-DE.
- (ii) A substantial resolution sensitivity is found for the convective CF, in-cloud LWP and decorrelation scales. However, the power laws of the cloud size distribution exhibit only a moderate resolution sensitivity. The different metrics show that the spatial resolution needs to be considered to avoid the interpretation of non-physical differences that are attributable to the different resolutions. One could alternatively compare time series of the LWP on a domain average which substantially reduces the resolution sensitivity.



- (iii) The results suggest that Meteosat is mainly limited by its spatial resolution, which is much coarser than the decorrelation length-scales. Due to its coarse spatial resolution, a lot of the small-scale LWP variability remains unresolved, which causes large uncertainties. If the spatial resolution of a satellite instrument were highly increased, the temporal resolution needs also to be increased, to allow an accurate characterization of the spatio-temporal behaviour.

Because the present study is based on a selection of only ten cases obtained from four days of simulations, it remains unclear whether our results are statistically robust and representative, in particular for other synoptic conditions. Nevertheless, the methodology presented here can serve as an example for future studies aimed at evaluating the representation of convective clouds in high-resolution models. A larger number of simulation days will allow us to verify the robustness of our results. To address this point, it is planned to carry out more ICON-LEM runs over Germany and over the Atlantic Ocean within the second phase of the HD(CP)<sup>2</sup> project.

In terms of comparability, forward satellite simulators using ICON-LEM cloud properties will be important to account for inconsistencies between assumptions made in satellite retrievals and simulations of convective clouds. Such simulators will also improve the quantification of retrieval sensitivities at very small or large LWP values. As soon as the implementation of the absorbing 1.6  $\mu\text{m}$  channel in the satellite forward operator is finished, it will become possible to apply the LWP retrieval algorithm on model data and thus to investigate such inconsistencies and sensitivities.

The intercomparison of observations and high-resolution model output demonstrates that Meteosat SEVIRI observations are limited by the sensor spatial resolution in the rapid scan mode. If the spatial resolution were highly increased to 500 m or even 100 m, an enhancement of the temporal resolution would be required also, in order to consider rapid changes of convective clouds and to calculate accurate cloud field tracks. In 2020, six new satellites from the Meteosat Third Generation will be launched, which will have operational scans down to 500 m resolution (Stuhlmann *et al.*, 2005).

Recent atmospheric models are still unable to fully resolve convective cloud processes in particular for large-domain simulations. This study demonstrates that even ICON-LEM with a native resolution of  $\mathcal{O}(156\text{ m})$  is not able to fully resolve the spatio-temporal variability of convective clouds in the so-called grey zone as power spectra are indicating (Dorrestijn *et al.*, 2012). The effective model resolution has implications for the planning of high-resolution simulations, where cloud processes on a 1 km scale need to be simulated at 150 m grid size or less. The insights gained here into the scaling behaviour at different model resolutions can help to improve stochastic parametrizations of cumulus convection in future modelling studies, and to better compare observational datasets and model results with different resolutions. Additionally, there is still a great step to go towards a large-domain observational dataset with a similar spatial and temporal resolution like ICON-LEM. Using data from the HRV channel with 1 km spatial and 5 min temporal resolution has already demonstrated a reduction in the tracking uncertainties (Bley *et al.*, 2016). The authors are currently developing an extension of the cloud property retrieval to the high resolution of Meteosat.

## Acknowledgements

Sebastian Bley's position was funded by the German Ministry of Education and Research (BMBF) under grant 01LK1210B. The study was done within the framework of the German-wide research initiative High Definition Clouds and Precipitation for Climate Prediction (HD(CP)<sup>2</sup>). Fabian Senf acknowledges funding by the BMBF project HD(CP)<sup>2</sup> phase II under grant

01LK1507C. We thank Rieke Heinze and Ksenia Gorges for providing the ICON-LEM data, and for their support regarding the management of huge datasets as well as Christian Barthlott who provided the COSMO-DE reference runs. We further acknowledge EUMETSAT for providing Meteosat SEVIRI data. Many thanks also to our colleagues for the many thoughtful comments which helped to improve this manuscript. We thank three anonymous reviewers for their supportive and constructive comments.

## References

- Anuta PE. 1970. Spatial registration of multispectral and multitemporal digital imagery using fast fourier transform techniques. *IEEE Trans. Geosci. Electron.* **8**: 353–368. <https://doi.org/10.1109/TGE.1970.271435>.
- Baldauf M, Seifert A, Förstner J, Majewski D, Raschendorfer M, Reinhardt T. 2011. Operational convective-scale numerical weather prediction with the COSMO model: Description and sensitivities. *Mon. Weather Rev.* **139**: 3887–3905. <https://doi.org/10.1175/MWR-D-10-05013.1>.
- Benner TC, Curry JA. 1998. Characteristics of small tropical cumulus clouds and their impact on the environment. *J. Geophys. Res. Atmos.* **103**: 28753–28767. <https://doi.org/10.1029/98JD02579>.
- Bley S, Deneke H, Senf F. 2016. Meteosat-based characterization of the spatio-temporal evolution of warm convective cloud fields over Central Europe. *J. Appl. Meteorol. Climatol.* **55**: 2181–2195. <https://doi.org/10.1175/JAMC-D-15-0335.1>.
- Bony S, Stevens B, Frierson DMW, Jakob C, Kageyama M, Pincus R, Shepherd TG, Sherwood SC, Siebesma AP, Sobel AH, Watanabe M, Webb MJ. 2015. Clouds, circulation and climate sensitivity. *Nat. Geosci.* **8**: 261–268.
- Brown AR. 1999. The sensitivity of large-eddy simulations of shallow cumulus convection to resolution and subgrid model. *Q. J. R. Meteorol. Soc.* **125**: 469–482. <https://doi.org/10.1002/qj.4971255405>.
- Cho HM, Zhang Z, Meyer K, Lebsock M, Platnick S, Ackerman AS, Di Girolamo L, C-Labonne L, Cornet C, Riedi J, Holz RE. 2015. Frequency and causes of failed MODIS cloud property retrievals for liquid phase clouds over global oceans. *J. Geophys. Res. Atmos.* **120**: 4132–4154. <https://doi.org/10.1002/2015JD023161>.
- Deneke HM, Roebeling RA. 2010. Downscaling of METEOSAT SEVIRI 0.6 and 0.8  $\mu\text{m}$  channel radiances utilizing the high-resolution visible channel. *Atmos. Chem. Phys.* **10**: 9761–9772.
- Dipankar A, Stevens B, Heinze R, Moseley C, Zängl G, Giorgetta M, Brdar S. 2015. Large-eddy simulation using the general circulation model ICON. *J. Adv. Model. Earth Syst.* **7**: 1942–2466. <https://doi.org/10.1002/2015MS000431>.
- Dorrestijn J, Crommelin DT, Siebesma AP, Jonker HJJ. 2012. Stochastic parameterization of shallow cumulus convection estimated from high-resolution model data. *Theor. Comput. Fluid Dyn.* **27**: 133–148. <https://doi.org/10.1007/s00162-012-0281-y>.
- Evan AT, Heidinger AK, Vimont DJ. 2007. Arguments against a physical long-term trend in global ISCCP cloud amounts. *Geophys. Res. Lett.* **34**: L04701. <https://doi.org/10.1029/2006GL028083>.
- Han D, Ellingson RG. 1999. Cumulus cloud formulations for longwave radiation calculations. *J. Atmos. Sci.* **56**: 837–851. <https://doi.org/10.1175/1520-0469>.
- Heinze R, Dipankar A, Carbajal Henken C, Moseley C, Sourdeval O, Trömel S, Xie X, Adamidis P, Ament F, Baars H, Barthlott C, Behrendt A, Blahak U, Bley S, Brdar S, Brueck M, Crewell S, Deneke H, Di Girolamo P, Evaristo R, Fischer J, Frank C, Friederichs P, Göcke T, Gorges K, Hande L, Hanke M, Hansen A, Hege HC, Hoose C, Jahns T, Kalthoff N, Klocke D, Kneifel S, Knippertz P, Kuhn A, van Laar T, Macke A, Maurer V, Mayer B, Meyer CI, Muppa SK, Neggers RAJ, Orlandi Pantillon E, Pospichal F, Röber B, Scheck N, Seifert L, Seifert A, Senf F, Siligam F, Simmer P, Steinke C, Stevens S, Wapler B, Weniger K, Wulfmeyer M, Zängl V, Zhang G, Quaas D. 2016. Large-eddy simulations over Germany using ICON: A comprehensive evaluation. *Q. J. R. Meteorol. Soc.* **143**: 69–100. <https://doi.org/10.1002/qj.2947>.
- Heus T, Seifert A. 2013. Automated tracking of shallow cumulus clouds in large domain, long duration large-eddy simulations. *Geosci. Model Dev.* **6**: 1261–1273.
- Hohenegger C, Brockhaus P, Schär C. 2008. Towards climate simulations at cloud-resolving scales. *Meteorol. Z.* **17**: 383–394. <https://doi.org/10.1127/0941-2948/2008/0303>.
- Horvath A, Seethala C, Deneke H. 2014. View angle dependence of MODIS liquid water path retrievals in warm oceanic clouds. *J. Geophys. Res.* **119**: 8304–8328. <https://doi.org/10.1002/2013JD021355>.
- Jiang H, Xue H, Teller A, Feingold G, Levin Z. 2006. Aerosol effects on the lifetime of shallow cumulus. *Geophys. Res. Lett.* **33**: L14806. <https://doi.org/10.1029/2006GL026024>.
- Kassianov E, Long CN, Ovtchinnikov M. 2005. Cloud sky cover versus cloud fraction: Whole-sky simulations and observations. *J. Appl. Meteorol.* **44**: 86–98. <https://doi.org/10.1175/JAM-2184.1>.

- Koren I, Oreopoulos L, Feingold G, Remer LA, Altaratz O. 2008. How small is a small cloud? *Atmos. Chem. Phys.* **8**: 3855–3864. <https://doi.org/10.5194/acp-8-3855-2008>.
- Kostka PM, Weissmann M, Buras R, Mayer B, Stiller O. 2014. Observation operator for visible and near-infrared satellite reflectances. *J. Atmos. Oceanic Technol.* **31**: 1216–1233. <https://doi.org/10.1175/JTECH-D-13-00116.1>.
- Lensky IM, Rosenfeld D. 2008. Clouds–Aerosols–Precipitation Satellite Analysis Tool (CAPSAT). *Atmos. Chem. Phys.* **8**: 6739–6753.
- Marshak A, Platnick S, Várnai T, Wen G, Cahalan RF. 2006. Impact of three-dimensional radiative effects on satellite retrievals of cloud droplet sizes. *J. Geophys. Res.* **111**: D09207. <https://doi.org/10.1029/2005JD006686>.
- Mechem DB, Yuter SE, deZoeke SP. 2012. Thermodynamic and aerosol controls in southeast Pacific stratocumulus. *J. Atmos. Sci.* **69**: 1250–1266. <https://doi.org/10.1175/JAS-D-11-0165.1>.
- Merk D, Deneke H, Pospichal B, Seifert P. 2016. Investigation of the adiabatic assumption for estimating cloud micro- and macrophysical properties from satellite and ground observations. *Atmos. Chem. Phys.* **16**: 933–952. <https://doi.org/10.5194/acp-16-933-2016>.
- Minnis P. 1989. Viewing zenith angle dependence of cloudiness determined from coincident GOES East and GOES West data. *J. Geophys. Res. Atmos.* **94**: 2303–2320. <https://doi.org/10.1029/JD094iD02p02303>.
- Nagasawa R, Iwasaki T, Asano S, Saito K, Okamoto H. 2006. Resolution dependence of non-hydrostatic models in simulating the formation and evolution of low-level clouds during a 'Yamase' event. *J. Meteorol. Soc. Jpn. Ser. II* **84**: 969–987. <https://doi.org/10.2151/jmsj.84.969>.
- Neggers RAJ, Jonker HJJ, Siebesma AP. 2003. Size statistics of cumulus cloud populations in large-eddy simulations. *J. Atmos. Sci.* **60**: 1060–1074. [https://doi.org/10.1175/1520-0469\(2003\)60\\$\(\\$1060:SSOCCP\\$\)\\$2.0.CO;2](https://doi.org/10.1175/1520-0469(2003)60$($1060:SSOCCP$)$2.0.CO;2).
- Roebeling RA, Feijt AJ, Stammes P. 2006. Cloud property retrievals for climate monitoring: Implications of differences between Spinning Enhanced Visible and Infrared Imager (SEVIRI) on METEOSAT-8 and Advanced Very High Resolution Radiometer (AVHRR) on NOAA-17. *J. Geophys. Res.* **111**: D20210. <https://doi.org/10.1029/2005JD006990>.
- Scheck L, Fréreau P, Buras-Schnell R, Mayer B. 2016. A fast radiative transfer method for the simulation of visible satellite imagery. *J. Quant. Spectrosc. Radiat. Trans.* **175**: 54–67. <https://doi.org/10.1016/j.jqsrt.2016.02.008>.
- Schulz J, Albert P, Behr H-D, Caprion D, Deneke H, Dewitte S, Dürr B, Fuchs P, Gratzki A, Hechler P, Hollmann R, Johnston S, Karlsson K-G, Manninen T, Müller R, Reuter M, Riihelä A, Roebeling R, Selbach N, Tetzlaff A, Thomas W, Werscheck M, Wolters E, Zelenka A. 2009. Operational climate monitoring from space: The EUMETSAT satellite application facility on climate monitoring (CM-SAF). *Atmos. Chem. Phys.* **9**: 1687–1709. <https://doi.org/10.5194/acp-9-1687-2009>.
- Seifert A, Beheng DK. 2005. A two-moment cloud microphysics parameterization for mixed-phase clouds. Part I: Model description. *Meteorol. Atmos. Phys.* **92**: 45–66. <https://doi.org/10.1007/s00703-005-0112-4>.
- Senf F, Dietzsch F, Hünerbein A, Deneke H. 2015. Characterization of initiation and growth of selected severe convective storms over Central Europe with MSG-SEVIRI. *J. Appl. Meteorol. Climatol.* **54**: 207–224. <https://doi.org/10.1175/JAMC-D-14-0144.1>.
- Stevens DE, Ackerman AS, Bretherton CS. 2002. Effects of domain size and numerical resolution on the simulation of shallow cumulus convection. *J. Atmos. Sci.* **59**: 3285–3301. [https://doi.org/10.1175/1520-0469\(2002\)059\\$\(\\$3285:EODSAN\\$\)\\$2.0.CO;2](https://doi.org/10.1175/1520-0469(2002)059$($3285:EODSAN$)$2.0.CO;2).
- Stuhlmann R, Rodriguez A, Tjemkes S, Grandell J, Arriaga A, Bézy JL, Aminou D, Bensi P. 2005. Plans for EUMETSATs Third Generation Meteosat geostationary satellite programme. *Adv. Space Res.* **36**: 975–981. <https://doi.org/10.1016/j.asr.2005.03.091>.
- Várnai T, Marshak A. 2007. View angle dependence of cloud optical thicknesses retrieved by Moderate Resolution Imaging Spectroradiometer (MODIS). *J. Geophys. Res. Atmos.* **112**: D06203. <https://doi.org/10.1029/2005JD006912>.
- Weisman ML, Skamarock WC, Klemp JB. 1997. The resolution dependence of explicitly modeled convective systems. *Mon. Weather Rev.* **125**: 527–548. [https://doi.org/10.1175/1520-0493\(1997\)125\\$\(\\$0527:TRDOEM\\$\)\\$2.0.CO;2](https://doi.org/10.1175/1520-0493(1997)125$($0527:TRDOEM$)$2.0.CO;2).
- Wolters ELA, Deneke HM, van den Hurk BJJM, Meirink JF, Roebeling RA. 2010. Broken and inhomogeneous cloud impact on satellite cloud particle effective radius and cloud-phase retrievals. *J. Geophys. Res.* **115**: D10214. <https://doi.org/10.1029/2009JD012205>.
- Wood R, Field PR. 2011. The distribution of cloud horizontal sizes. *J. Clim.* **24**: 4800–4816. <https://doi.org/10.1175/2011JCLI4056.1>.
- Zängl G, Reinert D, Ripodas P, Baldauf M. 2015. The ICON (ICOsahedral Non-hydrostatic) modelling framework of DWD and MPI-M: Description of the non-hydrostatic dynamical core. *Q. J. R. Meteorol. Soc.* **141**: 563–579. <https://doi.org/10.1002/qj.2378>.
- Zhao G, Di Girolamo L. 2007. Statistics on the macrophysical properties of trade wind cumuli over the tropical western Atlantic. *J. Geophys. Res.* **112**: D10204. <https://doi.org/10.1029/2006JD007371>.



## 5 Summary and Conclusions

The overall goal of the present thesis was an in-depth investigation of the spatiotemporal characteristics of convective cloud fields with the Spinning Enhanced Visible and Infrared Imager (SEVIRI) on-board the geostationary Meteosat satellite and its applicability towards model evaluation. The high resolution visible channel of SEVIRI was considered to improve the representation of small-scale convective cloud features, like their horizontal dimensions and their temporal evolution. The achieved techniques and findings were finally applied to high resolution model simulations to investigate the spatiotemporal characteristics of warm convective cloud fields across different spatial scales to advance our understanding of the effects of small-scale cloud processes. Towards this goal, we studied several metrics for comparing these high resolution model results with comparatively coarsely resolved satellite observations. The simulations of convective clouds are based on the ICON-LEM model, which was developed within the High Definition Clouds and Precipitation for Climate Prediction (HD(CP)<sup>2</sup>) project (Dipankar et al., 2015; Heinze et al., 2017). The simulations were conducted on different grid resolutions between 156 m and 625 m for the whole of Germany. The sensitivity of the studied metrics on the spatial resolution was quantified. The scaling behavior at a variety of spatial scales demonstrates new insights into the uncertainties of retrieved cloud properties and the current sensor limitations of Meteosat SEVIRI.

The main results of this thesis referring to the research questions formulated in section 1.5

1. How can we improve the representation of small-scale convective clouds using Meteosat observations?
2. What are suitable metrics for evaluating high resolution model simulations with relatively coarsely resolved satellite observations?
3. How sensitive are the spatiotemporal characteristics of convective cloud fields to the spatial resolution of a sensor or a model?

4. How can uncertainties of retrieved cloud properties and the instrumental limitations of MSG SEVIRI be quantified and which improvements are expected with respect to upcoming satellite missions?

are summarized as follows:

1. The high resolution visible channel was used to develop a cloud mask with an enhanced spatial resolution from  $3\times 6\text{ km}^2$  to  $1\times 2\text{ km}^2$  compared to the operational cloud mask. Suitable techniques were investigated to improve the representation of small-scale convective clouds and to further increase the resolution of retrieved convective cloud properties. The HRV mask identifies a ratio of 16 % of the operational cloudy pixel as fractional clouds on average.
2. The frequency distribution of the LWP, cloud size distribution and spatiotemporal scales were characterized across different spatial scales, ranging from the comparatively coarse satellite resolution to high model resolution. A sophisticated tracking algorithm was developed to quantify the convective and advective changes, which influence the evolution of warm convective cloud fields. The simulated spatiotemporal scales, however, had to be coarse-grained to the optical resolution of Meteosat to enable an appropriate evaluation and ensure comparability.
3. The investigated metrics reveal a pronounced sensitivity to the spatial model and satellite sensor resolution. The scaling behavior of the spatiotemporal characteristics and the cloud size distribution of the simulations indicates the effective resolution of the ICON-LEM model, which is 8–10 times the native model grid resolution.
4. The gained insights into the sensitivity of the spatiotemporal characteristics on the spatial resolution indicate that an increase of the spatial resolution to 1 km or even 500 m would be desirable for the Meteosat cloud properties, to better quantify the small-scale variability of convective clouds. This range will be covered by Meteosat Third Generation (MTG) and highlights the great opportunity to improve the observations of convective clouds once the new series of satellites is launched in 2021.

In the first study presented here (Bley and Deneke, 2013), a threshold-based cloud mask was developed for the high resolution visible (HRV) channel of Meteosat SEVIRI to improve the identification of small-scale convective clouds. It has an enhanced spatial resolution of  $1\times 2\text{ km}^2$  in comparison to the operational cloud mask with  $3\times 6\text{ km}^2$

resolution, and accounts for inhomogeneities in the land surface reflectance by using clear-sky reflectance composites from temporally averaged clear-sky images. These composites are considered as input for an iterative algorithm to reduce the overlap in the histograms of the clear-sky and cloudy reflectances, and thus to optimize the threshold relative to the underlying surface reflectance. The study finally shows that the HRV channel offers important sub-pixel information for the remaining low-resolution channels, and substantially improves the identification of low-level convective clouds which was exemplarily shown over the Upper Rhine Valley. This region was chosen as one of the case studies, because it is characterized by a high frequency of orographically induced convective clouds. On average over all case studies, 16 % of the pixels which are classified as cloudy by the operational EUMETSAT cloud mask correspond to fractional clouds in the HRV cloud mask. This fraction increases up to 20 % over the Upper Rhine Valley. The results indicate that the HRV cloud mask performs very reliably in cloudy conditions and misses only 10 % of the cloudy pixels which are attributable to thin cirrus clouds. These thin cirrus cloud misses were, however, restored in the HRV cloud mask.

This HRV mask together with high resolution clear sky reflectance composites is part of our wider effort to extend the cloud physical property retrieval (Roebeling et al., 2006) to the high spatial resolution which has been already performed for the cloud optical thickness (Carbajal Henken et al., 2011). The higher spatial resolution will reduce the cloud property uncertainties due to the plane-parallel albedo bias which has a substantial impact for fractional cumulus clouds (e.g., Wolters et al., 2010; Marshak et al., 2006). These uncertainties also depend on the viewing geometry, which can introduce further complications (Horváth et al., 2014). Mécikalski et al. (2013) used the HRV channel to sharpen infrared pixels to improve the estimation of the cloud top temperature and height. They reported a strong influence of the fractional cloudiness on the estimation of the cloud top temperature, especially for small sub-pixel cloud fractions. A recent study by Zhang et al. (2016) used a framework of synthetic cloud fields from a LES simulation together with MODIS observations to investigate the influence of the unresolved reflectance variations on the  $\tau$  and  $r_e$  retrieval based on a bispectral method. They summarized that the unresolved reflectance variability in low resolution satellite observations mainly causes a positive bias in the retrieval of  $r_e$ . The HRV channel contains valuable information about these reflectance variations and, is thus also used in Senf et al. (2015) for improving the tracking and characterization of convective storms.

The subject of the second study (Bley et al., 2016) was to characterize the spatiotemporal evolution of warm convective cloud fields with Meteosat SEVIRI over

Central Europe. Solar reflectances have been used together with cloud products (cloud optical thickness, droplet effective radius, liquid water path, droplet number concentration and HRV cloud mask) to investigate spatiotemporal decorrelation scales in an Eulerian and a Lagrangian reference frame. For the latter, a tracking algorithm was applied to sequential satellite images from the HRV channel. The decorrelation scales represent a change of the spatial and temporal coherence of the horizontal cloud field structure, while the Lagrangian decorrelation time is assumed as average cloud life time. Results obtained with the HRV channel at high spatial resolution ( $1.2 \times 2 \text{ km}^2$ ) and SEVIRI's standard resolution ( $3.6 \times 6 \text{ km}^2$ ) indicate a high sensitivity to the spatial resolution, which is most likely due to small-scale variability in cloud structures which decorrelate much faster than large-scale cloud features. Besides this resolution sensitivity, the  $0.6 \text{ }\mu\text{m}$  reflectance fields reveal explicitly higher decorrelation times than the  $0.8 \text{ }\mu\text{m}$ -channel, because the latter is highly sensitive to variations in the underlying surface reflectance, which also influence the tracking accuracy. The spatial pattern of  $\tau$  as well as LWP shows, however, similar decorrelation scales like the  $0.6 \text{ }\mu\text{m}$  reflectance. The LWP has been used for the main analysis, because it is a quantity that facilitates a process-based interpretation and allows direct comparison with atmospheric models. For all cases, a Lagrangian decorrelation time of 31 min and a spatial decorrelation length scale of 7 km is found. As expected, the warm convective cloud fields decorrelate much faster in an Eulerian reference frame, because of the decorrelation by the horizontal advection, which can be most likely neglected when adopting the Lagrangian perspective. Slobodda et al. (2015) considered the spatial decorrelation length as an indicator for the representativeness of a point measurement for its surrounding. They found similar decorrelation scales with smaller values for the solar channels, which correspond to the cloud microphysical properties, compared to the infrared channels.

Several sources of uncertainties have been identified for the calculated spatiotemporal characteristics, which are basically attributable to the limited spatial resolution of Meteosat. To overcome these limitations, the HRV channel was already used in a study by Carbajal Henken et al. (2011). Madhavan et al. (2017) investigated the spatiotemporal variability in global radiation measurements for varying length scales ranging from 100 m to 10 km and averaging time scales below 1 min. A network of 99 pyranometers was used to measure the global radiation with a high frequency. Their results also show a significant decrease of the spatiotemporal correlation for all considered frequencies, especially in situations with broken clouds.

To deepen our understanding of small-scale convective cloud variability, which can be only coarsely covered by current Meteosat observations, we need realistic simulations of

convective clouds at a high spatial resolution and for a large domain. Such simulations can also serve as reference for upcoming geostationary satellite missions like MTG with substantially enhanced spatial resolution compared to MSG (Stuhlmann et al., 2005). Furthermore, reliable metrics are required to exploit current Meteosat observations for model evaluation and for the development of parameterizations in GCMs.

The third study (Bley et al., 2017) builds on the methods developed in Bley et al. (2016) and proposes metrics for the evaluation of simulated convective cloud fields in a large eddy simulation. Several metrics are investigated in order to compare simulated convective cloud field characteristics from high resolution models with comparatively coarse resolution Meteosat observations and model results from the German operational model COSMO-DE. At a very fine spatial scale of 156 m, the simulations show a higher frequency of large LWP values with a factor of two to four smaller convective cloud fractions. Also the Lagrangian decorrelation time falls from 30 min to 10 min for an increase in the spatial resolution from 7 km to 1 km. Coarse graining of the simulated fields removes most of the differences between the observations and the simulations. It was shown that the effect of the oblique viewing geometry of Meteosat has only a comparatively minor influence on the convective cloud fraction compared to the resolution sensitivity, and can thus be neglected. The distribution of the cloud sizes can be represented by a power law and compares well between the observation and simulations. This power law is consistent across the different spatial scales, indicating a scale invariant metric, while all other investigated metrics show a high resolution sensitivity. The power law, however, shows a lower limit for the simulated cloud sizes that is in the range of 8–10 times the native model resolution which most likely corresponds to the effective resolution of the ICON-LEM model. This implies that simulations with a least 156 m grid resolution are required in order to resolve spatial cloud structures of 1 km. Barthlott and Hoose (2015) recently conducted simulations with the COSMO-DE model at grid resolutions between 2.8 km and 250 m, to investigate how the spatial resolution of the model influences the representation of convective clouds. They found that several meteorological processes, especially in the planetary boundary layer, show a strong resolution sensitivity. Furthermore, an effective grid resolution of 6–7 times the native resolution of COSMO-DE is inferred. In conclusion, they state that numerical simulations with a higher grid resolution of up to 100 m are desirable to improve the representation of boundary layer cloud processes.





## 6 Outlook

The results presented in this thesis demonstrate a significant sensitivity of most of the investigated metrics on the spatial resolution. This implies that the spatial resolution of a simulation or an observation needs to be carefully considered to avoid a nonphysical interpretation of the results in such a model evaluation. Beyond this resolution sensitivity, this study also quantifies several cloud field characteristics at varying spatial resolutions and the effect of satellite or model limitations. The scaling behavior at different model resolutions will further help to improve stochastic parameterizations of cumulus convection.

Determination of cloud radiative effects, especially in convective situations, remains highly uncertain due to the spatial variability of the cloud structures. Song et al. (2016) developed a parameterization to quantify the characteristic spectral signature of spatial cloud reflectance inhomogeneities. The high resolution cloud mask developed in this thesis provides important information about the small-scale fractional cloudiness and will thus help to improve the estimation of cloud radiative effects in Meteosat observations. It further gives the opportunity to calculate high temporal and spatial clear sky reflectances which are important for estimations of the aerosol concentration and for understanding the interaction between aerosol and convective clouds (Koren et al., 2008). The Meteosat cloud property retrieval of LWP is, however, still limited to a relatively coarse spatial resolution. An extension of the cloud property retrieval towards the resolution of the HRV cloud mask, including the LWP, is currently under development. An example satellite with highly spatially and temporally resolved measurements is the recently launched Geostationary Operational Environmental Satellite-R series (GOES-R) satellite, which is now operating over the USA with a spatial resolution down to 500 m for the visible 0.64  $\mu\text{m}$ -channel and rapid scans for limited areas with a repeat cycle of 30 sec (Schmit et al., 2005). For temporally resolved observations over Europe, however, the MSG series currently represents the state-of-the-art satellites until it will be replaced by Meteosat Third Generation, which will have similar performance as the GOES-R imager, but additionally to the 0.6  $\mu\text{m}$ -channel also a near-IR channel at 500 m resolution (Stuhlmann et al., 2005). This enhanced spatial resolution will significantly improve

the quantification of indirect aerosol effects by using collocated measurements or simulations of cloud condensation nuclei (CCN) (Merk et al., 2016). The wide range of spatial resolutions of observations and simulations has also implications on the uncertainty estimates of such effects (McComiskey and Feingold, 2012). Uncertainties in both satellite and model data cause large uncertainties in the quantification of the indirect aerosol climate forcing (Quaas et al., 2008). To substantially improve our understanding of aerosol-cloud-precipitation interactions and how they modify cloud microphysical properties, Rosenfeld et al. (2014) suggest to coordinate a wider effort using observations and models from process scale (where these interactions occur) to large scale (where sophisticated parameterizations are required).

Similar approaches as used in the present thesis to increase the spatial resolution of cloud products by using the high-frequency signal from the HRV channel are essential for upcoming satellite missions with different sensor resolutions and can be useful precursors for MTG. Such techniques can be also applied to polar-orbiting instruments with substantially higher spatial resolution to study unresolved cloud variability in coarser resolved satellite images. Zhang et al. (2016) used synthetic cloud fields and MODIS observations to investigate the influence of the unresolved reflectance variations within satellite pixels on the retrievals of  $\tau$  and  $r_e$ . They suggested to consider satellite data from ASTER, which has a much higher resolution than MODIS, leading to substantially improved texture information about the unresolved cloud variability.

Recent atmospheric models with comparable spatial resolution as ICON-LEM are still unable to fully resolve cloud processes in the so-called gray zone (Dorrestijn et al., 2012). Although the model runs on a 156 m grid, it indicates remarkable deficits below the effective resolution, which was found to be about 1.2 km. The effective model resolution has implications for the planning of upcoming high resolution simulations. A further increase in the ICON-LEM model resolution would be desirable in order to improve the representation of convective clouds below 1 km length scale. Also a larger number of simulations is required to verify the robustness of the results, especially under different synoptic conditions. This is already in progress in the second phase of the HD(CP)<sup>2</sup> project. Besides simulations over Germany, additional ICON-LEM runs will be conducted over the Atlantic Ocean, which will give the opportunity to investigate spatiotemporal cloud processes over the ocean. It is also shown that a further increase of the Cloud Physical Properties Retrieval would be desirable, too. The spatial resolution of the retrieved LWP is still much coarser than the spatial decorrelation scales of 1 km that were calculated for the simulated convective cloud fields. Fortunately, this resolution range will be captured by the Third Generation of the Meteosat satellites (Stuhlmann et al., 2005). The scale behavior of the decorrelation analysis indicates that

if the spatial resolution of the satellite sensor will be highly increased to 500 m or 100 m, the temporal resolution has to be increased as well. Fortunately, the passive imager onboard MTG will deliver a visible and a near-IR channel not only at a high spatial resolution of 500 m, but also with a higher repeat cycle of 2.5 min for the European Regional Rapid Scan.

Beyond considering the spatial resolution for an appropriate comparison between satellite retrieved and simulated cloud properties, the different assumptions in retrieval and model algorithms also represent an important source of uncertainty. Thus, uncertainties in the estimated cloud properties from satellite observations and models are not solely due to model and retrieval errors but also due to inconsistencies in their assumptions. These uncertainties can be quantified by utilizing satellite simulators. Such simulators apply inverse radiative transfer modeling to simulate satellite retrievals by considering model results about the sub-grid scale variability of clouds (Bodas-Salcedo et al., 2011). The pioneering ISCCP simulator is a diagnostic code that calculates what a satellite would retrieve for synthetic clouds by a given model output to improve the comparability of climate model output with satellite data (Klein et al., 2013). Their results demonstrate that simulations by climate models of the cloud amount, the cloud top pressure and particularly the cloud optical thickness have significantly improved over the last decade. To consider the spatial resolution of observations and simulations, these satellite simulators have to take into account the spatial limitations of the sensor (Quaas et al., 2004). Reverdy et al. (2015) introduced a Cloud Feedback Model Intercomparison Project Observation Simulator Package (COSP) for the ATmospheric LIDar (ATLID) instrument onboard the Earth Clouds, Aerosols and Radiation Explorer (EarthCARE) satellite to evaluate cloud fraction profiles predicted from GCMs, once EarthCARE is launched.

It should be also noted that passive satellite instruments, particularly on the geostationary orbit, are not able to provide a complete picture of the dynamical and microphysical cloud properties. To better understand aerosol-cloud interactions, Doppler radar instruments which will be operating on EarthCARE will provide better information about the updrafts and downdrafts of convective clouds complementary to measurements of the radiation at the same time (Illingworth et al., 2015).

In conclusion, this study emphasizes that a geostationary satellite instrument with a repeat cycle of at least 1 min and a horizontal resolution of 100 m would be desirable to substantially improve the characterization of convective clouds and the development of sophisticated parameterizations for numerical weather prediction and climate models. Such an observational capacity could contribute towards answering the question: “What

role does convection play in cloud feedbacks?” which is one of the big challenges of climate science as formulated by Bony et al. (2015).

# Appendix

## A.1 Authors contribution to the three publications

### **First publication: A threshold-based cloud mask for the high-resolution visible channel of Meteosat Second Generation SEVIRI**

In this publication, I developed the threshold-based HRV cloud mask algorithm, evaluated the data with the EUMETSAT cloud mask and wrote the manuscript draft. Moreover, I processed the HRV cloud mask for three years from 2012–2014 using the newly developed algorithm. Dr. Hartwig Deneke gave the full support, proposed many valuable suggestions for this study and carried out corrections for this publication.

### **Second publication: Meteosat-Based Characterization of the Spatiotemporal Evolution of Warm Convective Cloud Fields over Central Europe**

For this paper, I performed the tracking of the warm convective cloud fields and did the statistical analysis with the auto-correlation function. For the tracking, I adjusted the configuration of the high resolution wind product in the NWC SAF software package. I calculated the wind vectors and collected a case database with warm convective cloud fields over Central Europe. After a comprehensive analysis I wrote the manuscript draft with full support and many corrections carried out by Hartwig Deneke and Fabian Senf.

### **Third publication: Metrics for the evaluation of warm convective cloud fields in a large eddy simulation with Meteosat images**

For this study, I accessed and prepared the data output from the ICON-LEM and COSMO-DE simulations, which were both conducted in the HD(CP)<sup>2</sup> project. Due to the large model output of several TB per simulation day, it took me quite some time to cut out the relevant cloud microphysical data and to interpolate it to an equidistant two-dimensional grid to enable comparability with the satellite observations. In the next step, I developed a coarse-graining algorithm to average the high resolution model data to the satellite data and implemented the different metrics in the analysis in collaboration with Hartwig Deneke and Fabian Senf. Leonhard Scheck supported the distribution of the simulated cloud sizes and gave many valuable comments. I finally

wrote the manuscript draft, that was also supported and corrected by Hartwig Deneke and Fabian Senf.



## Bibliography

- Allan, R. P.: Combining satellite data and models to estimate cloud radiative effect at the surface and in the atmosphere, *Meteorol. Appl.*, 18, 324–333, 2011.
- Allan, R. P., Liu, C., Loeb, N. G., Palmer, M. D., Roberts, M., Smith, D., and Vidale, P.-L.: Changes in global net radiative imbalance 1985–2012, *Geophys. Res. Lett.*, 41, 5588–5597, 2014.
- Arakawa, A.: The cumulus parameterization problem: past, present, and future, *J. Climate*, 17, 2493–2525, 2004.
- Baldauf, M., Seifert, A., Förstner, J., Majewski, D., Raschendorfer, M., and Reinhardt, T.: Operational convective-scale numerical weather prediction with the COSMO model: Description and sensitivities, *Mon. Weather Rev.*, 139, 3887–3905, 2011.
- Barthlott, C. and Hoose, C.: Spatial and temporal variability of clouds and precipitation over Germany: multiscale simulations across the "gray zone", *Atmos. Chem. Phys.*, 15, 12 361–12 384, 2015.
- Bedka, K. M. and Mecikalski, J. R.: Application of satellite-derived atmospheric motion vectors for estimating mesoscale flows, *J. Appl. Meteor.*, 44, 1761–1772, 2005.
- Bley, S. and Deneke, H.: A threshold-based cloud mask for the high-resolution visible channel of Meteosat Second Generation SEVIRI, *Atmos. Meas. Tech.*, 6, 2713–2723, 2013.
- Bley, S., Deneke, H., and Senf, F.: Meteosat-based characterization of the spatiotemporal evolution of warm convective cloud fields over Central Europe, *J. Appl. Meteorol. Climat.*, 55, 2181–2195, 2016.
- Bley, S., Deneke, H., Senf, F., and Scheck, L.: Metrics for the evaluation of warm convective cloud fields in a large-eddy simulation with Meteosat images, *Q.J.R. Meteorol. Soc.*, 143, 2050–2060, 2017.

- Bodas-Salcedo, A., Webb, M. J., Bony, S., Chepfer, H., Dufresne, J.-L., Klein, S. A., Zhang, Y., Marchand, R., Haynes, J. M., Pincus, R., and John, V. O.: COSP: Satellite simulation software for model assessment, *Bull. Amer. Meteor. Soc.*, 92, 1023–1043, 2011.
- Bony, S., Stevens, B., Frierson, D. M. W., Jakob, C., Kageyama, M., Pincus, R., Shepherd, T. G., Sherwood, S. C., Siebesma, A. P., Sobel, A. H., Watanabe, M., and Webb, M. J.: Clouds, circulation and climate sensitivity, *Nat. Geosci.*, 8, 261–268, 2015.
- Cahalan, R. F., Ridgway, W., Wiscombe, W. J., Bell, T. L., and Snider, J. B.: The albedo of fractal stratocumulus clouds, *J. Atmos. Sci.*, 51, 2434–2455, 1994a.
- Cahalan, R. F., Ridgway, W., Wiscombe, W. J., Gollmer, S., and Harshvardhan: Independent pixel and monte carlo estimates of stratocumulus albedo, *J. Atmos. Sci.*, 51, 3776–3790, 1994b.
- Carbajal Henken, C., Schmeits, M. J., Deneke, H., and Roebeling, R. A.: Using MSG-SEVIRI cloud physical properties and weather radar observations for the detection of Cb/TCu clouds, *J. Appl. Meteor. Climatol.*, 50, 1587–1600, 2011.
- Cho, H.-M., Zhang, Z., Meyer, K., Lebsock, M., Platnick, S., Ackerman, A. S., Di Girolamo, L., C.-Labonnote, L., Cornet, C., Riedi, J., and Holz, R. E.: Frequency and causes of failed MODIS cloud property retrievals for liquid phase clouds over global oceans, *J. Geophys. Res. Atmos.*, 120, 4132–4154, 2015.
- Davis, A., Marshak, A., Wiscombe, W., and Cahalan, R.: Scale invariance of liquid water distributions in marine stratocumulus. Part I: Spectral properties and stationarity issues, *J. Atmos. Sci.*, 53, 1538–1558, 1996.
- Deneke, H. M. and Roebeling, R. A.: Downscaling of Meteosat SEVIRI 0.6 and 0.8  $\mu\text{m}$  channel radiances utilizing the high-resolution visible channel, *Atmos. Chem. Phys.*, 10, 9761–9772, 2010.
- Deneke, H. M., Knap, W. H., and Simmer, C.: Multiresolution analysis of the temporal variance and correlation of transmittance and reflectance of an atmospheric column, *J. Geophys. Res.*, 114, D17 206, 2009.
- Derrien, M.: Algorithm theoretical basis document for cloud products (cma-pge01 v3.2, ct-pge02 v2.2, ctth-pge03 v2.2). Technical report, Tech. Rep. 21, SAFNWC, 2012.

- Derrien, M. and Le Gléau, H.: MSG/SEVIRI cloud mask and type from SAFNWC, *Int. J. Remote Sens.*, 26, 4707–4732, 2005.
- Dipankar, A., Stevens, B., Heinze, R., Moseley, C., Zängl, G., Giorgetta, M., and Brdar, S.: Large eddy simulation using the general circulation model ICON, *J. Adv. Model. Earth Syst.*, 7, 1942–2466, 2015.
- Dorrestijn, J., Crommelin, D. T., Siebesma, A. P., and Jonker, H. J. J.: Stochastic parameterization of shallow cumulus convection estimated from high-resolution model data, *Theor. Comp. Fluid Dyn.*, 27, 133–148, 2012.
- Dufresne, J.-L. and Bony, S.: An assessment of the primary sources of spread of global warming estimates from coupled atmosphere–ocean models, *J. Climate*, 21, 5135–5144, 2008.
- Feijt, A. and Jonker, H.: Comparison of scaling parameters from spatial and temporal distributions of cloud properties, *J. Geophys. Res. Atmos.*, 105, 29 089–29 097, 2000.
- García-Pereda, J.: Algorithm theoretical basis document for high resolution winds (HRW - PGE09 v4.0). NWC SAF Doc. SAF/NWC/CDOP/INM/SCI/ATBD/09, Tech. Rep. Issue 4.0, EUMETSAT Satellite Application Facility on Support to Nowcasting and Very Short Range Forecasting (NWC SAF), 2013.
- Gupta, S. K., Ritchey, N. A., Wilber, A. C., Whitlock, C. H., Gibson, G. G., and Jr., P. W. S.: A climatology of surface radiation budget derived from satellite data, *J. Climate*, 12, 2691–2710, 1999.
- Han, Q., Rossow, W. B., and Lacis, A. A.: Near-Global Survey of Effective Droplet Radii in Liquid Water Clouds Using ISCCP Data, *J. Climate*, 7, 465–497, 1994.
- Hansen, J., Ruedy, R., Sato, M., and Lo, K.: Global surface temperature change, *Rev. Geophys.*, 48, RG4004, 2010.
- Hartmann, D., Klein Tank, A., Rusticucci, M., Alexander, L., Brönnimann, S., Charabi, Y., Dentener, F., Dlugokencky, E., Easterling, D., Kaplan, A., Soden, B., Thorne, P., Wild, M., and Zhai, P.: Observations: Atmosphere and surface, pp. 159–254, *Climate change 2013: The physical science basis. Contribution of working group I to the fifth assessment report of the intergovernmental panel on climate change*, Cambridge University Press, 2013.
- Hartmann, D. L., Ramanathan, V., Berroir, A., and Hunt, G. E.: Earth radiation budget data and climate research, *Rev. Geophys.*, 24, 439–468, 1986.

- Heinze, R., Dipankar, A., Carbajal Henken, C., Moseley, C., Sourdeval, O., Trömel, S., Xie, X., Adamidis, P., Ament, F., Baars, H., Barthlott, C., Behrendt, A., Blahak, U., Bley, S., Brdar, S., Brueck, M., Crewell, S., Deneke, H., Di Girolamo, P., Evaristo, R., Fischer, J., Frank, C., Friederichs, P., Göcke, T., Gorges, K., Hande, L., Hanke, M., Hansen, A., Hege, H.-C., Hoose, C., Jahns, T., Kalthoff, N., Klocke, D., Kneifel, S., Knippertz, P., Kuhn, A., van Laar, T., Macke, A., Maurer, V., Mayer, B., Meyer, C. I., Muppa, S. K., Neggers, R. A. J., Orlandi, E., Pantillon, F., Pospichal, B., Röber, N., Scheck, L., Seifert, A., Seifert, P., Senf, F., Siligam, P., Simmer, C., Steinke, S., Stevens, B., Wapler, K., Weniger, M., Wulfmeyer, V., Zängl, G., Zhang, D., and Quaas, J.: Large-eddy simulations over Germany using ICON: A comprehensive evaluation, *Quart. J. Roy. Meteor. Soc.*, 143, 69–100, 2017.
- Heus, T., van Heerwaarden, C. C., Jonker, H. J. J., Pier Siebesma, A., Axelsen, S., van den Dries, K., Geoffroy, O., Moene, A. F., Pino, D., de Roode, S. R., and Vilà-Guerau de Arellano, J.: Formulation of the Dutch Atmospheric Large-Eddy Simulation (DALES) and overview of its applications, *Geosci. Model Dev.*, 3, 415–444, 2010.
- Hohenegger, C., Brockhaus, P., and Schär, C.: Towards climate simulations at cloud-resolving scales, *Meteorol. Z.*, 17, 383–394, 2008.
- Horváth, Á., Seethala, C., and Deneke, H.: View angle dependence of MODIS liquid water path retrievals in warm oceanic clouds, *J. Geophys. Res.*, 119, 8304–8328, 2014.
- Illingworth, A. J., Barker, H. W., Beljaars, A., Ceccaldi, M., Chepfer, H., Clerbaux, N., Cole, J., Delanoë, J., Domenech, C., Donovan, D. P., Fukuda, S., Hiraoka, M., Hogan, R. J., Hünerbein, A., Kollias, P., Kubota, T., Nakajima, T., Nakajima, T. Y., Nishizawa, T., Ohno, Y., Okamoto, H., Oki, R., Sato, K., Satoh, M., Shephard, M. W., Velázquez-Blázquez, A., Wandinger, U., Wehr, T., and van Zadelhoff, G.-J.: The EarthCARE satellite: The next step forward in global measurements of clouds, aerosols, precipitation, and radiation, *Bull. Amer. Meteor. Soc.*, 96, 1311–1332, 2015.
- Ipe, A., Clerbaux, N., Bertrand, C., Dewitte, S., and Gonzalez, L.: Pixel-scale composite top-of-the-atmosphere clear-sky reflectances for Meteosat-7 visible data, *J. Geophys. Res.*, 108 (D19), 4612, 2003.
- Jonkheid, B. J., Roebeling, R. A., and van Meijgaard, E.: A fast SEVIRI simulator for quantifying retrieval uncertainties in the CM SAF cloud physical property algorithm, *Atmos. Chem. Phys.*, 12, 10 957–10 969, 2012.

- Kapur, J. N., Sahoo, P. K., and Wong, A. K. C.: A new method for gray-level picture thresholding using the entropy of the histogram, *Comput. Graphics Image Process*, 29, 273–285, 1985.
- Khain, A., Ovtchinnikov, M., Pinsky, M., Pokrovsky, A., and Krugliak, H.: Notes on the state-of-the-art numerical modeling of cloud microphysics, *Atmos. Res.*, 55, 159 – 224, 2000.
- Kiehl, J. T. and Trenberth, K. E.: Earth’s annual global mean energy budget, *Bull. Amer. Meteor. Soc.*, 78, 197–208, 1997.
- Klein, S. A., Zhang, Y., Zelinka, M. D., Pincus, R., Boyle, J., and Gleckler, P. J.: Are climate model simulations of clouds improving? An evaluation using the ISCCP simulator, *J. Geophys. Res. Atmos.*, 118, 1329–1342, 2013.
- Klüser, L., Rosenfeld, D., Macke, A., and Holzer-Popp, T.: Observations of shallow convective clouds generated by solar heating of dark smoke plumes, *Atmos. Chem. Phys.*, 8, 2833–2840, 2008.
- Koren, I., Oreopoulos, L., Feingold, G., Remer, L. A., and Altaratz, O.: How small is a small cloud?, *Atmos. Chem. Phys.*, 8, 3855–3864, 2008.
- Lensky, I. M. and Rosenfeld, D.: Clouds-Aerosols-Precipitation Satellite Analysis Tool (CAPSAT), *Atmos. Chem. Phys.*, 8, 6739–6753, 2008.
- Lin, Y.-L., Farley, R. D., and Orville, H. D.: Bulk parameterization of the snow field in a cloud model, *J. Climate Appl. Meteor.*, 22, 1065–1092, 1983.
- Loeb, N. G., Lyman, J. M., Johnson, G. C., Allan, R. P., Doelling, D. R., Wong, T., Soden, B. J., and Stephens, G. L.: Observed changes in top-of-the-atmosphere radiation and upper-ocean heating consistent within uncertainty, *Nat. Geosci.*, 5, 110–113, 2012.
- Madhavan, B. L., Deneke, H., Witthuhn, J., and Macke, A.: Multiresolution analysis of the spatiotemporal variability in global radiation observed by a dense network of 99 pyranometers, *Atmos. Chem. Phys.*, 17, 3317–3338, 2017.
- Marshak, A., Platnick, S., Várnai, T., Wen, G., and Cahalan, R. F.: Impact of three-dimensional radiative effects on satellite retrievals of cloud droplet sizes, *J. Geophys. Res.*, 111, D09 207, 2006.
- McComiskey, A. and Feingold, G.: The scale problem in quantifying aerosol indirect effects, *Atmos. Chem. Phys.*, 12, 1031–1049, 2012.

- Mechem, D. B., Yuter, S. E., and deSzoeko, S. P.: Thermodynamic and aerosol controls in Southeast Pacific stratocumulus, *J. Atmos. Sci.*, 69, 1250–1266, 2012.
- Mecikalski, J. R. and Bedka, K. M.: Forecasting convective initiation by monitoring the evolution of moving cumulus in daytime GOES imagery, *Mon. Wea. Rev.*, 134, 49–78, 2006.
- Mecikalski, J. R., Koenig, M., and Jewett, C. P.: Application of high-resolution visible sharpening of partly cloudy pixels in Meteosat Second Generation infrared imagery, *Atmos. Res.*, 134, 1–11, 2013.
- Merk, D., Deneke, H., Pospichal, B., and Seifert, P.: Investigation of the adiabatic assumption for estimating cloud micro- and macrophysical properties from satellite and ground observations, *Atmos. Chem. Phys.*, 16, 933–952, 2016.
- Minnis, P. and Harrison, E. F.: Diurnal variability of regional cloud and clear-sky radiative parameters derived from goes data. Part iii: November 1978 radiative parameters, *J. Clim. Appl. Meteorol.*, 23, 993–1011, 1984.
- Minnis, P., Garber, D. P., Young, D. F., Arduini, R. F., and Takano, Y.: Parameterizations of reflectance and effective emittance for satellite remote sensing of cloud properties, *J. Atmos. Sci.*, 55, 3313–3339, 1998.
- Nakajima, T. and King, M. D.: Determination of the optical thickness and effective particle radius of clouds from reflected solar radiation measurements. Part I: Theory, *J. Atmos. Sci.*, 47, 1878–1893, 1990.
- Otto, A., Otto, F. E. L., Boucher, O., Church, J., Hegerl, G., Forster, P. M., Gillett, N. P., Gregory, J., Johnson, G. C., Knutti, R., Lewis, N., Lohmann, U., Marotzke, J., Myhre, G., Shindell, D., Stevens, B., and Allen, M. R.: Energy budget constraints on climate response, *Nat. Geosci.*, 6, 415–416, 2013.
- Platnick, S.: A superposition technique for deriving mean photon scattering statistics in plane-parallel cloudy atmospheres, *J. Quant. Spectrosc. Radiat. Transfer*, 68, 57–73, 2001.
- Quaas, J., Boucher, O., and Bréon, F.-M.: Aerosol indirect effects in POLDER satellite data and the Laboratoire de Mtorologie Dynamique-Zoom (LMDZ) general circulation model, *J. Geophys. Res.*, 109, 2156–2202, 2004.
- Quaas, J., Boucher, O., Bellouin, N., and Kinne, S.: Satellite-based estimate of the direct and indirect aerosol climate forcing, *J. Geophys. Res. Atmos.*, 113, D05 204, 2008.



- Reverdy, M., Chepfer, H., Donovan, D., Noel, V., Cesana, G., Hoareau, C., Chiriaco, M., and Bastin, S.: An EarthCARE/ATLID simulator to evaluate cloud description in climate models, *J. Geophys. Res. Atmos.*, 120, 11,090–11,113, 2015.
- Roebeling, R. A., Feijt, A. J., and Stammes, P.: Cloud property retrievals for climate monitoring: Implications of differences between Spinning Enhanced Visible and Infrared Imager (SEVIRI) on METEOSAT-8 and Advanced Very High Resolution Radiometer (AVHRR) on NOAA-17, *J. Geophys. Res.*, 111, D20 210, 2006.
- Roebeling, R. A., Deneke, H. M., and Feijt, A. J.: Validation of cloud liquid water path retrievals from SEVIRI using one year of CloudNET observations, *J. Appl. Meteor. Climatol.*, 47, 206–222, 2008.
- Rosenfeld, D., Andreae, M. O., Asmi, A., Chin, M., de Leeuw, G., Donovan, D. P., Kahn, R., Kinne, S., Kivekäs, N., Kulmala, M., Lau, W., Schmidt, K. S., Suni, T., Wagner, T., Wild, M., and Quaas, J.: Global observations of aerosol-cloud-precipitation-climate interactions, *Rev. Geophys.*, 52, 750–808, 2014.
- Rossow, W. B. and Garder, L. C.: Cloud detection using satellite measurements of infrared and visible radiances for ISCCP, *J. Climate*, 6, 2341–2369, 1993.
- Schiffer, R. and Rossow, W. B.: The International Satellite Cloud Climatology Project (ISCCP) – The first project of the world climate research programme, *Bull. Amer. Meteor. Soc.*, 64, 779–784, 1983.
- Schlemmer, L. and Hohenegger, C.: The formation of wider and deeper clouds as a result of cold-pool dynamics, *J. Atmos. Sci.*, 71, 2842–2858, 2014.
- Schmetz, J., Pili, P., Tjemkes, S., Just, D., Kerkmann, J., Rota, S., and Ratier, A.: An introduction to Meteosat Second Generation (MSG), *Bull. Amer. Meteor. Soc.*, 83, 977–992, 2002.
- Schmit, T. J., Gunshor, M. M., Menzel, W. P., Gurka, J. J., Li, J., and Bachmeier, A. S.: Introducing the next-generation advanced baseline imager on Goes-R, *Bull. Amer. Meteor. Soc.*, 86, 1079–1096, 2005.
- Schulz, J., Albert, P., Behr, H.-D., Caprion, D., Deneke, H., Dewitte, S., Drr, B., Fuchs, P., Gratzki, A., Hechler, P., Hollmann, R., Johnston, S., Karlsson, K.-G., Manninen, T., Müller, R., Reuter, M., Riihelä, A., Roebeling, R., Selbach, N., Tetzlaff, A., Thomas, W., Werscheck, M., Wolters, E., and Zelenka, A.: Operational climate monitoring from space: the EUMETSAT satellite application facility on climate monitoring (CM-SAF), *Atmos. Chem. Phys.*, 9, 1687–1709, 2009.

- Seifert, A. and Beheng, D. K.: A two-moment cloud microphysics parameterization for mixed-phase clouds. Part 1: Model description, *Meteor. Atmos. Phys.*, 92, 45–66, 2005.
- Senf, F., Dietzsch, F., Hünnerbein, A., and Deneke, H.: Characterization of initiation and growth of selected severe convective storms over Central Europe with MSG-SEVIRI, *J. Appl. Meteor. Climatol.*, 54, 207–224, 2015.
- Slobodda, J., Hünnerbein, A., Lindstrot, R., Preusker, R., Ebell, K., and Fischer, J.: Multichannel analysis of correlation length of SEVIRI images around ground-based cloud observatories to determine their representativeness, *Atmos. Meas. Tech.*, 8, 567–578, 2015.
- Song, S., Schmidt, K. S., Pilewskie, P., King, M. D., Heidinger, A. K., Walther, A., Iwabuchi, H., Wind, G., and Coddington, O. M.: The spectral signature of cloud spatial structure in shortwave irradiance, *Atmos. Chem. Phys.*, 16, 13 791–13 806, 2016.
- Sourdeval, O., C-Labonnote, L., Baran, A. J., Mülmenstädt, J., and Brogniez, G.: A methodology for simultaneous retrieval of ice and liquid water cloud properties. Part 2: Near-global retrievals and evaluation against A-Train products, *Quart. J. Roy. Meteor. Soc.*, 142, 3063–3081, 2016.
- Stephens, G. L.: Radiation profiles in extended water clouds. II: Parameterization schemes, *J. Atmos. Sci.*, 35, 2123–2132, 1978.
- Stephens, G. L., Li, J., Wild, M., Clayson, C. A., Loeb, N., Kato, S., L’Ecuyer, T., Stackhouse, P. W., Lebsock, M., and Andrews, T.: An update on Earth’s energy balance in light of the latest global observations, *Nat. Geosci.*, 5, 691–696, 2012.
- Stubenrauch, C. J., Rossow, W. B., Kinne, S., Ackerman, S., Cesana, G., Chepfer, H., Girolamo, L. D., Getzewich, B., Guignard, A., Heidinger, A., Maddux, B. C., Menzel, W. P., Minnis, P., Pearl, C., Platnick, S., Poulsen, C., Riedi, J., Sun-Mack, S., Walther, A., Winker, D., Zeng, S., and Zhao, G.: Assessment of global cloud datasets from satellites: Project and database initiated by the GEWEX radiation panel, *Bull. Amer. Meteor. Soc.*, 94, 1031–1049, 2013.
- Stuhlmann, R., Rodriguez, A., Tjemkes, S., Grandell, J., Arriaga, A., Bézy, J.-L., Aminou, D., and Bensi, P.: Plans for EUMETSATs Third Generation Meteosat geostationary satellite programme, *Adv. Space Res.*, 36, 975 – 981, 2005.

- Tiedtke, M.: A comprehensive mass flux scheme for cumulus parameterization in large-scale models, *Mon. Weather Rev.*, 117, 1779–1800, 1989.
- Trenberth, K. E., Fasullo, J. T., and Kiehl, J.: Earth’s global energy budget, *Bull. Amer. Meteor. Soc.*, 90, 311–323, 2009.
- Várnai, T. and Marshak, A.: View angle dependence of cloud optical thicknesses retrieved by Moderate Resolution Imaging Spectroradiometer (MODIS), *J. Geophys. Res. Atmos.*, 112, D06 203, 2007.
- Watts, P. D., Bennartz, R., and Fell, F.: Retrieval of two-layer cloud properties from multispectral observations using optimal estimation, *J. Geophys. Res. Atmos.*, 116, D16 203, 2011.
- Weisman, M. L., Skamarock, W. C., and Klemp, J. B.: The resolution dependence of explicitly modeled convective systems, *Mon. Weather Rev.*, 125, 527–548, 1997.
- Wielicki, B. A., Barkstrom, B. R., Harrison, E. F., III, R. B. L., Smith, G. L., and Cooper, J. E.: Clouds and the Earth’s Radiant Energy System (CERES): An Earth observing system experiment, *Bull. Amer. Meteor. Soc.*, 77, 853–868, 1996.
- Wild, M., Folini, D., Schär, C., Loeb, N., Dutton, E. G., and König-Langlo, G.: The global energy balance from a surface perspective, *Climate Dyn.*, 40, 3107–3134, 2012.
- Wolters, E. L. A., Deneke, H. M., van den Hurk, B. J. J. M., Meirink, J. F., and Roebeling, R. A.: Broken and inhomogeneous cloud impact on satellite cloud particle effective radius and cloud-phase retrievals, *J. Geophys. Res.*, 115, D10 214, 2010.
- Wood, R. and Hartmann, D. L.: Spatial variability of liquid water path in marine low cloud: The importance of mesoscale cellular convection, *J. Climate*, 19, 1748–1764, 2006.
- Zelinka, M. D., Klein, S. A., and Hartmann, D. L.: Computing and partitioning cloud feedbacks using cloud property histograms. Part I: Cloud radiative kernels, *J. Climate*, 25, 3715–3735, 2012.
- Zelinka, M. D., Klein, S. A., Taylor, K. E., Andrews, T., Webb, M. J., Gregory, J. M., and Forster, P. M.: Contributions of different cloud types to feedbacks and rapid adjustments in CMIP5, *J. Climate*, 26, 5007–5027, 2013.
- Zhang, Z. and Platnick, S.: An assessment of differences between cloud effective particle radius retrievals for marine water clouds from three MODIS spectral bands, *J. Geophys. Res. Atmos.*, 116, D20 215, 2011.

- Zhang, Z., Ackerman, A. S., Feingold, G., Platnick, S., Pincus, R., and Xue, H.: Effects of cloud horizontal inhomogeneity and drizzle on remote sensing of cloud droplet effective radius: Case studies based on large-eddy simulations, *J. Geophys. Res.*, 117, 2156–2202, 2012.
- Zhang, Z., Werner, F., Cho, H.-M., Wind, G., Platnick, S., Ackerman, A. S., Di Girolamo, L., Marshak, A., and Meyer, K.: A framework based on 2-D Taylor expansion for quantifying the impacts of subpixel reflectance variance and covariance on cloud optical thickness and effective radius retrievals based on the bispectral method, *J. Geophys. Res. Atmos.*, 121, 7007–7025, 2016.
- Zinner, T. and Mayer, B.: Remote sensing of stratocumulus clouds: Uncertainties and biases due to inhomogeneity, *J. Geophys. Res.*, 111, D14 209, 2006.
- Zinner, T., Mannstein, H., and Tafferner, A.: Cb-TRAM: Tracking and monitoring severe convection from onset over rapid development to mature phase using multi-channel Meteosat-8 SEVIRI data, *Meteorol. Atmos. Phys.*, 101, 191–210, 2008.

# List of Abbreviations

AMV	Atmospheric Motion Vector
ASTER	Advanced Spaceborne Thermal Emission and Reflection Radiometer
ATLID	ATmospheric LIDar
AVHRR	Advanced Very High Resolution Radiometer
CF	Cloud Fraction
CM	Cloud Mask
CM SAF	Satellite Application Facility on Climate Monitoring
COSP	Cloud Feedback Model Intercomparison Project Observation Simulator Package
COSMO	Consortium for Small-scale Modeling
COT	Cloud Optical Thickness
CPP	Cloud Physical Properties
CT	Cloud Type
CTH	Cloud Top Height
CWP	Cloud Water Path
DAK	Doubling Adding KNMI
DWD	Deutscher Wetterdienst
EarthCARE	Earth Clouds, Aerosols and Radiation Explorer
ECMWF	European Center for Medium range Weather Forecasting
ECS	Equilibrium Climate Sensitivity
GCM	General Circulation Model
GOES-R	Geostationary Operational Environmental Satellite-R series
HD(CP) <sup>2</sup>	High Definition Clouds and Precipitation for Advanced Climate Prediction
HRW	High Resolution Wind
HRV	High Resolution Visible
ICON	ICOsahedral Nonhydrostatic
ISCCP	International Satellite Cloud Climatology Project
LES	Large Eddy Simulation

LW	LongWave
LWC	Liquid Water Content
LWP	Liquid Water Path
MSG	Meteosat Second Generation
MTG	Meteosat Third Generation
NWC SAF	Satellite Application Facility on Support to Nowcasting and Very Short Range Forecasting
NWP	Numerical Weather Prediction
PBL	Planetary Boundary Layer
RGB	Red-Green-Blue
RSS	Rapid Scan Service
RTTOV	Radiative Transfer models for calculations of radiances for satellite infrared or microwave nadir scanning radiometers
SEVIRI	Spinning Enhanced Visible and InfraRed Imager
SW	ShortWave
TCR	Transient Climate Response
TOA	Top Of Atmosphere
TROPOS	Leibniz Institute for Tropospheric Research
WCRP	World Climate Research Programme
WV	Water Vapor



## List of Symbols

$\rho_w$	Density of water
$\tau$	Cloud optical thickness
$r_e$	Cloud droplet effective radius
$\text{CO}_2$	Carbon dioxide
$\text{N}_2\text{O}$	Nitrous oxide
$\text{CH}_4$	Methane
$\text{O}_3$	Tropospheric ozone

## List of Figures

- 1.1 Annual global mean energy balance of the Earth, representing present day climate conditions at the the beginning on the twenty-first century (Wild et al., 2012). . . . . 2
- 1.2 Equilibrium temperature change associated with the Planck response, water vapor, surface albedo and cloud feedback, computed for 12 CMIP3/AR4 calculations for a  $2\times\text{CO}_2$  forcing (Dufresne and Bony, 2008). 3
- 1.3 (a) Three length scales of an atmosperic model with different grid resolutions of  $L=25.6$  km (length scale of deterministic parameterizations in NWP models),  $l=1.6$  km (length scale where stochastic parameterizations are required) and  $\Delta x=50$  m (length scale of LES simulations) (Dorrestijn et al., 2012). (b) Decomposition of the resolved and unresolved turbulent fluxes in relation to the grid resolution  $l$  for the full  $25.6\times 25.6$  km<sup>2</sup> domain shown in (a). The solid dotted line represents the standard deviation of the unresolved fluxes. . 5

2.1	SEVIRI Full disk red-green-blue (RGB) natural color image following the Lensky and Rosenfeld (2008) method. Data for this thesis is taken from the rapid scan service (RSS), which covers a sub region of the full disk from approximately 15° to 70° N. This smaller area leads to a higher repeat cycle of 5 min instead of 15 min. The white rectangle marks a region over Central Europe, which is chosen for this thesis. . . . .	11
2.2	Look-up table for calculation of $\tau$ and $r_e$ from the KNMI DAK radiative transfer simulations. Solid lines are related to $r_e$ , vertical dashed lines correspond to $\tau$ . The red cross demonstrates an example cloudy pixel with $r_e=12 \mu\text{m}$ and $\tau=16$ . . . . .	13
2.3	Theoretical case to illustrate the nonlinearity effect in $r_e$ retrievals resulting from sub-pixel cloud inhomogeneity (Zhang et al., 2012). Numbers on top of the Nakajima King look-up table correspond to $\tau$ , numbers on the right represent $r_e$ . . . . .	17
3.1	ICON-LEM domain and its two nests with grid refinement. The open lateral boundaries are relaxed towards COMSO-DE analysis (Heinze et al., 2017). . . . .	20
3.2	Domain covered by the COSMO-DE model with 421×461 grid points (Baldauf et al., 2011). . . . .	21

## List of Tables

2.1	SEVIRI channels . . . . .	12
-----	---------------------------	----

# Acknowledgements

I would like to take the opportunity to thank a number of people that supported me over the last years having a great time as a PhD student in the satellite working group at TROPOS.

Most of all, I am grateful to my supervisors, Hartwig Deneke, Andreas Macke and Johannes Quaas, for the opportunity to work in this exciting field and for their extraordinary support and for many expert suggestions and fruitful discussions.

I would especially like to thank all colleagues from the satellite working group. I greatly enjoyed the pleasant and familiar atmosphere in our group. Beyond refreshing discussions during group meetings or coffee breaks, also our Christmas and summer parties, group retreats in the Saxon Switzerland as well as joint conference trips to Gdansk, Vienna and Toulouse, will leave pleasant and lasting memories.

Dear Hartwig, thank you for supporting me in difficult questions and problems. You helped me to keep my long-term research objectives in mind, while giving me also a lot of open space for my own ideas and how to reach my goals. Your thoughtful reviews and suggestions on all my manuscripts considerably helped me to improve this thesis. Thank you also for the opportunity to participate in the Polarstern expedition PS 83.

Dear Fabian and Anja, I would like to thank you for your very energetic support and the time that you always spend to help me to solve complex mathematical problems and programming challenges. Fabian, your keen eye for detail is invaluable.

Dear Daniel, you have become a very good friend. I am glad that we are sharing so many great experiences and still stay in contact after you have left our group. Thank you for your competent reviews and comments on my publications and this thesis.

Dear Skat group, it was a joy to be part of our group playing cards on Wednesdays and having a lot of fun, especially when we had crazy Ramsch rounds.

Furthermore, I would like to thank all PhD students for exciting events like trips to the Saxon Switzerland, the outstanding team spirit and warm atmosphere.

Dear Family, I would like to thank you that you always supported and encouraged me in my decisions with a lot of patience.

Dear Ulrike, thank you for your encouragement and for making my life much happier. It was a great luck that we met right in the perfect time.



# Curriculum Vitae

## Sebastian Bley

Date of birth            25th June 1986  
Address                 Rudolph-Herrmann-Str. 22  
                               D-04299 Leipzig  
                               Germany  
                               +4917663049558  
                               sebastian.bley@tropos.de

## Academic Education

Since 12/2012	<b>PhD candidate</b> Leibniz Institute for Tropospheric Research (TROPOS), Leipzig, Germany HD(CP) <sup>2</sup> (High definition clouds and precipitation for advancing climate prediction)
10/2009 – 03/2012	<b>Master of Science in Meteorology (grade: 1.3)</b> University of Leipzig, Germany Master thesis (in German): Comparison of two threshold algorithms for cloud detection in solar Meteosat SEVIRI images and application on the HRV channel
10/2006 – 09/2009	<b>Bachelor of Science in Meteorology (grade: 1.9)</b> University of Leipzig, Germany
09/1997 – 06/2005	Secondary school Evangelisches Kreuzgymnasium Dresden (Abitur)





## Declaration of Independence

Hereby I, Sebastian Bley, declare that I prepared this PhD Thesis without inadmissible aid and only by the usage of the specified resources. I also declare, that I marked the directly or indirectly adopted ideas from external references.

I insure that I do not get any assistance benefits from other persons in selection and evaluation of the material as well as in the preparation of the manuscript.

Furthermore, I hereby declare and confirm that this PhD dissertation is entirely the result of my own investigations except where otherwise indicated. In particular, I insure that I did not make a claim on the aid of a doctoral consultant. Also I insure that no one has gained, from me or from other persons on behalf on me, immediately or indirectly pecuniary advantages, which are related to the content of this PhD dissertation.

Hereby I insure that this PhD Thesis was not submitted, neither in Germany nor in other countries, in an identical or similar design to another examination office for the purpose of a graduation or another examination procedure.

Hereby I state that I have not been involved in another PhD procedure.

Leipzig, 11.04.2017

Leipzig, 11.04.2017

S. Bley

Sebastian Bley



Zusammenfassung der wissenschaftlichen Ergebnisse zur Dissertation

# Investigation of Warm Convective Cloud Fields with Meteosat Observations and High Resolution Models

Von der Fakultät für Physik und Geowissenschaften der Universität Leipzig

genehmigte

## Dissertation

M. Sc. Sebastian Bley

angefertigt am

Leibniz-Institut für Troposphärenforschung (TROPOS)

Tag der Verleihung: 23.10.2017

---

Warm convective clouds are highly variable in space and time and cover large areas of the earth (Turner et al., 2007). Through the transport of energy and moisture, they couple the boundary layer and the free troposphere. Their bright cloud tops reflect the incoming sunlight which strongly modulates the atmospheric radiation budget (Trenberth et al., 2009). There is a clear evidence that the Earth's climate is changing and that greenhouse gases emitted by human activity are drastically increasing (Hartmann et al., 2013). It is still not fully understood, how much the globe will warm exactly and how the climate system will respond to rising greenhouse gases, particularly the carbon dioxide ( $\text{CO}_2$ ) concentration. Because of our lack of understanding of relevant processes and feedbacks, low-level clouds remain a dominant source of uncertainty in climate projections (Clement et al., 2009). The realistic representation of clouds in general circulation models (GCMs) in general, and low-level convective clouds in particular, remains a fundamental challenge of climate research (Bony et al., 2015). This difficulty arises in part from the coarse horizontal resolution ( $\sim 100$  km) of GCMs, which does not allow to resolve individual clouds nor the underlying turbulent, microphysical and convective processes. Instead, sub-grid scale processes below the model resolution have to be parameterized. Thus, there is a great need to further investigate the physical processes of convective clouds to better quantify the uncertainties in satellite observations as well as atmospheric and climate models.

The overall aim of the present thesis is an in-depth characterization of the spatiotemporal evolution of convective cloud fields with the Spinning Enhanced Visible and Infrared Imager (SEVIRI) on-board the geostationary Meteosat Second Generation (MSG) satellite and its applicability towards model evaluation. While polar-orbiting satellites like MODIS can resolve finer spatial cloud structures due to their higher spatial resolution, only geostationary satellites

like Meteosat have the capability to observe and track clouds from their early developing stage onwards. A further goal is to establish appropriate metrics to evaluate the representation of convective cloud fields in the high resolution model ICON-LEM and to characterize convective cloud fields across different spatial scales. This characterization provides complementary information about the spatial structure and temporal changes of cloud properties, to serve as finger-print of underlying dynamical and microphysical processes. In addition, information on the spatial structure of cloud fields as given by the power spectrum are essential to realistically represent cloud radiative effects in models and observations (Davis et al., 1996).

The main scientific questions for this thesis are formulated as follows:

1. How can we improve the representation of small-scale convective clouds using Meteosat observations?
2. What are suitable metrics for evaluating high resolution model simulations with relatively coarsely resolved satellite observations?
3. How sensitive are the spatiotemporal characteristics of convective cloud fields to the spatial resolution of a sensor or a model?
4. How can uncertainties of retrieved cloud properties and the instrumental limitations of MSG SEVIRI be quantified and which improvements are expected with respect to upcoming satellite missions?

Summarizing the results of this thesis, the answers to these questions are formulated as follows:

1. The high resolution visible channel was used to develop a cloud mask with an enhanced spatial resolution from  $3 \times 6 \text{ km}^2$  to  $1 \times 2 \text{ km}^2$  compared to the operational cloud mask. Suitable techniques were investigated to improve the representation of small-scale convective clouds and to further increase the resolution of retrieved convective cloud properties. The HRV mask identifies a ratio of 16 % of the operational cloudy pixel as fractional clouds on average.
2. The frequency distribution of the LWP, cloud size distribution and spatiotemporal scales were characterized across different spatial scales, ranging from the comparatively coarse satellite resolution to high model resolution. A sophisticated tracking algorithm was developed to quantify the convective and advective changes, which influence the evolution of warm convective cloud fields. The simulated spatiotemporal scales, however, had to be coarse-grained to the optical resolution of Meteosat to enable an appropriate evaluation and ensure comparability.
3. The investigated metrics reveal a pronounced sensitivity to the spatial model and satellite sensor resolution. The scaling behavior of the spatiotemporal characteristics and the cloud size distribution of the simulations indicates the effective resolution of the ICON-LEM model, which is 8–10 times the native model grid resolution.
4. The gained insights into the sensitivity of the spatiotemporal characteristics on the spatial resolution indicate that an increase of the spatial resolution to 1 km or even 500 m would be desirable for the Meteosat cloud properties, to better quantify the small-scale variability of convective clouds. This range will be covered by Meteosat Third Generation (MTG) and highlights the great opportunity to improve the observations of convective clouds once the

new series of satellites is launched in 2021 (Stuhlmann et al., 2005).

In conclusion, this study emphasizes that a geostationary satellite instrument with a repeat cycle of at least 1 min and a horizontal resolution of 100 m would be desirable to substantially improve the characterization of convective clouds and the development of sophisticated parameterizations for numerical weather prediction and climate models. Such an observational capacity could contribute towards answering the question: “What role does convection play in cloud feedbacks?” which is one of the big challenges of climate science as formulated by Bony et al. (2015).

## Bibliography

- Bony, S., Stevens, B., Frierson, D. M. W., Jakob, C., Kageyama, M., Pincus, R., Shepherd, T. G., Sherwood, S. C., Siebesma, A. P., Sobel, A. H., Watanabe, M., and Webb, M. J.: Clouds, circulation and climate sensitivity, *Nat. Geosci.*, 8, 261–268, 2015.
- Clement, A. C., Burgman, R., and Norris, J. R.: Observational and model evidence for positive low-level cloud feedback, *Science*, 325, 460–464, 2009.
- Davis, A., Marshak, A., Wiscombe, W., and Cahalan, R.: Scale invariance of liquid water distributions in marine stratocumulus. Part I: Spectral properties and stationarity issues, *J. Atmos. Sci.*, 53, 1538–1558, 1996.
- Hartmann, D., Klein Tank, A., Rusticucci, M., Alexander, L., Brönnimann, S., Charabi, Y., Dentener, F., Dlugokencky, E., Easterling, D., Kaplan, A., Soden, B., Thorne, P., Wild, M., and Zhai, P.: Observations: Atmosphere and surface, pp. 159–254, *Climate change 2013: The physical science basis. Contribution of working group I to the fifth assessment report of the intergovernmental panel on climate change*, Cambridge University Press, 2013.
- Stuhlmann, R., Rodriguez, A., Tjemkes, S., Grandell, J., Arriaga, A., Bézy, J.-L., Aminou, D., and Bensi, P.: Plans for EUMETSATs Third Generation Meteosat geostationary satellite programme, *Adv. Space Res.*, 36, 975 – 981, 2005.
- Trenberth, K. E., Fasullo, J. T., and Kiehl, J.: Earth’s global energy budget, *Bull. Amer. Meteor. Soc.*, 90, 311–323, 2009.
- Turner, D., Vogelmann, A., Austin, R., Barnard, J., Cady-Pereira, K., Chiu, J. C., Clough, S., Flynn, C., Khaiyer, M., Liljegren, J., Johnson, K., Lin, B., Long, C., Marshak, A., Matrosov, S., McFarlane, S., Miller, M., Min, Q., Minnis, P., O’Hirok, W., Wang, Z., and Wiscombe, W.: Thin liquid water clouds: Their importance and our challenge, *Bulletin of the American Meteorological Society*, 88, 177–190, 2007.

## Publications List

### First publication:

”Bley, S. and Deneke, H.: A threshold-based cloud mask for the high-resolution visible channel of Meteosat Second Generation SEVIRI, *Atmos. Meas. Tech.*, **6**, 27132723, 2013.”

In this publication, I developed the threshold-based HRV cloud mask algorithm, evaluated the data with the EUMETSAT cloud mask and wrote the manuscript draft. Moreover, I processed the HRV cloud mask for three years from 2012-2014 using the newly developed algorithm. Dr. Hartwig Deneke gave the full support, proposed many valuable suggestions for this study and carried out corrections for this publication.

### Second publication:

”Bley, S., Deneke, H., and Senf, F.: Meteosat-based characterization of the spatiotemporal evolution of warm convective cloud fields over Central Europe, *J. Appl. Meteorol. Climat.*, **55**, 21812195, 2016.”

In this paper, I performed the tracking of the warm convective cloud fields and did the statistical analysis with the auto-correlation function. For the tracking, I adjusted the configuration of the high resolution wind product in the NWC SAF software package. I calculated the wind vectors and collected a case database with warm convective cloud fields over Central Europe. After a comprehensive analysis I wrote the manuscript draft with full support and many corrections carried out by Hartwig Deneke and Fabian Senf.

### Third publication:

”Bley, S., Deneke, H., Senf, F., and Scheck, L.: Metrics for the evaluation of warm convective cloud fields in a large eddy simulation with Meteosat images, *Quart. J. Roy. Meteor. Soc.*, **143**, 2050–2060, 2017.”

In this study, I accessed and prepared the data output from the ICON-LEM and COSMO-DE simulations, which were both conducted in the HD(CP)<sup>2</sup> project. Due to the large model output of several TB per simulation day, it took me quite some time to cut out the relevant cloud microphysical data and to interpolate it to an equidistant two-dimensional grid to enable comparability with the satellite observations. In the next step, I developed a coarse-graining algorithm to average the high resolution model data to the satellite data and implemented the different metrics in the analysis in collaboration with Hartwig Deneke and Fabian Senf. Leonhard Scheck supported the distribution of the simulated cloud sizes and gave many valuable comments. I finally wrote the manuscript draft, that was also supported and corrected by Hartwig Deneke and Fabian Senf.

### Fourth publication (not a part of this thesis):

Baars, H., Kanitz, T., Engelmann, R., Althausen, D., Heese, B., Komppula, M., Preiler, J., Tesche, M., Ansmann, A., Wandinger, U., Lim, J.-H., Ahn, J. Y., Stachlewska, I. S., Amiridis, V., Marinou, E., Seifert, P., Hofer, J., Skupin, A., Schneider, F., Bohlmann, S., Foth, A., Bley, S., Pfüller, A., Giannakaki, E., Lihavainen, H., Viisanen, Y., Hooda, R. K., Pereira, S. N., Bortoli, D., Wagner, F., Mattis, I., Janicka, L., Markowicz, K. M., Achtert, P., Artaxo, P., Pauliquevis, T., Souza, R. A. F., Sharma, V. P., van Zyl, P. G., Beukes, J. P., Sun, J., Rohwer, E. G., Deng, R., Mamouri, R.-E., and Zamorano, F.: An overview of the first decade of PollyNET: An emerging network of automated Raman-polarization lidars for continuous aerosol profiling, *Atmos. Chem. Phys.*, **16**, 5111–5137, doi:10.5194/acp-16-5111-2016, 2016.



In this publication, I contributed to the long-term dataset of aerosol measurements with the multiwavelength-polarization-Raman lidars (Polly) aboard the research vessel Polarstern during the expedition PS 83 (ANT-XXIX/10). I calculated together with Andreas Foth backscatter and extinction profiles over the Atlantic Ocean and did some corrections on the manuscript.

### Fifth publication (not a part of this thesis):

Heinze, R., Dipankar, A., Henken, C. C., Moseley, C., Sourdeval, O., Trömel, S., Xie, X., Adamidis, P., Ament, F., Baars, H., Barthlott, C., Behrendt, A., Blahak, U., **Bley, S.**, Brdar, S., Brueck, M., Crewell, S., Deneke, H., Di Girolamo, P., Evaristo, R., Fischer, J., Frank, C., Friederichs, P., Göcke, T., Gorges, K., Hande, L., Hanke, M., Hansen, A., Hege, H.-C., Hoose, C., Jahns, T., Kalthoff, N., Klocke, D., Kneifel, S., Knippertz, P., Kuhn, A., van Laar, T., Macke, A., Maurer, V., Mayer, B., Meyer, C. I., Muppa, S. K., Neggers, R. A. J., Orlandi, E., Pantillon, F., Pospichal, B., Röber, N., Scheck, L., Seifert, A., Seifert, P., Senf, F., Siligam, P., Simmer, C., Steinke, S., Stevens, B., Wapler, K., Weniger, M., Wulfmeyer, V., Zängl, G., Zhang, D. and Quaas, J.: Large-eddy simulations over Germany using ICON: A comprehensive evaluation. *Quart. J. Roy. Meteor. Soc.*, **143**: 69–100. doi:10.1002/qj.2947.

In this publication, I wrote the section "Horizontal distribution of cloud parameters" as part of the "Clouds" chapter in collaboration with Odran Sourdeval and Cintia Carbajal Henken. I did the evaluation of the horizontal distribution of simulated cloud properties from the ICON-LEM model using observations from Meteosat and MODIS and simulations from the operational COSMO-DE model. I finally did some corrections throughout the review process.

**PhD commission:****Prof. Dr. Johannes Quaas (Chairman)**

Institute for Meteorology, University of Leipzig, Leipzig, Germany  
johannes.quaas@uni-leipzig.de

**Prof. Dr. Andreas Macke (Supervisor)**

Leibniz Institute for Tropospheric Research, Leipzig, Germany  
andreas.macke@tropos.de

**Prof. Dr. Ina Tegen**

Leibniz Institute for Tropospheric Research, Leipzig, Germany  
ina.tegen@tropos.de

**Supervisor committee:****Prof. Dr. Andreas Macke (First supervisor)**

Leibniz Institute for Tropospheric Research, Leipzig, Germany  
andreas.macke@tropos.de

**Dr. Hartwig Deneke (co-supervisor)**

Leibniz Institute for Tropospheric Research, Leipzig, Germany  
hartwig.deneke@tropos.de

**Prof. Dr. Johannes Quaas (co-supervisor)**

Institute for Meteorology, University of Leipzig, Leipzig, Germany  
johannes.quaas@uni-leipzig.de